
Mass Determination of Elliptical Galaxies

Natalya Lyskova



München 2014

Mass Determination of Elliptical Galaxies

Natalya Lyskova

Dissertation
an der Fakultät für Physik
der Ludwig-Maximilians-Universität
München

vorgelegt von
Natalya Lyskova
aus Perm, Russland

München, den 10 Januar 2014

Erstgutachter: Prof. Dr. Rashid Sunyaev

Zweitgutachter: Prof. Dr. Ortwin Gerhard

Tag der mündlichen Prüfung: 21 February 2014

Contents

Zusammenfassung	xi
Summary	xiii
1 Introduction	1
1.1 Mass determination techniques	2
1.1.1 X-ray analysis	2
1.1.2 Gravitational lensing	3
1.1.3 Dynamical modeling	4
1.2 The simple(st) mass estimators	5
1.2.1 The virial theorem and virial-like estimators	5
1.2.2 Estimators based on the spherical Jeans equation	8
1.3 Structure of the thesis	13
2 Simple recipe for estimating galaxy masses	17
2.1 Introduction	18
2.2 Description of the method	18
2.3 The sample of simulated galaxies	20
2.3.1 Description of the sample	20
2.3.2 Isothermality of potentials in massive galaxies	21
2.3.3 Analysis procedure	22
2.4 Analysis of the sample	26
2.4.1 At a sweet point	26
2.4.2 Simulated galaxies at high redshifts	31
2.4.3 Mass from integrated properties	31
2.4.4 Circular speed derived from the aperture velocity dispersion	33
2.4.5 Circular speed from X-ray data	35
2.5 Testing the method on simulated galaxy clusters	37
2.6 Discussion	41
2.7 Conclusions	44
2.8 Acknowledgments	45

3 X-ray bright elliptical galaxies	49
3.1 Introduction	50
3.2 Description and justification of the method	51
3.2.1 Rotation of galaxies.	53
3.2.2 An algorithm for estimating V_c	56
3.3 Analysis	56
3.3.1 M87, revisited. Illustration of the Method	56
3.3.2 Observations and data reduction	61
3.3.3 Circular speed from X-ray data.	62
3.3.4 Optical Rotation Curves	68
3.3.5 Comments on individual galaxies.	70
3.3.6 Stellar populations: properties, M/L , contributions to the total mass	73
3.4 Discussion	79
3.5 Conclusion	83
3.6 Acknowledgments	84
4 Performance of simple mass estimators for elliptical galaxies	89
4.1 Introduction	90
4.2 Mass approximation formulae.	91
4.2.1 Local estimator.	92
4.2.2 Global estimator.	93
4.3 Tests	94
4.3.1 Analytic models.	94
4.3.2 Tests on simulated galaxies.	101
4.4 Comparison of simple mass estimators with a state-of-the-art analysis.	107
4.5 Mass proxy.	113
4.6 Discussions and Conclusions.	114
4.7 Acknowledgments	115
5 Conclusions	119
Acknowledgements	123

List of Figures

1.1	X-ray and optical image of the Coma cluster	3
1.2	Example of a strong gravitational lensing.	4
1.3	Aperture velocity dispersion as a function of aperture radius.	7
1.4	Projection of a spherical system along the line of sight	9
1.5	$\sigma_p(R)$ for $I(R) \propto e^{-7.67(R/R_{1/2})^4}$ in $\Phi(r) = V_c^2 \ln r + const$	10
1.6	σ_p for $I(R) \propto R^{-\alpha}$ in $\Phi(r) = V_c^2 \ln r + const$ as a function of α	11
2.1	Circular velocity curves of massive simulated galaxies	21
2.2	Excluding the satellites from the galaxy image	22
2.3	Influence of satellites on $I(R)$, $\sigma_p(R)$ and recovered V_c^{iso}	23
2.4	$R_{\text{eff}} - M_*$ relation as found for simulated galaxies	25
2.5	Histograms of deviations $\Delta_{opt} = (V_c^{iso} - V_c^{\text{true}}) / V_c^{\text{true}}$ at different radii	26
2.6	Examples of a relaxed galaxy and a galaxy with merger activity	27
2.7	Histograms for the subsamples of simulated galaxies	28
2.8	Histograms of deviations calculated for the subsample ‘MG’ at different radii	30
2.9	Accuracy of the derived potential of massive simulated galaxies	32
2.10	$\sigma_{ap}(< R)$ within aperture of different radii as a V_c -estimate	34
2.11	Hot gas electron $n(r)$, $T(r)$, $P = nkT$ and $V_c(r)$ of a simulated galaxy	36
2.12	V_c -estimate from X-ray data for simulated galaxies	37
2.13	Excluding the clumps from a hot gas density map of a simulated galaxy	38
2.14	Simple circular speed estimation in the simulated galaxy cluster	39
2.15	The fraction of galaxy clusters as a function of the deviation	40
2.16	Distribution of high-redshift galaxies from the subsample ‘MG’	43
3.1	Histograms of orientation-averaged deviations Δ_{opt} for simulated galaxies .	54
3.2	Simple circular speed estimates of M87	58
3.3	Simple V_c -estimates for M87 Vs the state-of-the-art V_c -profiles	59
3.4	The results of the SAO RAS 6-m telescope observations	63
3.4	(continue)	64
3.4	(continue)	65
3.5	The effect of the abundance gradient on the X-ray derived $V_c(r)$	67
3.6	Simple V_c -estimates, X-ray based V_c and the stellar contribution to the V_c .	71
3.6	(continue)	72

3.7	The comparison of the Lick index profiles in NGC 4125	74
3.8	The comparison of the Lick index profiles in NGC 708	76
3.9	The radial variations of the stellar population metallicity	77
3.10	The variations of the stellar population M/L along the radius	78
3.11	The radial profiles of the surface mass density along the radius	80
4.1	Typical profiles considered for a sample of analytical models	96
4.2	Circular speed estimates for ‘ideal’ model galaxy	97
4.3	Deviations of simple V_c -estimates from V_c^{true} for model spherical galaxies .	99
4.4	Dependence of deviations on properties of the $V_c^{true}(r)$ and $\sigma_p(R)$	100
4.5	Deviations for the local V_c -estimator from the V_c^{true} for simulated galaxies .	102
4.6	Deviations for the global V_c -estimator from the V_c^{true} for simulated galaxies	103
4.7	Observed correlations for simulated galaxies	105
4.8	Deviation of the estimated V_c from the V_c^{true} as a function of M_{vir}	106
4.9	$\alpha(R)$, $\sigma_p(R)$ and V_c^{Schw} from the Schwarzschild modeling	108
4.10	Comparison of simple V_c -estimates with V_c^{Schw}	110
4.10	(continue)	111
4.11	M_{vir} of simulated galaxies as a function of $\sigma_p(R_2)$ and $\sqrt{\langle \sigma_p^2 \rangle}$	114

List of Tables

2.1	Summary of the methods discussed.	41
3.1	Sample of observed with the SAO RAS 6-m telescope elliptical galaxies	61
3.2	Log of the observations	61
3.3	V_c -estimates for our sample of elliptical galaxies	69
3.4	Metallicity gradient within and beyond the half effective radius.	75
3.5	Stellar masses and the fraction of dark matter (DM) within R_{sweet}	79
3.6	Ellipticity and effective radius for the sample galaxies	81
4.1	Main properties of Churazov et al. and Wolf et al. estimators.	95
4.2	Sample of real elliptical galaxies analyzed using the Schwarzschild modeling	107
4.3	Simple V_c -estimates and V_c from dynamical modeling	112
4.4	Summary table	113

Zusammenfassung

Die vorliegende Arbeit beschäftigt sich vorwiegend mit der Untersuchung und Weiterentwicklung einer einfachen Schätzfunktion für die Masse von frühen Galaxien, die sich für grobe optische Galaxiendurchmusterungen mit mangelhaften und/oder ungenauen Daten eignen. Wir ziehen einfache und stabile Methoden in Betracht, die eine anisotropieunabhängige Massenberechnung einer Galaxie aufgrund von Flächenhelligkeit und projizierten Geschwindigkeitsdispersionsdiagrammen ermöglichen. Es ist sinnvoll anzunehmen, dass eine grundlegende Degenaration der Anisotropie der Masse umgangen werden kann, ohne sich auf zusätzliche Beobachtungsdaten verlassen zu müssen, allerdings nur in einem speziellen (charakteristischen) Radius, z.B. behandeln die Ansätze nicht die kreisförmige Massendistribution. Zuverlässige Schätzwerte in einem einzigen Radius können wie folgt verwendet werden: (i) Kalibrierung anderer Methoden zur Massenberechnung; (ii) Schätzung einer non-thermalen Zufuhr zum Gesamtdruck im Vergleich zu einem Schätzwert der Masse einer Röntgengalaxie im gleichen Radius; (iii) Auswertung des Anteils der dunklen Materie im Vergleich zu der heller Materie; (iv) Ableitung der Steigung des Massenprofils, kombiniert mit dem Schätzwert der Masse eines starken Gravitationslinseneffekts; (v) Ersatz für die Virialmasse.

Vor kurzem wurden zwei einfache Methoden ausgearbeitet: die lokale (Churazov et al. 2010) und die globale Methode (Wolf et al. 2010). Diese berechnen die Masse in einem spezifischen Radius und sind kaum von der Anisotropie stellarer Umlaufbahnen abhängig. Einer der Ansätze (Wolf et. al. 2010) verwendet die gesamte, nach der Leuchtkraft gewichtete Geschwindigkeitsdispersion und wertet die Masse in einem deprojizierten Halblichtradius aus, d.h. sie verlässt sich auf die globalen Eigenschaften einer Galaxie. Im Gegensatz dazu verwendet die Churazov et. al.-Methode lokale Eigenschaften, also logarithmische Kurven der Flächenhelligkeit und der Geschwindigkeitsdispersionsdiagramme, und berechnet die Masse in einem Radius, in dem die Flächenhelligkeit mit R^{-2} abnimmt (siehe Richstone und Tremaine 1984, Gerhard 1993).

Um die Stabilität und Genauigkeit der Methoden zu überprüfen, habe ich diese auf analytische Modelle sowie simulierte Galaxien aus einer Stichprobe von kosmologischen Simulationen, die ähnliche Eigenschaften früher Galaxien aufweisen, angewendet. Die lokalen sowie globalen Schätzwerte scheinen mit der Masse in dem entsprechenden charakteristischen Radius übereinzustimmen. Insbesondere für massive langsam rotierende Galaxien ermöglicht die lokale Methode eine nahezu unverfälschte Schätzung der Masse (wenn man es mit der Stichprobe angleicht) mit einer leichten QMW-Abweichung von $\simeq 12\%$ (Kapitel

2). Wenn man die globale Methode auf massive simulierte Galaxien mit einem annähernd flachen Geschwindigkeitsdispersionsdiagramm anwendet, kann man ebenfalls eine nahezu unverfälschte Schätzung der Masse erzielen, obwohl die QMW-Abweichung geringfügig größer ausfällt ($\simeq 14 - 20\%$), als für die lokale Methode (Kapitel 4). Eine auffällige Abweichung wird in der Ermittlung des charakteristischen Radius erwartet, da der Halblichtradius von dem Radiusbereich für die Analyse und der angewandten Methode abhängt.

Als nächstes habe ich die Schätzfunktionen an einer Stichprobe einer echten frühen Galaxie, die schon eingehend mit dem neuesten dynamischen Modellverfahren analysiert wurde, analysiert. Für diese Gruppe von Galaxien liegen die Schätzwerte erstaunlich nah an den Ergebnissen der Schwarzschildmodelle, obwohl einige davon flach sind und langsam rotieren. Sobald die lokale Schätzfunktion an das Beispiel angeglichen worden ist, beträgt die Abweichung von der im dynamischen Modellverfahren errechneten Idealmasse $\approx 10\%$ und die QMW-Abweichung $\approx 13\%$ zwischen den verschiedenen Galaxien. Die Erwartungstreue kann mit Messunsicherheit verglichen werden. Des Weiteren wird die Abweichung größtenteils von einer einzigen Galaxie verursacht, die die höchste Dichte in der Stichprobe aufweist. Schließt man diese aus der Stichprobe aus, vermindert sich die Verzerrung auf $\approx 6\%$ und die QMW-Abweichung um $\approx 6\%$. Die globale Schätzfunktion für dieselbe Stichprobe zeigt eine mittlere Abweichung von $\approx 4\%$ mit einer geringfügig größeren QMW-Abweichung von $\approx 15\%$ (Kapitel 4).

Angesichts der positiven Ergebnisse wende ich die lokale Schätzmethode auf eine Stichprobe an, die fünf helle frühe Röntgengalaxien beinhaltet, die mit einem 6-m Teleskop in Russland beobachtet werden. Durch die Verwendung der öffentlich verfügbaren Chandra-Daten ist es mir gelungen, das Röntgenmassenprofil mithilfe der Thesen der Sphärischen Symmetrie sowie des Hydrostatischen Gleichgewichts von heißem Gas abzuleiten. Ein Vergleich zwischen den Schätzfunktionen der optischen- und Röntgenmasse erlaubte es uns, der non-thermalen Zufuhr zum Gesamtdruck, die beispielsweise durch microturbulente Gasbewegungen verursacht wurde, Grenzen zu setzen (der an die Stichprobe angegliche Wert beträgt $\approx 4\%$). Sobald die aus der Röntgenstrahlung entstandene Kreisgeschwindigkeit für die non-thermale Zufuhr korrigiert wurde, lieferte die Diskrepanz zwischen der aus der Röntgenstrahlung entstandenen Kreisgeschwindigkeit V_c^X und der optischen Kreisgeschwindigkeit für stellare Umlaufbahnen V_c^{iso} Hinweise auf die orbitale Struktur der Galaxie. Zum Beispiel würden kleine Radii $V_c^X > V_c^{iso}$ eher kreisförmigen Umlaufbahnen entsprechen, während größere Radii eher strahlenförmige Umlaufbahnen vermuten lassen. Für zwei der Galaxien in unserer Stichprobe liegt die Vermutung nahe, dass bei Radii, die größer sind als der Halblichtradius, die Umlaufbahnen vorwiegend strahlenförmig werden. Schließlich hat der Unterschied zwischen der optischen Schätzfunktion für Masse am charakteristischen Radius und derstellaren Zufuhr zur Gesamtmasse der Galaxie es uns erlaubt, den Anteil der dunklen Materie in der Galaxie abzuleiten. Der vorwiegende Anteil der dunklen Materie in unserer Stichprobe von frühen Galaxien beträgt $\approx 50\%$ für Salpeter IMF und $\approx 70\%$ für Kroupa IMF auf dem Radius, der nahe an dem Halblichtradius liegt (Kapitel 3).

Summary

The work presented here focuses on the investigation and further development of simple mass estimators for early-type galaxies which are suitable for large optical galaxy surveys with poor and/or noisy data. We consider simple and robust methods that provide an anisotropy-independent estimate of the galaxy mass relying on the stellar surface brightness and projected velocity dispersion profiles. Under reasonable assumptions a fundamental mass-anisotropy degeneracy can be circumvented without invoking any additional observational data, although at a special (characteristic) radius only, i.e these approaches do not recover the radial mass distribution. Reliable simple mass estimates at a single radius could be used (i) to cross-calibrate other mass determination methods; (ii) to estimate a non-thermal contribution to the total gas pressure when compared with the X-ray mass estimate at the same radius; (iii) to evaluate a dark matter fraction when compared with the luminous mass estimate; (iv) to derive the slope of the mass profile when combined with the mass estimate from strong lensing; (v) or as a virial mass proxy.

Two simple mass estimators have been suggested recently - the local (Churazov et al. 2010) and the global (Wolf et al. 2010) methods - which evaluate mass at a particular radius and are claimed to be weakly dependent on the anisotropy of stellar orbits. One approach (Wolf et al. 2010) uses the total luminosity-weighted velocity dispersion and evaluates the mass at a deprojected half-light radius, i.e. relies on the global properties of a galaxy. In contrast, the Churazov et al. technique uses local properties: logarithmic slopes of the surface brightness and velocity dispersion profiles, and recovers the mass at a radius where the surface brightness declines as R^{-2} (see also Richstone and Tremaine 1984, Gerhard 1993).

To test the robustness and accuracy of the methods I applied them to analytic models and to simulated galaxies from a sample of cosmological zoom-simulations which are similar in properties to nearby early-type galaxies. Both local and global simple mass estimates are found to be in good agreement with the true mass at the corresponding characteristic radius. Particularly, for slowly rotating simulated galaxies the local method gives an almost unbiased mass-estimate (when averaged over the sample) with a modest RMS-scatter of $\simeq 12\%$ (Chapter 2). When applied to massive simulated galaxies with a roughly flat velocity dispersion profile, the global approach on average also provides the almost unbiased mass-estimate, although the RMS-scatter is slightly larger ($\simeq 14 - 20\%$) than for the local estimator (Chapter 4). A noticeable scatter in the determination of the characteristic radius is also expected since the half-light radius depends on the radial range used for the

analysis and applied methodology.

Next I tested the simple mass estimators on a sample of real early-type galaxies which had previously been analyzed in detail using state-of-the-art dynamical modeling. For this set of galaxies the simple mass estimates are in remarkable agreement with the results of the Schwarzschild modeling despite the fact that some of the considered galaxies are flattened and mildly rotating. When averaged over the sample the simple local method overestimates the best-fit mass from dynamical modeling by $\approx 10\%$ with the RMS-scatter $\approx 13\%$ between different galaxies. The bias is comparable to measurement uncertainties. Moreover, it is mainly driven by a single galaxy which has been found to be the most compact one in the sample. When this galaxy is excluded from the sample, the bias and the RMS-scatter are both reduced to $\approx 6\%$. The global estimator for the same sample gives the mean deviation $\approx 4\%$ with the slightly larger RMS-scatter of $\approx 15\%$ (Chapter 4).

Given the encouraging results of the tests I apply the local mass estimation method to a sample of five X-ray bright early-type galaxies observed with the 6-m telescope BTA in Russia. Using publicly available Chandra data I derived the X-ray mass profile assuming spherical symmetry and hydrostatic equilibrium of hot gas. A comparison between the X-ray and optical mass estimates allowed me to put constraints on the non-thermal contribution (sample averaged value is $\approx 4\%$) to the total gas pressure arising from, for instance, microturbulent gas motions. Once the X-ray derived circular speed is corrected for the non-thermal contribution, the mismatch between the X-ray circular speed V_c^X and the optical circular velocity for isotropic stellar orbits V_c^{iso} provides a clue to the orbital structure of the galaxy. E.g., at small radii $V_c^X > V_c^{iso}$ would suggest more circular orbits, while at larger radii this would correspond to more radial orbits. For two galaxies in our sample there is a clear indication that at radii larger than the half-light radius stellar orbits become predominantly radial. Finally, the difference between the optical mass-estimate at the characteristic radius and the stellar contribution to the total mass permitted the derivation of a dark-matter fraction. A typical dark matter fraction for our sample of early-type galaxies is $\approx 50\%$ for Salpeter IMF and $\approx 70\%$ for Kroupa IMF at the radius which is close to the half-light radius (Chapter 3).

Chapter 1

Introduction

Since the beginning of the 20-th century mass measurements of galaxies and clusters of galaxies is a hot and actively discussed topic. Interest to ‘weighing’ galaxies and galaxies clusters has led to an extremely important discovery of dark matter. In 1933 Fritz Zwicky applied the virial theorem to the Coma galaxy cluster and found that the virial cluster mass is ≈ 400 times greater than the ‘visual’ mass estimated from the total brightness of the cluster. Zwicky calculations suggested that there must be some form of an unseen matter (‘dark matter’) which would be able to hold the cluster galaxies together. First observations of spiral galaxies rotation curves (Babcock, 1939; Mayall, 1951) showed no Keplerian velocity decrease in the outer regions in contradiction to expectations. This observation also had no significant influence on scientific community, rather details of the analysis (e.g., adopted distances) were questioned. Most astronomers in the $\sim 50 - 60$ s kept believing that disk galaxies had Keplerian velocities at moderate and large distances from the center. Thanks to progress in instrumentation, observations of hundreds extended rotation curves became available in ~ 1980 s, majority of which demonstrated no Keplerian velocity fall. This fact played a major role in convincing the scientific community that there exist an unseen (dark) matter which accounts for a major part of the total mass of disk galaxies. It took $\simeq 50$ years to make the paradigm of the dark matter common and widely accepted. Dark matter emit/absorb electromagnetic radiation very weakly (if at all) and interacts with ordinary matter mainly gravitationally. Unfortunately, up to now there is no reliable detection of dark matter particles in the Earth experiments, and galaxies and galaxy clusters retain the status of main laboratories for investigation of dark matter properties.

Apart from the dark matter studies mass determination of galaxies are crucial for understanding their formation and evolution processes. The current Λ Cold Dark Matter cosmological paradigm predicts a hierarchical growth of structures in the Universe. Small overdensities collapse first, then the resulting dark matter ‘clumps’ merge together and finally form large halos which serve as ‘cradles’ for galaxy formation. One of the predictions of the Λ CDM model is that the structural parameters of galaxies correlate with properties of massive parent dark matter haloes which are in turn tightly coupled with the halo mass (e.g., Mo, Mao and White, 1998; Macciò, Dutton and van den Bosch, 2008, and references

therein).

1.1 Mass determination techniques

A number of techniques have been developed in the past to investigate the mass distributions in early-type galaxies. Each method has its own set of assumptions and limitations. Comparison of mass profiles inferred from different techniques is necessary to get reliable estimates and to control systematic uncertainties, inherent in all methods. It also leads to interesting constraints on properties of elliptical galaxies, when possible biases are well understood and systematic errors are under control. Let us briefly describe main approaches for analysis of early-type galaxies.

1.1.1 X-ray analysis

Massive elliptical galaxies (and galaxy clusters) are bright X-rays sources as found by the Einstein X-ray observatory (Figure 1.1 shows an example of a X-ray image of a galaxy cluster). X-ray observations of hot diffuse gas in these galaxies (as well as in galaxy clusters) allows one to probe the galaxy gravitational potential out to ~ 10 kpc ($\sim 10R_{1/2}$; $R_{1/2}$ is the optical half-light radius) where observations in optical or radio bands are extremely challenging. Assuming hydrostatic equilibrium and spherical symmetry, with known (obtained from observations) gas number density $n(r)$ and temperature $T(r)$ profiles, one can estimate the galaxy mass:

$$\frac{1}{\rho} \frac{dP}{dr} = -\frac{d\Phi}{dr} = \frac{GM(< r)}{r^2} \quad (1.1)$$

$$M(< r) = -\frac{kTr}{G\mu m_p} \left(\frac{d \ln n}{d \ln r} + \frac{d \ln T}{d \ln r} \right), \quad (1.2)$$

where $\rho = \mu m_p n$ is the gas density (m_p stands for the proton mass, μ for the mean atomic weight), $P = nkT$ is the thermal gas pressure (k is the Boltzmann constant) and $\Phi(r)$ is the gravitational galaxy potential.

Strictly speaking, the hot coronae of elliptical galaxies could deviate from the spherical symmetry. Although, a spherical averaging of ellipsoidal objects is shown to introduce only a small (orientation-averaged) bias for not too flat models (e.g. Buote and Humphrey, 2012). The equation (1.1) does not also account for possible non-thermal contribution to the gas total pressure, arising from, for instance, turbulent motions, cosmic rays, magnetic fields, etc (e.g., Churazov et al., 2008). E.g., numerical simulations suggest that in relaxed systems the non-thermal support is at the level of 5 - 35% of the total gas pressure (e.g. Nagai, Vikhlinin and Kravtsov, 2007; Lau, Kravtsov, Nagai, 2009; Zhuravleva et al., 2013). Comparing X-ray mass estimates with other methods could provide constraints on the contribution of the non-thermal components to the total gas pressure.

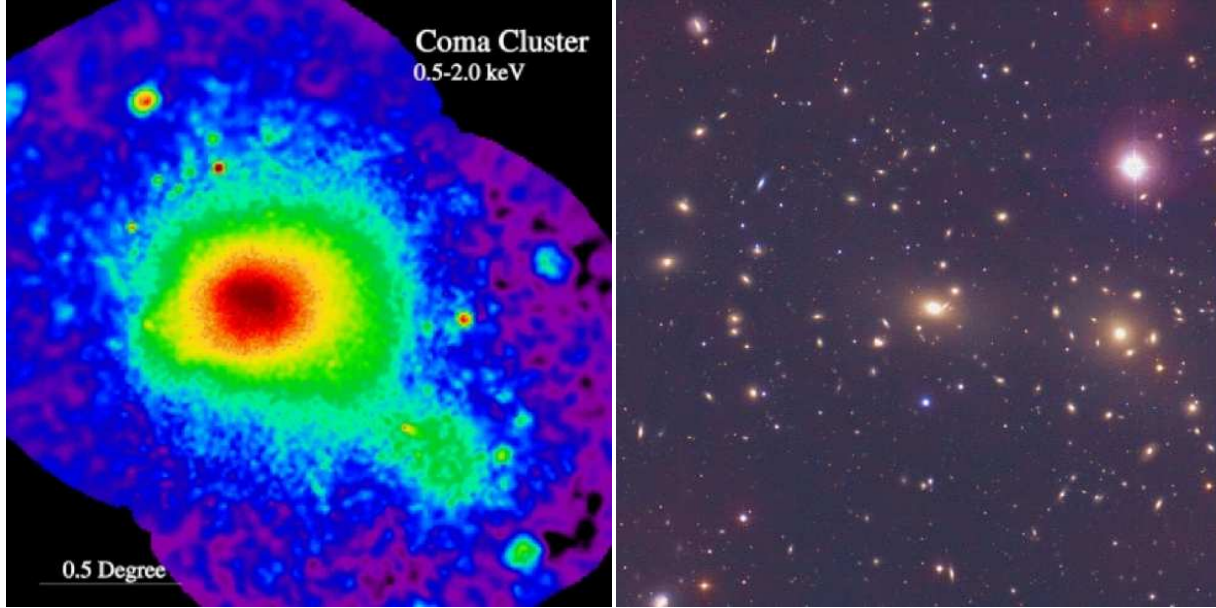


Figure 1.1: Hot X-ray emitting gas in the Coma cluster of galaxies as seen by ROSAT satellite is shown on the left (image credit: S.L. Snowden/ROSAT/MPE). The optical image of is on the right (image credit: O. Lopez-Cruz and I. Shelton/NOAO/AURA/NSF).

1.1.2 Gravitational lensing

Gravitational lensing - bending the light rays by gravitational field - is the only method of mass determination, which can be applied to objects regardless of their composition and dynamical state (relaxed or disturbed). Depending on the deflection angle of light, gravitational lensing is divided into two regimes: strong and weak. If the source is a subject to strong lensing, the observer sees multiple images of the source and/or ring-like structures (Figure 1.2). Measuring the angular separation of images one can get an independent estimate of the total mass inside a cylinder with the Einstein radius $R_E = \sqrt{\frac{4GM D_d(D_s - D_d)}{c^2 D_s}}$, where G is the gravitational constant, c - speed of light, M - the lens mass, D_d and D_s are the distances from the observer to the lens and to the source respectively. Strong lensing offers an opportunity to infer the Hubble constant H by measuring the time delay between the source images and reconstructing a geometry of the gravitationally lensed system. An advantage of such method for the Hubble constant determination is that it probes directly the geometric scale of the system.

In the weak lensing regime only distortions of size and shape (tangential ‘stretching’) of background sources are observed. Weak lensing allows one to investigate the shape of the gravitational potential and map the dark matter distribution at large radii where other methods are not applicable, although an amplitude of background galaxies distortions due to the weak lensing is comparable to the telescope aberrations. Currently the weak lensing techniques are very promising for cosmological studies (to probe dark energy) and rapidly

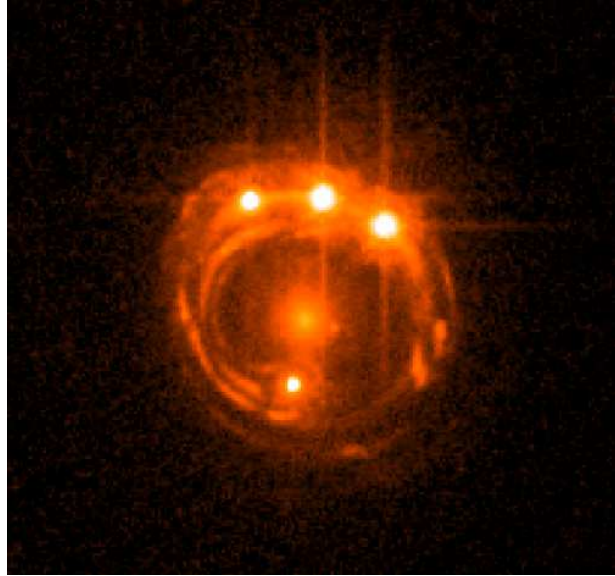


Figure 1.2: Example of a strong gravitational lensing. The quasar RXJ1131-123 as seen by the Hubble Space Telescope. Due to gravitational lensing the quasar appears as four point-like images connected by an Einstein ring. The lens galaxy is at the center of the ring.

developing.

1.1.3 Dynamical modeling

All methods that are based on modeling kinematic data of elliptical galaxies suffer from the fundamental degeneracy between the galaxy mass and the anisotropy of tracer orbits. The interpretation of the observed velocity dispersion profile $\sigma_p(R)$ alone is found to be ambiguous due to the lack of single ideal tracers on known orbits.

Dynamical modeling using orbit superposition (Schwarzschild method, 1979) is considered to be the state-of-the-art technique for the investigation of early-type galaxies which recovers the galaxy's gravitational potential and orbital structure with an accuracy of $\lesssim 15\%$ (e.g., Thomas et al., 2005).

Schwarzschild (1979) introduced a numerical orbit-superposition technique to construct collisionless phase-space distribution functions of tracers in dynamical equilibrium. The basic idea of the method is that an elliptical galaxy is considered as a bound system of individual stars, all possible orbits of which could be defined from the integrals of motion. In brief, the Schwarzschild method consists of several steps: (i) firstly, in a trial gravitational potential one composes a library of stellar orbits which correspond to all possible initial positions in the six-dimensional phase-space; (ii) then one constructs the superposition of all orbits which describes the observed distribution of surface brightness $I(R)$ and kinematic profiles ($\sigma_p(R)$ and higher moments) as good as possible. (iii) Finally,

parameters of the gravitational potential are varied, and the whole procedure is carried out again as long as the deviation of the resulting model from observational data reaches the minimum value.

The Schwarzschild technique allows one to obtain a radial distribution of a galaxy mass, to study the contribution of individual components (luminous matter, dark halo and supermassive black hole) to the galaxy gravitational potential. The method can be applied to any steady-state collisionless system. No assumptions on the orbit configuration is required. Derived distribution function in the six-dimensional phase space is guaranteed to be everywhere positive (= to be physically meaningful). The main challenge is to construct a representative library of orbits. The orbit-superposition technique is widely used for determining the mass distribution, dark matter fraction and orbit configuration of nearby early-type galaxies as well as for ‘weighing’ central black holes. The method is very sensitive to the quality and completeness of the observational data, and not all the model parameters are uniquely constrained. It is also computationally expensive. E.g. the Schwarzschild orbit-superposition analysis of the nearby massive elliptical galaxy M87 took over ~ 37500 hours of cpu (Gebhardt and Thomas, 2009).

As the sophisticated detailed modeling requires high signal-to-noise observational data on the line-of-sight velocity moments it is applicable only to nearby galaxies. Large astronomical surveys of galaxies at different redshifts are extremely important for galaxy formation and mass assembly studies. For such surveys usage of detailed dynamical modeling is not practical/possible especially in a case of poor and/or noisy observational data. It is desirable to have simple and robust techniques based on the most basic observables that provide an unbiased mass estimate with a modest scatter.

Before moving to simple mass estimators let us note that recent studies based on different approaches and their combinations suggest that the gravitational potential $\Phi(r)$ of massive elliptical galaxies is close to isothermal (e.g. Gerhard et al., 2001; Treu et al., 2006; Koopmans et al., 2006; Fukazawa et al., 2006; Churazov et al., 2010).

1.2 The simple(st) mass estimators

1.2.1 The virial theorem and virial-like estimators

Despite an enormous progress in a development of mass determination techniques, the scalar virial theorem is still widely used for analyzing spheroidal systems especially at high redshifts where detailed high-quality observational data are not available. The total mass of an isolated spherical system in a steady state can be expressed as (Binney and Tremaine, 2008)

$$M = 3 \frac{\langle \sigma_p^2 \rangle r_g}{G}, \quad (1.3)$$

where G is the gravitational constant, r_g is called the gravitational radius and the luminosity-weighted average line-of-sight velocity dispersion is defined as

$$\langle \sigma_p^2 \rangle = \frac{\int_0^\infty \sigma_p^2(R) I(R) R dR}{\int_0^\infty I(R) R dR}. \quad (1.4)$$

Apart from its simplicity the main advantage of the scalar virial theorem is its independence from the anisotropy β of tracers' orbits. Unfortunately, the value of r_g depends on the total and luminous mass distribution of a system, making the formula (1.3) not practical for mass determination of real systems. One way to overcome this problem is to express the gravitational radius in terms of observationally available half-light radius $R_{1/2}$ under some assumptions on a stellar density. Spitzer (1969) noticed that a ratio between a 3D half light radius and the gravitational radius $r_{1/2}/r_g \approx 0.4 \pm 0.2$ for different polytropes (for polytropic index between 3 and 5). This result has been confirmed by Mamon (2000); Łokas and Mamon (2001), who theoretically derived $r_{1/2}/r_g \approx 0.403$ for the Hernquist (1990) model. For a wide range of stellar light profiles (Sérsic, exponential, Plummer, King) the 3D half light radius $r_{1/2}$ is related to the projected half light radius $R_{1/2}$ as $r_{1/2} \approx 1.3R_{1/2}$ (Ciotti, 1991; Spitzer, 1987). So the relation (1.3) can be rewritten as

$$M \approx 1.6 \frac{\langle \sigma_p^2 \rangle R_{1/2}}{G} \quad (1.5)$$

for common analytical stellar density profiles.

Another way to get rid of r_g in the equation (1.3) is to assume the isothermal form of a gravitational potential $\Phi(r) = V_c^2 \ln r + const$. As mentioned above, approximate isothermality of elliptical galaxies is suggested by a number of recent independent studies on kinematics, X-rays and gravitational lensing. Assuming $V_c(r) = const$ the virial theorem further simplifies to

$$M(< r) = 3 \frac{\langle \sigma_p^2 \rangle r}{G}, \quad (1.6)$$

giving the radial total mass profile which is based on a single observable quantity and rigorously independent of the anisotropy parameter β .

In any form the virial theorem approach requires determination of the luminosity-weighted square of the projected velocity dispersion over the entire galaxy or within large enough aperture. How large should be an aperture radius to ensure that $\sigma_{ap}^2(R_{ap}) = \frac{\int_0^{R_{ap}} \sigma_p^2(R) I(R) R dR}{\int_0^{R_{ap}} I(R) R dR}$ is insensitive to the anisotropy, i.e. $\sigma_{ap}^2 \approx \langle \sigma_p^2 \rangle$? Consider, for example, a spherical galaxy composed of isotropic (the anisotropy parameter $\beta = 0$), pure radial ($\beta = 1$) and pure circular ($\beta \rightarrow -\infty$) orbits in an isothermal gravitational potential. As the anisotropy parameter varies between $-\infty$ and 1 the two latter cases are somewhat extreme and show an expected range of variations of observables due to the unknown anisotropy. Figure 2.10 shows the aperture velocity dispersion $\sigma_{ap}(R)$ as a function of the aperture radius. The aperture velocity dispersions for different anisotropies are shown in blue ($\beta = 0$), green ($\beta = 1$) and magenta ($\beta \rightarrow -\infty$). For the de Vaucouleurs's surface

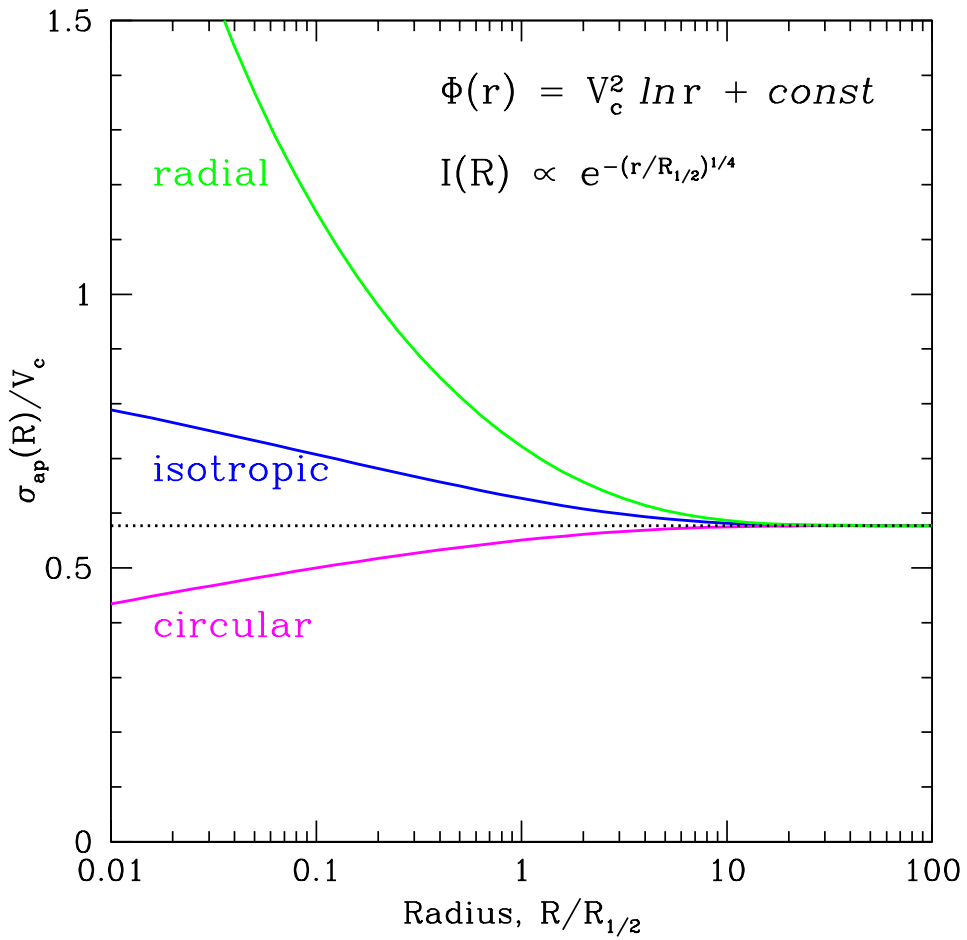


Figure 1.3: Aperture velocity dispersion σ_{ap} as a function of aperture radius (normalized to the half-light radius) for a spherical galaxy described by the de Vaucouleurs law $I(R) \propto e^{-7.67(R/R_{1/2})^4}$ and an isothermal gravitational potential $\Phi(r) = V_c^2 \ln r + \text{const}$. The curves show the observed aperture velocity dispersion for different values of the anisotropy parameter: $\beta = 0$ (in blue), $\beta \rightarrow -\infty$ (in magenta) and $\beta = 1$ (in green). The minimum aperture radius required to get a reliable estimate of $\langle \sigma_p^2 \rangle$ is $\sim 10R_{1/2}$. Adapted from Churazov et al. (2010).

brightness distribution these three curves converge to the same value $\sigma_{ap} \approx \sqrt{\langle \sigma_p^2 \rangle} = V_c/\sqrt{3}$ at very large aperture radius (~ 10 half-light radii). For smaller aperture radii the σ_{ap} is very sensitive to the anisotropy and can not be used as approximation for $\sqrt{\langle \sigma_p^2 \rangle}$. Large apertures are available mostly for distant galaxies. For nearby ellipticals velocity dispersion profiles are typically observed out to $\sim 1 - 2$ effective radii.

Having the surface brightness distributions and integral field kinematics of 25 nearby early-type galaxies Cappellari et al. (2006) calibrated the virial-like mass estimator in a form

$$M(< r_{1/2}) = k \frac{\langle \sigma_p^2 \rangle_e r_{1/2}}{G}, \quad (1.7)$$

where $\langle \sigma_p^2 \rangle_e = \sigma_e^2$ is the luminosity-weighted line-of-sight velocity dispersion calculated within a projected circular aperture of radius equal to an effective (half-light) radius $R_{1/2}$. Comparing the simple virial-like mass estimators with masses from an axisymmetric Schwarzschild models constructed for the same sample of galaxies, the coefficient $k \approx 2.5$ has been derived, i.e. the mass within the 3D effective radius $r_{1/2}$ can be approximated as

$$M(< r_{1/2}) \approx 1.9 \frac{\sigma_e^2 r_{1/2}}{G} \approx 2.5 \frac{\sigma_e^2 R_{1/2}}{G}, \quad (1.8)$$

where $r_{1/2} \approx 1.33R_{1/2}$ used. Note this virial-like mass estimator implies the certain methodology of $R_{1/2}$ and σ_e measurements (for details see Cappellari et al. 2006). The half-light radius and a total galaxy luminosity are obtained from a fit of $R^{1/4}$ (de Vaucouleurs) growth curves to the aperture photometry and the σ_e is measured in a circular aperture of radius $R_{1/2}$ centered on the galaxy.

1.2.2 Estimators based on the spherical Jeans equation

Another common approach to mass determination of elliptical galaxies is to use the stationary non-streaming spherical Jeans equation which describes the motion of a collisionless system of test particles in a gravitational potential $\Phi(r)$. The Jeans equation relates together the anisotropy parameter β , a volume density of tracers $j(r)$ and a radial velocity dispersion $\sigma_r(r)$ (Binney and Tremaine, 2008):

$$\frac{d}{dr} (j\sigma_r^2) + 2\frac{\beta}{r} j\sigma_r^2 = -j \frac{d\Phi}{dr}, \quad (1.9)$$

where the anisotropy $\beta(r) = 1 - \sigma_t^2/\sigma_r^2$ (see Figure 1.4) for the spherically symmetric case ($\sigma_t(r)$ is the tangential velocity dispersion). For a given $\beta(r)$ one can derive $M(< r)$ from the Jeans equation linking $j(r)$ and $\sigma_r(r)$ to the observable surface brightness $I(R)$ and projected velocity dispersion $\sigma_p(R)$ via the structural projection equation

$$I(R) = 2 \int_R^\infty \frac{j(r)r dr}{\sqrt{r^2 - R^2}}, \quad (1.10)$$

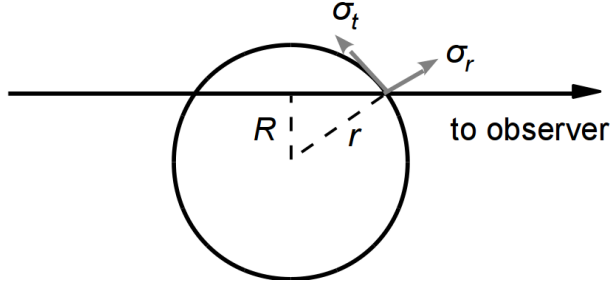


Figure 1.4: Projection of a spherical system along the line of sight. r is the 3D radius, R stands for the projected radius, σ_t and σ_r are the radial and tangential velocity dispersions respectively.

and the anisotropic kinematic projection equation (Binney and Mamon, 1982)

$$\sigma_p^2(R)I(R) = 2 \int_R^\infty \left(1 - \frac{R^2}{r^2}\beta\right) \frac{j(r)\sigma_r^2 r dr}{\sqrt{r^2 - R^2}}. \quad (1.11)$$

For isotropic distribution of tracers' orbits ($\beta = 0$) one can solve the spherical Jeans equation (1.9) and relate the mass $M(< r)$ to the observables ($I(R)$ and $\sigma_p(R)$) via the isotropic mass inversion equation (Mamon and Boué, 2010):

$$M(< r) = -\frac{r}{\pi G j(r)} \int_r^\infty \frac{d^2(I\sigma_p^2)}{dR^2} \frac{R dR}{\sqrt{R^2 - r^2}}, \quad (1.12)$$

where a 3D stellar density is obtained from the Abel inversion equation:

$$j(r) = -\frac{1}{\pi} \int_r^\infty \frac{dI}{dR} \frac{dR}{\sqrt{R^2 - r^2}}, \quad (1.13)$$

In general, for any known anisotropy profile the equation of anisotropic kinematic projection (1.11) can be inverted to yield the radial velocity dispersion profile $\sigma_r(r)$, thus allowing one to derive the mass distribution of a spherical galaxy through the Jeans equation (1.9) in terms of double integrals of observable profiles $I(R)$ and $\sigma_p(R)$ (Mamon and Boué, 2010). Unfortunately, there is no direct and reliable way to derive $\beta(r)$ from observational data without invoking an expensive detailed modelling.

Richstone and Tremaine (1984) emphasized that the galaxy mass and the anisotropy still can be disentangled from the Jeans equation under some reasonable assumptions. For a spherical galaxy described by the de Vaucouleurs's surface brightness distribution $I(R) \propto e^{-7.67(R/R_{1/2})^4}$ and a constant mass-to-light ratio, values of the observed velocity dispersion (obtained from the Schwarzschild analysis) for isotropic, circular and radial orbits are quite similar at some particular radius (see Figure 1 in Richstone and Tremaine 1984 and Figure 1.5), suggesting that at this radius the galaxy mass estimate is minimally affected by the unknown anisotropy. Based on studies of stellar velocity profiles in the

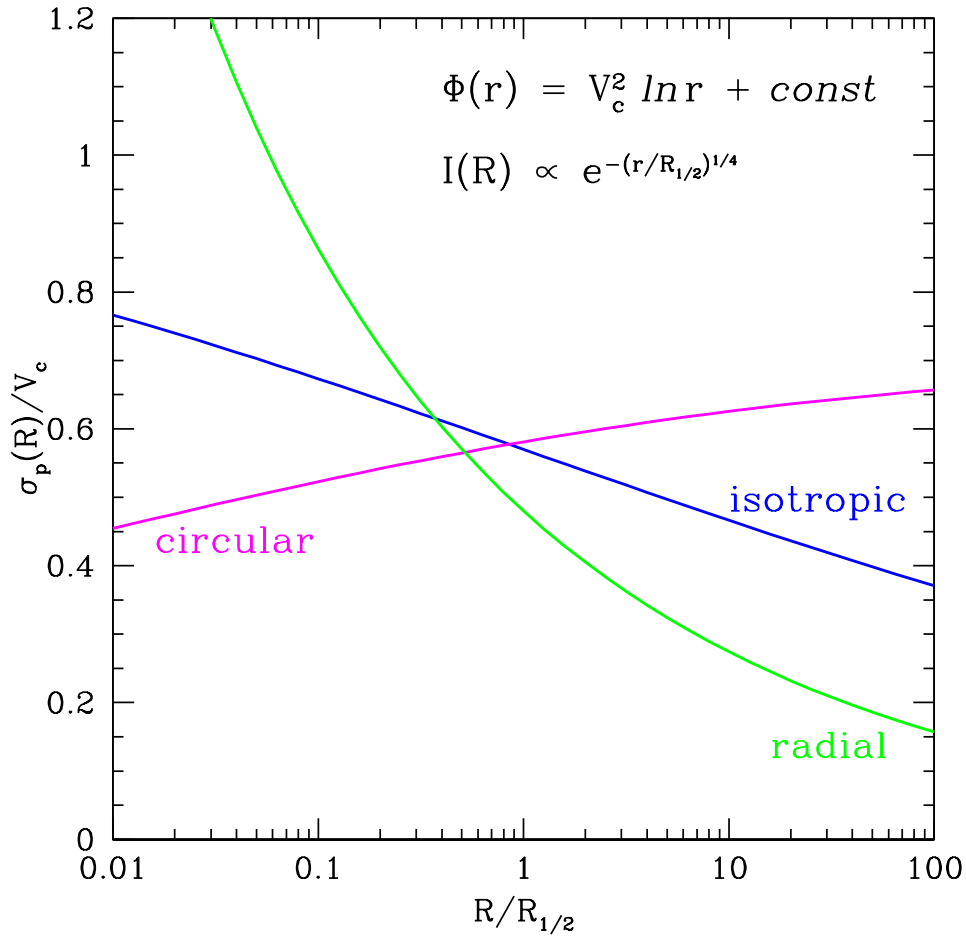


Figure 1.5: Projected velocity dispersion as a function of radius (normalized to the half-light radius) for a spherical galaxy described by the de Vaucouleurs's surface brightness profile and isothermal gravitational potential. The curves show the observed velocity dispersion for isotropic (blue), circular (magenta) and radial (green) orbits. There exist a special radius at which sensitivity to the anisotropy is minimal. Adapted from Churazov et al. (2010).

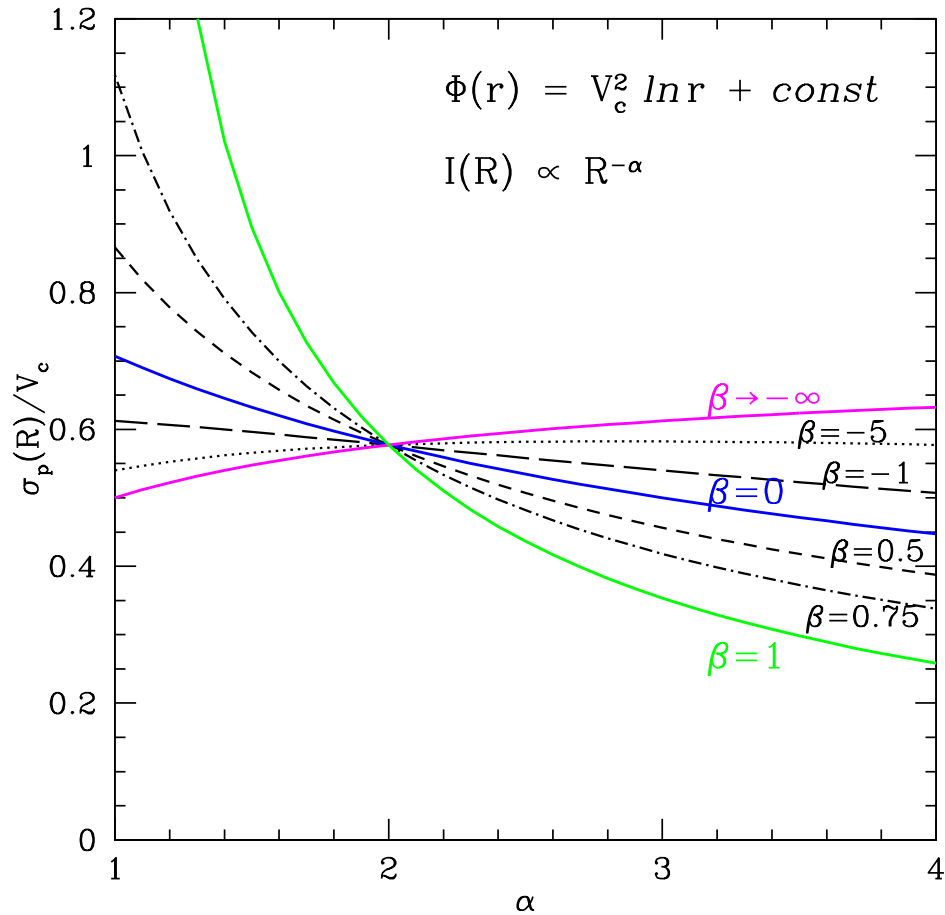


Figure 1.6: Projected velocity dispersion as a function of α for a spherical galaxy described by the pure power-law surface brightness $I(R) \propto R^{-\alpha}$ profile and isothermal gravitational potential. The curves show the observed velocity dispersion for different values of the anisotropy parameter β . Adapted from Churazov et al. (2010).

isothermal gravitational potential Gerhard (1993) noticed that for the pure power-law surface brightness profile $I(R) \propto R^{-\alpha}$ the projected velocity dispersion does not depend on the anisotropy for $\alpha = 2$ (Figure 1.6). Combining these two notes, Churazov et al. (2010) proposed a simple mass estimator which determines the galaxy mass at the special radius which is close to R_2 where $I(R)$ declines as $\propto R^{-2}$. From the spherical Jeans equation (1.9) assuming $\Phi(r) = V_c^2 \ln r + \text{const}$ one can derive an analytic relation between the circular speed ($V_c^2(r) = GM(< r)/r$) and the local properties of $I(R)$ and $\sigma_p(R)$ for the cases of isotropic ($\beta = 0$), circular ($\beta \rightarrow -\infty$) and radial ($\beta = 1$) orbits:

$$\begin{aligned} V_c^{\text{iso}} &= \sigma_p(R) \cdot \sqrt{1 + \alpha + \gamma} \\ V_c^{\text{circ}} &= \sigma_p(R) \cdot \sqrt{2 \frac{1 + \alpha + \gamma}{\alpha}} \\ V_c^{\text{rad}} &= \sigma_p(R) \cdot \sqrt{(\alpha + \gamma)^2 + \delta - 1}, \end{aligned} \quad (1.14)$$

where

$$\alpha \equiv -\frac{d \ln I(R)}{d \ln R}, \quad \gamma \equiv -\frac{d \ln \sigma_p^2}{d \ln R}, \quad \delta \equiv \frac{d^2 \ln [I(R) \sigma_p^2]}{d (\ln R)^2}. \quad (1.15)$$

A radius where V_c^{iso} , V_c^{circ} and V_c^{rad} have similar values is the special radius where sensitivity of the method to the anisotropy β is expected to be minimal. Note, that for $\sigma_p = \text{const}$ and not very steep surface brightness profiles ($\delta \ll \alpha$) the equations (1.14) can be simplified to:

$$\begin{aligned} V_c^{\text{iso}} &= \sigma_p(R) \cdot \sqrt{\alpha + 1} \\ V_c^{\text{circ}} &= \sigma_p(R) \cdot \sqrt{2 \frac{\alpha + 1}{\alpha}} \\ V_c^{\text{rad}} &= \sigma_p(R) \cdot \sqrt{\alpha^2 - 1}. \end{aligned} \quad (1.16)$$

So for nearly flat velocity dispersion profiles in the isothermal gravitational potential the galaxy circular speed (or mass) could be estimated at the radius R_2 where $I(R) \propto R^{-2}$, as pointed out by Gerhard (1993). For varying line-of-sight velocity dispersion one can get an anisotropy independent estimate of the circular speed using the local properties of the observed $I(R)$ and $\sigma_p(R)$ profiles at the radius where analytic V_c -profiles from the equations (1.14) have similar values.

While equations (1.14), (1.16) are derived under the assumption of $V_c(r) = \text{const}$, tests on model spherical ‘galaxies’ with non-logarithmic potentials, non-power law behaviour of the surface brightness profile and varying anisotropy parameter and tests on a sample of cosmological zoom-simulations of individual galaxies (Churazov et al., 2010; Lyskova et al., 2014b) have shown that the circular speed can still be recovered to a reasonable accuracy.

A similar approach has been suggested by Wolf et al. (2010) who derived the simple mass estimator by manipulating the spherical Jeans equation (1.9) and the scalar virial theorem. Wolf et al. (2010) noticed that for spherical systems with roughly constant $\sigma_p(R)$,

the mass within the radius r_3 where $j(r) \propto r^{-3}$ (which is close to $r_{1/2} \approx 1.33R_{1/2}$) is almost independent of the assumed $\beta(r)$ and can be approximated as

$$M(< r_3) \approx 4 \frac{\langle \sigma_p^2 \rangle R_{1/2}}{G}. \quad (1.17)$$

In contrast to the Churazov et al. ('local') approach, this estimator requires averaging of the velocity dispersion out the the virial radius of the system and determination of the projected half-light radius, i.e. depends on the global galaxy properties. For the pure power-law surface brightness distribution and isothermal gravitational potential both methods gives the same circular speed estimate $V_c = \sqrt{3\sigma_p(R_2)} = \sqrt{3\langle \sigma_p^2 \rangle}$ at the special radius $R_2 = r_3$.

1.3 Structure of the thesis

This thesis aims to investigate and further develop simple mass estimators for early-type galaxies which could be applied to analysis of large optical galaxy surveys.

Chapter 1 gives results of extensive tests of the local mass estimator on a sample of 65 cosmological zoom-simulations of individual galaxies. It is also demonstrated that the simple method could be successfully applied to galaxy clusters where individual galaxies are used as mass tracers.

The application of the simple optical mass estimator to real X-ray bright elliptical galaxies is discussed in Chapter 2. Comparison of the simple estimate with the X-ray based and luminous mass profiles allows one to put constraints on the gas physics and configuration of stellar orbits. In this Chapter I estimate the magnitude of the non-thermal microturbulent motions of the hot gas, disentangle stellar and dark matter contributions to the total mass and characterize the distribution of stellar orbits for the analyzed sample of galaxies.

Chapter 3 presents a comparison of the simple local method with the global approach suggested by Wolf et al. (2010). To compare the methods I test them on a grid of analytical models, on samples of simulated galaxies and real early-type galaxies that had been already modelled using the Schwarzschild orbit superposition technique. A possibility to use the simple estimates as a proxy for a virial galaxy mass is also discussed.

The main findings are summarized in Conclusions.

Bibliography

- Babcock H.W. 1939, Lick Obs. Bull., 19, 41
- Binney J., Mamon G.A. 1982, MNRAS 200, 361
- Binney J., Tremaine S. 2008, Galactic Dynamics, 2nd edn. (Princeton University Press)
- Buote D. A., Humphrey P. J. 2012, MNRAS, 421, 1399
- Cappellar M., Bacon R., Bureau M., Damen M. C., Davies R. L., de Zeeuw P. T., Emsellem E., Falcón-Barroso J., Krajnović D., Kuntschner H., McDermid R. M., Peletier R. F., Sarzi M., van den Bosch R. C. E., van de Ven G. 2006, MNRAS, 366, 1126
- Churazov E., Forman W., Vikhlinin A., Tremaine S., Gerhard O., Jones C. 2008, MNRAS, 388, 1062
- Churazov E., Tremaine S., Forman W., Gerhard O., Das P., Vikhlinin A., Jones C., Böhringer H., Gebhardt K. 2010, MNRAS, 404, 1165
- Ciotti L. 1991, A&A, 249, 99
- Fukazawa Y., Botoya-Nonesa J. G., Pu J., Ohto A., Kawano N. 2006, AJ, 636, 698
- Gebhardt K., Thomas J. 2009, ApJ, 700, 1690
- Gerhard O.E. 1993, MNRAS, 265, 213
- Gerhard O., Kronawitter A., Saglia R. P., Bender R. 2001, AJ, 121, 1936
- Hernquist L. 1990, ApJ, 356, 359
- Koopmans L. V. E., Treu T., Bolton A. S., Burles S., Moustakas L. A. 2006, ApJ, 649, 599
- Lau E. T., Kravtsov A. V., Nagai D. 2009, ApJ, 705, 1129
- Lokas E.L., Mamon G.A. 2001, MNRAS, 321, 155
- Lyskova N. et al., in prep.

- Macciò A.V., Dutton A.A., van den Bosch F.C. 2008, MNRAS, 391, 1940
- Mamon G.A. 2000, in Combes F., Mamon G. A., Charmandaris V., eds, ASP Conf. Ser. Vol. 197, Dynamics of Galaxies: from the Early Universe to the Present. Astron. Soc. Pac., San Francisco, p. 377
- Mamon G.A. and Boué G. 2010, MNRAS, 401, 2433
- Mayall N.U. 1951, in The Structure of the Galaxy (Ann Arbor: Univ. Michigan Press), 19
- Mo H.J., Mao S., White S. D. M. 1998, MNRAS, 295, 319
- Nagai D., Vikhlinin A., Kravtsov A. V. 2007, ApJ, 655 98
- Richstone D. O., Tremaine S. 1984, ApJ 286, 27
- Schwarzschild M. 1979, ApJ, 232, 236
- Spitzer L.J. 1969, ApJ, 158, L139
- Spitzer L.J. 1987, Dynamical Evolution of Globular Clusters. Princeton Univ. Press, Princeton, NJ, p. 191
- Thomas J., Saglia R.P., Bender R., Thomas D., Gebhardt K., Magorrian J., Corsini E.M., Wegner J. 2005, MNRAS, 360, 1355
- Treu T., Koopmans L. V., Bolton A. S., Burles S., Moustakas L. A. 2006, ApJ, 640, 662
- Wolf J., Martinez G.D., Bullock J.S., Kaplinghat M., Geha M., Muñoz R.R., Simon J.D., Avedo F.F. 2010, MNRAS, 406, 1220
- Zhuravleva I., Churazov E., Kravtsov A., Lau E. T., Nagai D., Sunyaev R. 2013, MNRAS, 428, 3274
- Zwicky F. 1933, Helv. Phys. Acta, 6, 110

Chapter 2

Testing a simple recipe for estimating galaxy masses from minimal observational data.

Based on Mon.Not.R.Astron.Soc., 2012, 423, 1813

N.Lyskova, E.Churazov, I.Zhuravleva, T. Naab, L. Oser, O. Gerhard, X. Wu

and on Astron. Nachr., 2013, 4-5, 360

N.Lyskova

Abstract.

The accuracy and robustness of a simple method to estimate the total mass profile of a galaxy is tested using a sample of 65 cosmological zoom-simulations of individual galaxies. The method only requires information on the optical surface brightness and the projected velocity dispersion profiles and therefore can be applied even in case of poor observational data. In the simulated sample massive galaxies ($\sigma \simeq 200 - 400 \text{ km s}^{-1}$) at redshift $z = 0$ have almost isothermal rotation curves for broad range of radii (RMS $\simeq 5\%$ for the circular speed deviations from a constant value over $0.5R_{\text{eff}} < r < 3R_{\text{eff}}$). For such galaxies the method recovers the unbiased value of the circular speed. The sample averaged deviation from the true circular speed is less than $\sim 1\%$ with the scatter of $\simeq 5 - 8\%$ (RMS) up to $R \simeq 5R_{\text{eff}}$. Circular speed estimates of massive non-rotating simulated galaxies at higher redshifts ($z = 1$ and $z = 2$) are also almost unbiased and with the same scatter. For the least massive galaxies in the sample ($\sigma < 150 \text{ km s}^{-1}$) at $z = 0$ the RMS deviation is $\simeq 7 - 9\%$ and the mean deviation is biased low by about $1 - 2\%$. We also derive the circular velocity profile from the hydrostatic equilibrium (HE) equation for hot gas in the simulated galaxies. The accuracy of this estimate is about RMS $\simeq 4 - 5\%$ for massive objects ($M > 6.5 \times 10^{12} M_{\odot}$) and the HE estimate is biased low by $\simeq 3 - 4\%$, which can be traced to the presence of gas motions. This implies that the simple mass estimate can be used to determine the mass of observed massive elliptical galaxies to an accuracy of 5–8% and can be very useful for galaxy surveys.

2.1 Introduction

The accurate determination of galaxy masses is a crucial issue for galaxy formation and evolution models. Disentangling dark matter and baryonic matter of a galaxy permits testing the predictions of Λ CDM-cosmology and probing the mass function. An algorithm for deriving the mass of a spiral galaxy is straight forward - one just need to measure a rotation curve from gas or stars that can be safely assumed to be on circular orbits. For elliptical galaxies the situation is less simple. There is no ‘perfect’ (in terms of accuracy) tracer to measure the total gravitational potential. The main problem is the degeneracy between the anisotropy of stellar orbits and the mass. The shape of stellar orbits is not known a priory and different combinations of orbits may give the same distribution of light. Several different approaches for mass determination were proposed and successfully implemented, like strong and weak lensing (e.g. Gavazzi et al., 2007; Mandelbaum et al., 2006), modelling of X-ray emission of hot gas in galaxies (e.g. Humphrey et al., 2006; Churazov et al., 2008), Schwarzschild modelling of stellar orbits, etc. Accurate data on the projected line-of-sight velocity distribution with information on higher-order moments enables an accurate determination of the mass distribution for nearby ellipticals (e.g. Gerhard et al., 1998; Thomas et al., 2011). However, in case of minimal available data detailed modelling is often not possible. Therefore it is important to find a method to measure galaxy masses with reasonable accuracy which gives an unbiased estimate when averaged over a large number of galaxies. In particular, it can be extremely useful while analysing large surveys, especially at high redshifts when detailed observational data of each individual galaxies are often not available.

The simplest way of estimating the mass of a galaxy is based on the projected velocity dispersion in a fixed aperture (e.g. Cappellari et al., 2006). A slightly more complicated approach is described in Churazov et al. (2010). To estimate the mass the only information required is the light profile and either the dispersion profile measurement or at least a reliable dispersion measurement at some radius. Testing this particular method on a sample of simulated galaxies is the subject of this paper. The main questions that we want to address are (i) What is the accuracy of this method? (ii) Does it give an unbiased result? (iii) What are the restrictions for application of this method?

The structure of the paper is as follows. In section 2.2, we provide a brief description of the method. In section 2.3 we describe the sample of simulated galaxies which is used to test the method. The analysis of the accuracy of the method is presented in section 2.4 where we also discuss alternative methods for determining the circular velocity. A summary on the bias and accuracy of the various methods is given in section 2.6 with conclusions in section 2.7.

2.2 Description of the method

The main idea of the method is described in Churazov et al. (2010). Here we just provide a brief summary.

The method is based on the stationary non-streaming spherical Jeans equation:

$$\frac{d}{dr} j \sigma_r^2 + 2 \frac{\beta}{r} j \sigma_r^2 = -j \frac{d\Phi}{dr}, \quad (2.1)$$

where $j(r)$ ¹ is the stellar luminosity density, $\sigma_r(r)$ is the radial component of the velocity dispersion tensor (weighted by luminosity), $\beta(r) = 1 - \sigma_\theta^2/\sigma_r^2$ is the stellar anisotropy parameter ($\sigma_\theta = \sigma_\phi$ because of the assumed spherical symmetry) and $\Phi(r)$ is the gravitational potential of a galaxy.

While the stellar luminosity density $j(r)$ and radial dispersion $\sigma_r(r)$ can not be observed directly they contribute to the two-dimensional surface brightness $I(R)$ and the velocity dispersion $\sigma(R)$ profiles:

$$I(R) = 2 \int_R^\infty \frac{j(r)r dr}{\sqrt{r^2 - R^2}}, \quad (2.2)$$

$$\sigma^2(R) \cdot I(R) = 2 \int_R^\infty j(r) \sigma_r^2(r) \left(1 - \frac{R^2}{r^2} \beta(r)\right) \frac{r dr}{\sqrt{r^2 - R^2}}. \quad (2.3)$$

Assuming $\beta(r) = \text{const}$ we note that $\beta = 0$ for systems where the distribution of stellar orbits is isotropic, $\beta = 1$ if all stellar orbits are radial and $\beta \rightarrow -\infty$ if the orbits are circular.

Assuming the logarithmic form of the gravitational potential $\Phi(r) = V_c^2 \ln(r) + \text{const}$ and using local properties of given $I(R)$ and $\sigma(R)$ one can calculate a circular velocity V_c for three different types of stellar orbits: isotropic ($\sigma_r = \sigma_\phi = \sigma_\theta, \beta = 0$), radial ($\sigma_\phi = \sigma_\theta = 0, \beta = 1$) and circular ($\sigma_r = 0, \beta \rightarrow -\infty$). These relations are given by:

$$\begin{aligned} V_c^{\text{iso}} &= \sigma_{\text{iso}}(R) \cdot \sqrt{1 + \alpha + \gamma} \\ V_c^{\text{circ}} &= \sigma_{\text{circ}}(R) \cdot \sqrt{2 \frac{1 + \alpha + \gamma}{\alpha}} \\ V_c^{\text{rad}} &= \sigma_{\text{rad}}(R) \cdot \sqrt{(\alpha + \gamma)^2 + \delta - 1}, \end{aligned} \quad (2.4)$$

where

$$\alpha \equiv -\frac{d \ln I(R)}{d \ln R}, \quad \gamma \equiv -\frac{d \ln \sigma^2}{d \ln R}, \quad \delta \equiv \frac{d^2 \ln [I(R) \sigma^2]}{d (\ln R)^2}. \quad (2.5)$$

In case of noisy data on the dispersion velocity profile the subdominant terms γ and δ can be neglected, i.e. the dispersion profile is assumed to be flat, and equations (2.4) are simplified to:

$$\begin{aligned} V_c^{\text{iso}} &= \sigma_{\text{iso}}(R) \cdot \sqrt{\alpha + 1} \\ V_c^{\text{circ}} &= \sigma_{\text{circ}}(R) \cdot \sqrt{2 \frac{\alpha + 1}{\alpha}} \end{aligned} \quad (2.6)$$

¹Throughout this paper we denote a projected 2D radius as R and a 3D radius as r .

$$V_c^{\text{rad}} = \sigma_{\text{rad}}(R) \cdot \sqrt{\alpha^2 - 1}.$$

Let us call a sweet spot the radius at which all three curves $V_c^{\text{iso}}(R)$, $V_c^{\text{circ}}(R)$ and $V_c^{\text{rad}}(R)$ are very close to each other. One can hope that at the sweet spot the sensitivity of the method to the stellar anisotropy parameter β is minimal and the estimation of the circular speed at this particular point is reasonable. E.g. from equations (2.6) it is clear that in case of the power-law surface brightness profile with $\alpha = 2$ and $\beta = \text{const}$ the relation between the circular speed and the projected velocity dispersion does not depend on the anisotropy parameter (e.g. Gerhard, 1993). While the derivation of equations (2.4), (2.6) relies on the assumption about a flat circular velocity profile, tests on model galaxies with non-logarithmic potentials, non-power law behaviour of the surface brightness and line-of-sight velocity dispersion profiles and with the anisotropy parameter β varying with radius (Churazov et al., 2010) have shown that the circular speed can still be recovered to a reasonable accuracy. Now we extend these tests to a sample of simulated elliptical galaxies.

This method for evaluating the circular speed is not only simple and fast in implementation but it also does not require any assumptions on the radial distribution of anisotropy $\beta(r)$ and mass $M(r)$.

The mathematical derivation of equations (2.4-2.6) can be found in Churazov et al. (2010). A similar approach and analytic formulae for kinematic deprojection and mass inversion also can also be found in Wolf et al. (2010) and Mamon et al. (2010).

2.3 The sample of simulated galaxies

2.3.1 Description of the sample

Simulations provide a useful opportunity to test different methods and procedures as all intrinsic properties of a system at hand are known. The main drawback of simulated objects is that they may not include all physical processes that take place in reality and thus may not reflect all complexity of nature. To test the procedure under consideration we have used a sample of 65 cosmological zoom simulations partly presented in Oser et al. (2010). These SPH simulations include feedback from supernovae type II, a uniform UV-background radiation field, star formation and radiative Hydrogen and Helium cooling but do not include ejective feedback in the form of supernovae driven winds. Present-day stellar masses of simulated galaxies range from $2.18 \times 10^{10} M_\odot h^{-1}$ to $28.68 \times 10^{10} M_\odot h^{-1}$ inside 30 kpc. The softening length used in simulations is about $R_{\text{soft}}=400 \text{ pc } h^{-1}, h = 0.72$. Typically the softening can affect profiles up to $\sim 3R_{\text{soft}}$, which is $\simeq 1.7$ kpc in our case. We have followed a conservative approach and restricted the analysis to radii larger than 3 kpc. It should be noted that low-mass simulated galaxies may have no real counterparts possibly due to lack of important physical processes (e.g., significant winds) in simulations. However, it has been demonstrated in Oser et al. (2012) that the massive simulated galaxies have properties very similar to observed early-type galaxies (see also Figure 4), i.e. they follow

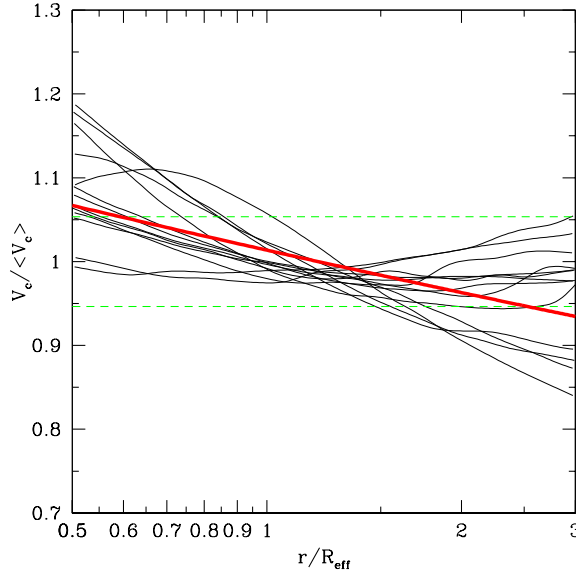


Figure 2.1: Circular velocity curves of massive galaxies ($\sigma(R_{\text{eff}}) > 200 \text{ km s}^{-1}$) as a function of radius r . Individual rotation curves normalised to the speed averaged over $[0.5R_{\text{eff}}, 3R_{\text{eff}}]$ are shown in black, green dashed lines indicate the interval $[1 - RMS, 1 + RMS]$, where $RMS = 4.9\%$, the red thick line represents the overall trend $V_c \propto r^{-0.06}$.

the observed scaling relations and their evolution with redshift. For detailed description of simulations and included physics see Oser et al. (2010).

To effectively increase the number of galaxies we have considered three independent projections of each galaxy. So the whole sample of simulated galaxies consists of 195 objects².

2.3.2 Isothermality of potentials in massive galaxies

First of all we have found that massive galaxies in the sample have almost isothermal rotation curves over broad range of radii. To demonstrate this statement (Figure 2.1) we have selected galaxies with a projected velocity dispersion at the effective radius $\sigma(R_{\text{eff}})$ (procedure of computation R_{eff} is described in section 2.3.3) greater than 200 km s^{-1} and plotted their circular velocity curves $V_c = \sqrt{GM(< r)}/r$ as a function of r/R_{eff} . G is the gravitational constant, $M(< r)$ is the mass enclosed within r and R_{eff} is the effective radius of the galaxy. The circular velocity curves were normalised to the value of V_c averaged over $r \in [0.5R_{\text{eff}}, 3R_{\text{eff}}]$. Three circular velocity curves that make the most significant contribution to the RMS actually correspond to galaxies with the effective radius $R_{\text{eff}} < 6 \text{ kpc}$. The fact that for these galaxies $0.5R_{\text{eff}}$ is close to the softening length may affect the

²Nevertheless, for calculating an error in a bias estimation ($= RMS / \sqrt{N}$) we conservatively use the number of galaxies rather than the number of projections as the subsamples corresponding to different projections are not entirely independent.

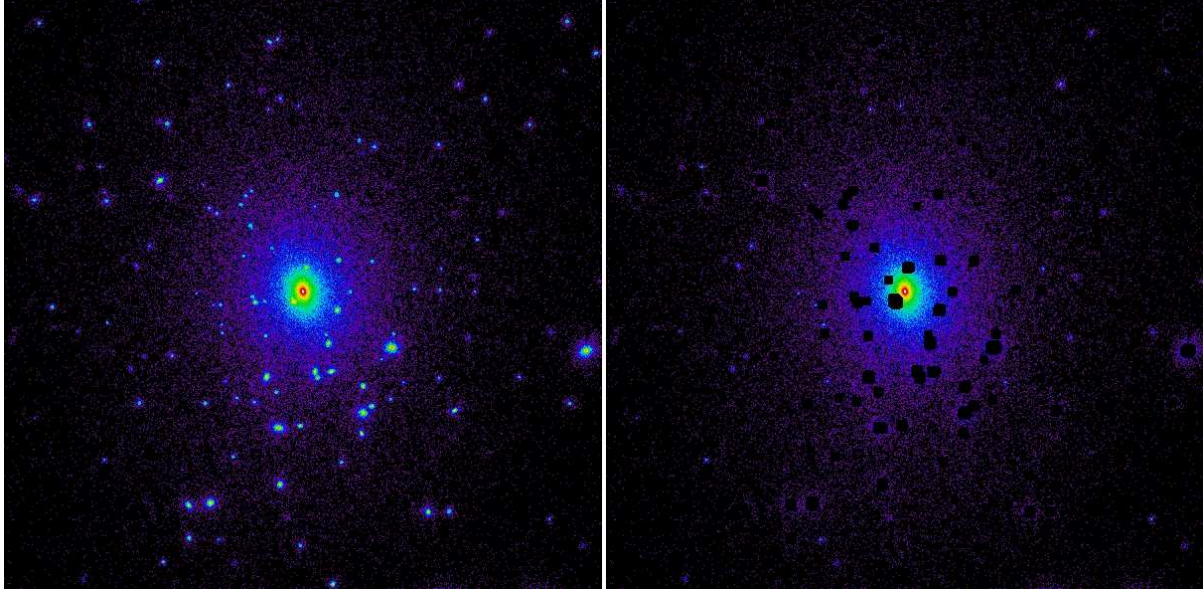


Figure 2.2: Excluding the satellites. $150 \text{ kpc} \times 150 \text{ kpc}$. Left: Initial galaxy image. Right: Cleaned galaxy image.

scatter.

2.3.3 Analysis procedure

The analysis of each galaxy consists of several steps described below.

Step 1: Excluding satellites from the galaxy image.

Usually an image of a simulated galaxy (the distribution of stars projected onto a plane) contains many satellite objects and needs to be cleaned. Exclusion of satellites makes the surface brightness and the line-of-sight velocity dispersion profiles smoother and reduces the Poisson noise associated with satellites. The algorithm we used for removing satellites is as follows: first, for each star a quantity w characterising the local density of stars ($w \propto \rho_*^{-1/3}$) and analogous to the HSML (the SPH smoothing length) was calculated and the array of these values was sorted. Then the $(0.4 \cdot N_{\text{stars}})^{\text{th}}$ term of the sorted w -array was chosen as a reference value w_o . N_{stars} is a total number of stars in a galaxy and a factor in front of N_{stars} is some arbitrary parameter (the value 0.4 was chosen by a trial-and-error method). Stars with the 3D-radius $r > 10 \text{ kpc}$ and $w < w_o$ are considered as members of a satellite. After projecting stars onto the plane perpendicular to the line of sight we have excluded all satellites together with an adjacent area of 1.5 kpc in size. The initial and final images of some arbitrarily chosen galaxy (the virial halo mass is $\simeq 1.7 \times 10^{13} M_\odot h^{-1}$) are shown in Figure 2.2.

Step 2: Evaluating $I(R)$ and $\sigma(R)$.

All radial profiles have been computed in a set of logarithmic concentric annuli around

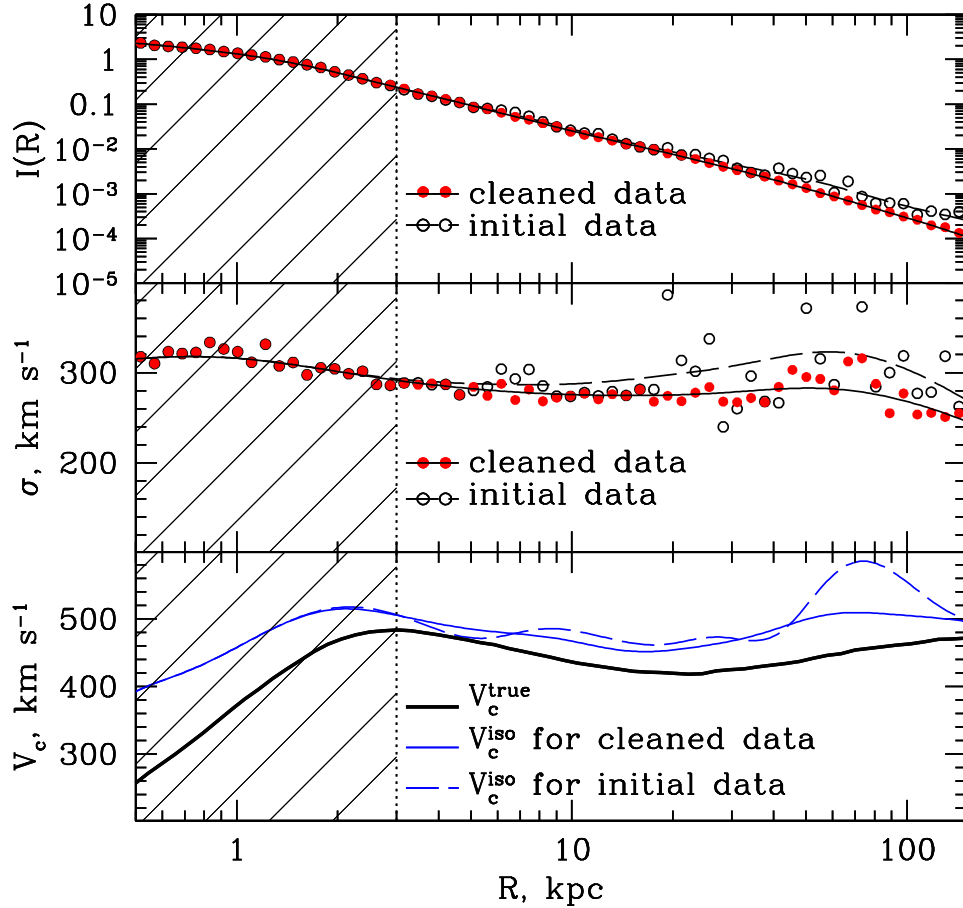


Figure 2.3: Influence of satellites on the surface brightness (the upper panel) and the projected velocity dispersion profiles (in the middle). Open black circles correspond to the initial galaxy image and solid red circles - to the galaxy image without satellites. The black dashed curve is the smoothed curve for the initial data and the black solid curve is for the cleaned data. The bottom panel shows the true circular velocity (black thick line) and recovered circular velocity for the isotropic distribution of stellar orbits (in blue) for initial data (dashed) and cleaned data (solid). It is clear that removing satellites reduces the scatter in the line-of-sight velocity dispersion data and makes the profile smoother.

the halo center. To calculate the surface brightness profile, corrected for the contamination from the satellites, we have first counted the number of stars in each annulus, excising the regions around satellites. The surface area of each annuli has been also calculated, excluding the same regions. The ratio of these quantities gives us the desired ‘cleaned’ surface brightness profile. The average line-of-sight velocity of stars and the projected velocity dispersion have been calculated similarly.

Importance of the ‘cleaning’ procedure and the resulting profiles of $I(R)$ and $\sigma(R)$ are shown in Figure 2.3. The surface brightness data (open circles correspond to the initial (‘uncleaned’) image and red solid circles to the ‘cleaned’ image) and the smoothed curves (the calculation of these curves is described in Step 3) are shown in the upper panel, the projected velocity dispersion profiles are shown in the middle panel. The true circular velocity $V_c^{\text{true}}(r)$ (black solid curve) and recovered from the initial data (blue dashed line) and from ‘cleaned’ data (blue solid line) circular velocity for the isotropic distribution of stellar orbits V_c^{iso} (the first equation in (2.4)) are shown in the bottom panel. The last curve is in better agreement with the true velocity profile. All results and figures in this paper are restricted to the region $R > 3.0$ kpc.

Step 3: Taking derivatives.

To take derivatives we follow the procedure described in Churazov et al. (2010) in Appendix B. The main idea is that all data points participate in calculating the derivative but with different weights. The weight function is given by

$$W(R_0, R) = \exp \left[-\frac{(\ln R_0 - \ln R)^2}{2\Delta^2} \right], \quad (2.7)$$

where R_0 is the radius at which the derivative is being calculated and the parameter Δ is the width of the weight function.

Both observed and simulated surface brightness profiles are typically quite smooth so we have used $\Delta_I = 0.3$ to calculate the logarithmic derivative $d \ln I(R) / d \ln R$. For the line-of-sight velocity dispersion data we have used $\Delta_\sigma = 0.5$. With the assumed values of Δ the local perturbations are smoothed out but the global trend of the profiles is not affected. Changing values Δ_I and Δ_σ in the range [0.3, 0.5] does not significantly influence our final result³. The difference (in terms of circular velocity) is less than 1%. As an example the smoothed curves for the $I(R)$ and $\sigma(R)$ data in Figure 2.3 are calculated using this procedure.

We have also tested the influence of parameters of the presented smoothing algorithm. As long as the smoothed curve describes data reasonably well neither the functional form of the weight function nor other parameters (like higher order terms in expansion $\ln I(R) = a(\ln R)^2 + b \ln R + c$ or $\sigma(R) = a(\ln R)^2 + b \ln R + c$) significantly affect the final result.

Step 4: Estimating the circular velocity.

Applying equations (2.4) or (2.6) to the smoothed $I(R)$ and $\sigma(R)$ we have calculated V_c -profiles assuming isotropic, radial and circular orbits of stars. Then we have found a

³If, however, we choose a width of the weight function smaller than $\Delta = 0.3$ the local scatter in the data is not smoothed out and the results become ambiguous.

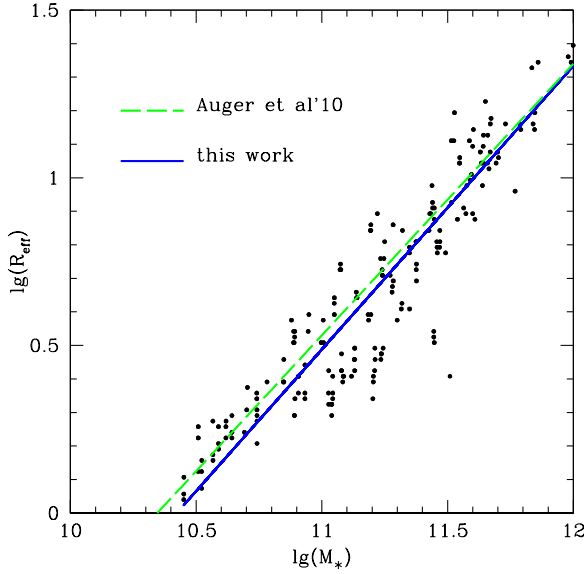


Figure 2.4: $R_{\text{eff}} - M_*$ relation. The blue solid line is the linear fit to data points from the simulations. The green dashed line is the observed mass-size relation from (Auger et al., 2010).

radius (a sweet point R_{sweet}) at which the quantity $(V_c^{\text{iso}} - \bar{V})^2 + (V_c^{\text{rad}} - \bar{V})^2 + (V_c^{\text{circ}} - \bar{V})^2$, where $\bar{V} = (V_c^{\text{iso}} + V_c^{\text{rad}} + V_c^{\text{circ}})/3$, is minimal. The value of the isotropic velocity profile at this particular point is the estimation of the circular velocity speed we are looking for. We take V_c^{iso} as an estimate of the $V_c(R)$ (rather than V_c^{circ} or V_c^{rad}) for two reasons. Firstly, at around one effective radius the dominant anisotropy for most elliptical galaxies is $\sigma_{zz} < \sigma_{RR} \sim \sigma_{\phi\phi}$ (Cappellari et al. (2007)). The spherically averaged anisotropy is therefore only moderate (see also Gerhard et al. (2001), Figure 4). Massive elliptical galaxies are the most isotropic. Thus an isotropic orbit distribution is a much better approximation than purely radial or circular orbits. Secondly, the value of V_c^{iso} is less prone to spurious wiggles in $I(R)$ and $\sigma(R)$.

The effective radius R_{eff} is calculated as a radius of the circle which contains half of the projected stellar mass, taking into account effects of cleaning. We found that in the simulated data-set the value of the effective radius depends on the maximal radius used to calculate the total number of stars in a galaxy. The problem is especially severe for the most massive galaxies as they have an almost power-law 3D stellar density distribution $\rho_* \propto r^{-a}$ with $a \simeq 3$. In our analysis (in contrast to Oser et al. (2012)) we have not introduced any artificial cut-off and used all stars in the smooth stellar component (excluding substructure) of the main galaxies out to their virial radii for the calculation of the effective radius. The resulting effective radii as a function of total stellar mass (in logarithmic scale) are shown in Figure (2.4). The slope and the normalization of the $R_{\text{eff}} - M_*$ relation are close to the fit of SLACS data by Auger et al. (2010).

The axis ratio q of each projection of a galaxy is calculated as a square root of eigenval-

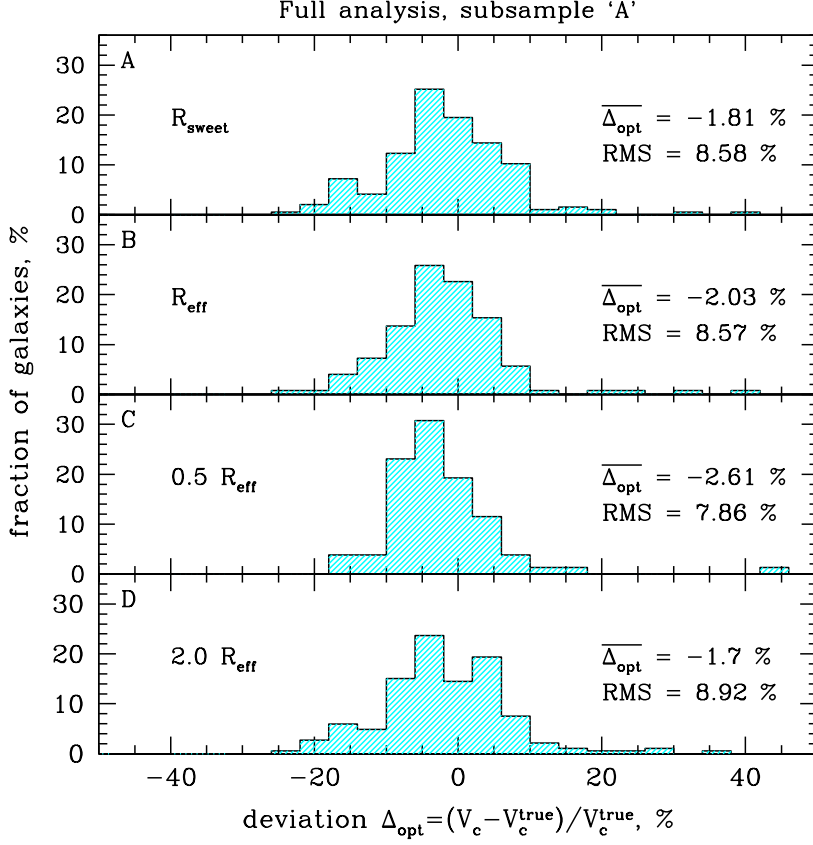


Figure 2.5: The fraction of galaxies (in %) as a function of deviation $\Delta_{opt} = (V_c^{\text{iso}} - V_c^{\text{true}}) / V_c^{\text{true}}$ evaluated via equations (2.4) at different radii: R_{sweet} (panel (A)), R_{eff} (panel (B)), $0.5R_{\text{eff}}$ (panel (C)) and $2R_{\text{eff}}$ (panel (D)).

ues of the diagonalised inertia tensor. The inertia tensor is computed within the effective radius without excluding substructures. We have found that q is not sensitive to our cleaning procedure as normally there are almost no satellites within R_{eff} .

2.4 Analysis of the sample

2.4.1 At a sweet point

For each galaxy in the sample we have performed all steps described above and we have selected the radius at which the circular velocity curves for isotropic, circular and radial orbits (equations (2.4)) intersect or lie close to each other. Then we have calculated the value of the isotropic speed V_c^{iso} at this radius. To measure the accuracy of our estimates let us introduce a deviation from the true circular speed $\Delta_{opt} = (V_c^{\text{iso}} - V_c^{\text{true}}) / V_c^{\text{true}}$, where V_c^{iso} and V_c^{true} should be taken at the sweet spot R_{sweet} . The subscript 'opt' (= optical) is used

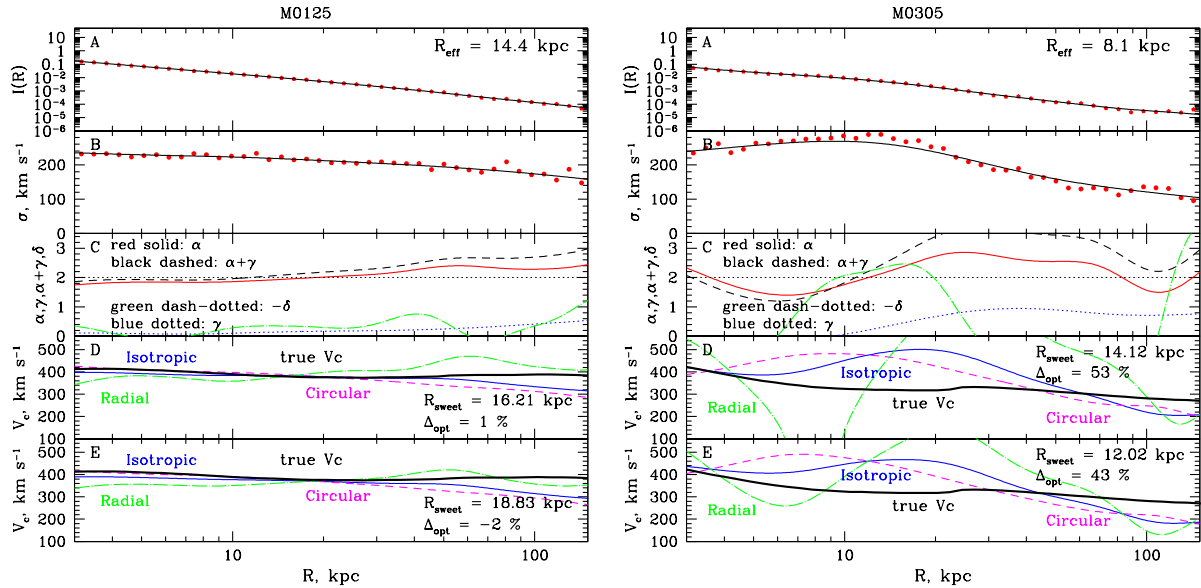


Figure 2.6: Left: Example of the galaxy that perfectly suits for the analysis. The surface brightness and the projected velocity dispersion profiles are shown in panels (A) and (B) correspondingly. Data are represented as red points and smoothed curves that were used to compute derivatives (α, γ, δ) as black solid lines. The auxiliary coefficients $\alpha, \gamma, -\delta$ and $\alpha + \gamma$ are shown in panel (C) in red solid, blue dotted, green dash-dotted and black dashed lines, respectively. Circular velocity profiles for isotropic orbits of stars (blue solid line), pure radial (green dash-dotted) and pure circular (magenta dashed) orbits as well as the true circular speed (black thick curve) are presented in panel (D) for the full version of the analysis (equations (2.4)). And the same curves for the simplified analysis (equations (2.6)) are shown in panel (E). Right: Example of the galaxy with large deviation Δ_{opt} due to merger activity. The crest in the projected velocity dispersion profile at $R \simeq 20$ kpc leads to the significantly overestimated value of the circular speed.

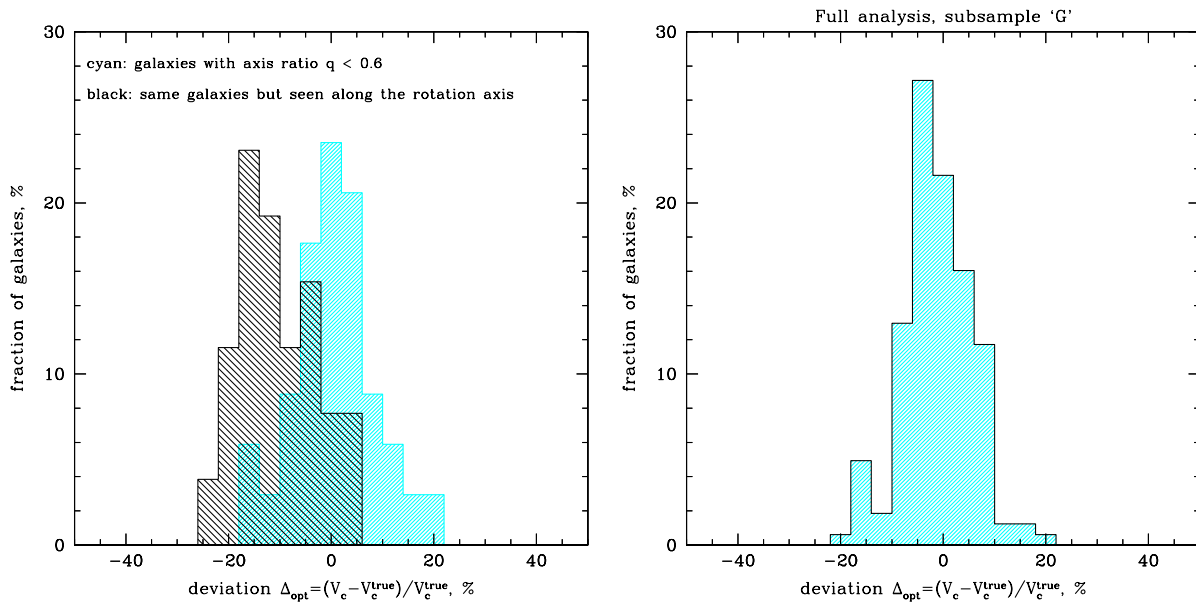


Figure 2.7: Left: Shown in cyan is the histogram for deviations for galaxies with the axis ratio $q < 0.6$, in black is the histogram for the same galaxies but seen in a projection with the axis ratio q close to unity (= seen along the rotation axis). Right: The histogram for deviations for the sample when merging and oblate galaxies seen along the rotation axis are excluded (subsample ‘G’). The average deviation $\overline{\Delta_{opt}} = (-1.2 \pm 0.9)\%$, $RMS = 6.8\%$.

to distinguish this method (based on optical data) from circular speed calculations based on X-ray data. We have plotted the number of galaxies (normalised to the total number of galaxies and expressed in %) versus the deviation Δ_{opt} in a form of a histogram. To have an idea whether the method under consideration gives reasonable accuracy, histograms for deviations at R_{eff} , $0.5R_{\text{eff}}$ and $2R_{\text{eff}}$ are also shown. The whole sample ('subsample A') is presented in Figure 3.6. The sample averaged value of the deviation $\overline{\Delta_{opt}}$ is slightly less than zero in all cases. For example, at the sweet point $\overline{\Delta_{opt}} = (-1.8 \pm 1.1)\%$ while the RMS = 8.6%⁴.

Large deviations ($\sim 30 - 40\%$) are seen only in galaxies with ongoing merger activity. The influence of mergers appears as 'waves' in the projected velocity dispersion profile. The example of such a system is shown in Figure 2.6 (right panel). The presence of such 'waves' indicates that the circular speed could be significantly overestimated (by a factor of $\sim 1.2 - 1.5$), which is not surprising as the method is based on the spherical Jeans equations and the assumption about dynamical equilibrium is violated. When the profiles $I(R)$ and $\sigma(R)$ are smooth and monotonic the circular speed can be recovered with much higher accuracy (Figure 2.6, left panel).

The sample includes galaxies with different values of ellipticity. The axis ratio q (computed from the diagonalized inertia tensor within R_{eff}) ranges from 0.19 to 0.99. To test the possible influence of the ellipticity on the accuracy of estimates we have selected galaxies with axis ratio $q < 0.6$. The resulting distribution as a function of the circular speed deviations is almost symmetric, unbiased, with $RMS \simeq 8\%$ (Figure 2.7). On the other hand, if we consider the same galaxies seen in a projection with the maximum value of the axis ratio q , we get the distribution appreciably biased toward negative values of the deviation ($\overline{\Delta_{opt}} = (-10.2 \pm 1.6)\%$). The reason for this bias is rotation. When observing a galaxy along its rotation axis the projected velocity dispersion is appreciably smaller than for perpendicular directions. To further test this statement we have rotated each galaxy so that the principal axes of the galaxy ($A \geq B \geq C$) coincide with the coordinate system (x , y and z , correspondingly) and analysed velocity maps for each projection. As a criteria for rotation we have used the anisotropy-parameter $(v/\sigma)^* = \frac{v/\bar{\sigma}}{\sqrt{(1-q)/q}}$, where v is the average rotation velocity of stars, $\bar{\sigma}$ is the mean velocity dispersion and q is the axis ratio (Binney, 1978; Bender and Nieto, 1990). If $(v/\sigma)^* > 1.0$ then the object is assumed to be rotating. We have found that the most massive simulated galaxies usually do not rotate or rotate slowly and show signs of triaxiality while less massive galaxies rotate faster and show signs of axisymmetry. This statement is in agreement with observational studies (e.g. Cappellari et al. (2007) and references therein). Moreover, the majority of rotating galaxies appears to be oblate, rotating around the short axis. So for the oblate galaxies observed along the rotation axis (and as a consequence seen in a projection with the axis ratio q close to unity) the method gives underestimated values of the circular speed. It should be noted that when observing the rotating galaxies along long axes the circular speed esti-

⁴ $\bar{x} = \frac{\sum x}{N}$, $RMS = \sqrt{\frac{\sum (x - \bar{x})^2}{N-1}}$

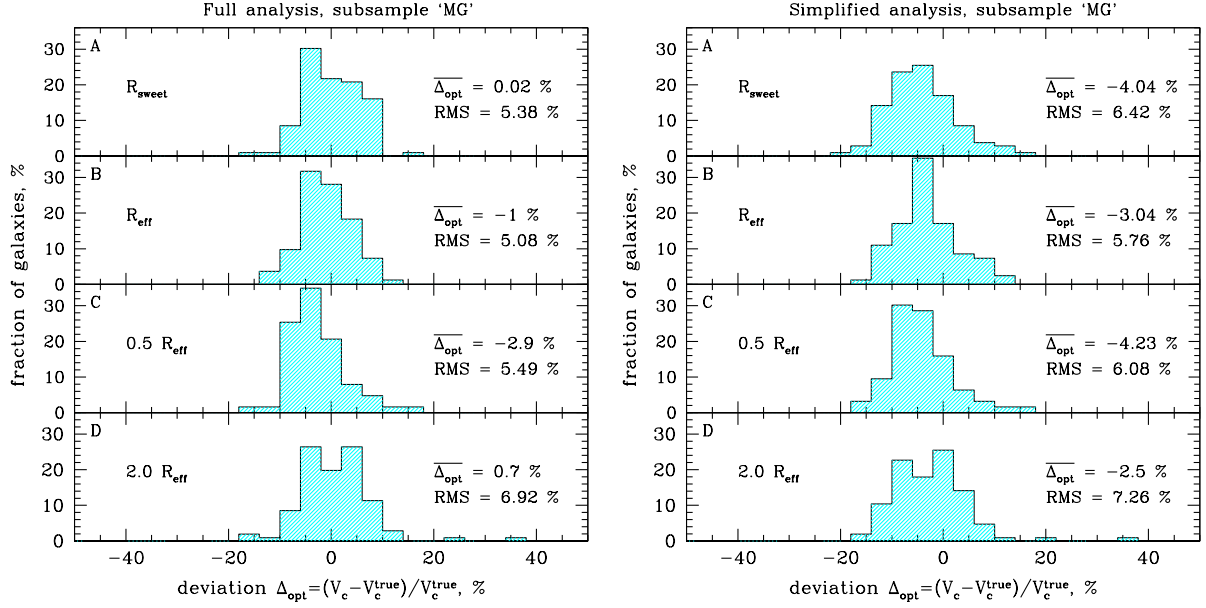


Figure 2.8: Left: Distribution of galaxies from the subsample ‘MG’ (massive galaxies with $\sigma(R_{\text{eff}}) > 150 \text{ km s}^{-1}$ when merging and oblate galaxies observed along the rotation axis are excluded) according to their deviations. Deviations are calculated at R_{sweet} (panel (A)), R_{eff} (panel (B)), $0.5R_{\text{eff}}$ (panel (C)) and $2R_{\text{eff}}$ (panel (D)). Right: The same histograms but for the simplified version of the analysis (equations (2.6))

mate is slightly biased towards overestimation (Thomas et al. (2007) reached the similar conclusion). The average deviation for the subsample of oblate galaxies seen perpendicular to the rotation axis is biased high by $\Delta_{\text{opt}} \simeq (4.4 \pm 1.4)\%$ with RMS = 6.3%.

To investigate possible projection effects on the results of our analysis we have picked one rotating galaxy (the virial halo mass is $\simeq 2.2 \times 10^{12} M_{\odot} h^{-1}$) and calculated the surface brightness and the velocity dispersion profiles for different lines of sight. While the light profiles are quite similar, the velocity dispersion profiles may differ significantly when the line of sight is parallel to the rotation axis and perpendicular to it. We have calculated the average value of the circular speed estimates taking into account the probability of observing the galaxy at different angles. For the selected galaxy the average deviation from the true V_c is about -4.9% and the maximum deviation (when observing along the rotation axis) is about -25% .

It should be mentioned that the method under consideration was designed for recovering the circular speed in massive elliptical galaxies and it does not pretend to give accurate results for low-mass galaxies. In addition, not so many elliptical galaxies with $\sigma < 150 - 200 \text{ km s}^{-1}$ are observed (e.g. Bernardi et al., 2010).

It is convenient to distinguish low and high mass simulated galaxies by the value of the projected velocity dispersion at the effective radii. Let us call ‘massive’ galaxies with $\sigma(R_{\text{eff}}) > 150 \text{ km s}^{-1}$. If we apply our analysis to the subsample of massive galaxies and exclude merging and oblate galaxies seen along the rotation axis (the subsample ‘MG’),

we get an unbiased distribution with $RMS = 5.4\%$. The resulting histogram is shown in Figure 2.8, left image, panel (A). Estimations at other radii give slightly more biased and slightly less accurate results (Figure 2.8, left image, panels (B)-(D)).

Thereby we have marked out four subsamples - the whole sample without exceptions ('A' - all), the sample without merging or oblate galaxies seen along the rotation axis ('G' - good), the subsample of massive galaxies ('M' - massive) with $\sigma(R_{\text{eff}}) > 150 \text{ km s}^{-1}$ and, finally, the subsample of massive galaxies when merging and oblate galaxies observed along the rotation axis are excluded ('MG' - massive and good).

In case of missing or unreliable data on the line-of-sight velocity dispersion profile Churazov et al. (2010) suggest to apply a simplified version of the aforementioned analysis (equations (2.6)). By neglecting terms γ and δ we assume that the projected velocity dispersion profile is flat. Then the radius at which $I(R) \propto R^{-2}$ is the sweet point. The resulting histograms for the subsample 'MG' are shown in Figure 2.8, right panel. It can be seen that data on the projected velocity dispersion plays noticeable role in the analysis if the required accuracy is of order of several %. Neglecting its derivatives leads to a bias towards underestimated values of V_c ($\overline{\Delta}_{opt} = (-4.0 \pm 1.1)\%$ at the sweet point) and broader wings/tails ($RMS = 6.4\%$ at R_{sweet}) compared to Figure 2.8, left panel. Nonetheless, if only the surface brightness profile and some data on the projected velocity dispersion are available the simplified version of the method seems to be a good choice.

2.4.2 Simulated galaxies at high redshifts

We have also tested the same procedure for galaxies at higher redshifts. Namely, at $z = 1$ and $z = 2$. The fraction of merging galaxies in the sample is larger at high redshift than at $z = 0$ and the number of stars in each halo is considerably smaller. Nevertheless, results are quite encouraging. For the subsample 'MG' the average deviation of the circular speed for the isotropic distribution of orbits at the sweet point (estimated via equations (2.4)) from the true one is close to zero and the scatter is modest. At redshift $z = 1$ the average deviation is $\overline{\Delta}_{opt} = (-0.3 \pm 1.1)\%$ and $RMS = 6.0\%$, at $z = 2$ $\overline{\Delta}_{opt} = (0.9 \pm 2.2)\%$ and $RMS = 8.0\%$.

2.4.3 Mass from integrated properties

Asssuming the logarithmic form of the gravitational potential $\Phi(r) = V_c^2 \ln r + const$ we can estimate the potential Φ over some range of radii up to a constant. To calculate the potential one needs to know the circular velocity profile. If we assume that this profile roughly coincides with the isotropic profile V_c^{iso} over some range of radii (let us choose $R \in [0.5R_{\text{eff}}, 3R_{\text{eff}}]$ as a range of radii easily available for observations), we can define:

$$\Phi^{opt} = \int_{0.5R_{\text{eff}}}^R \frac{[V_c^{\text{iso}}]^2}{r} dr, \quad (2.8)$$

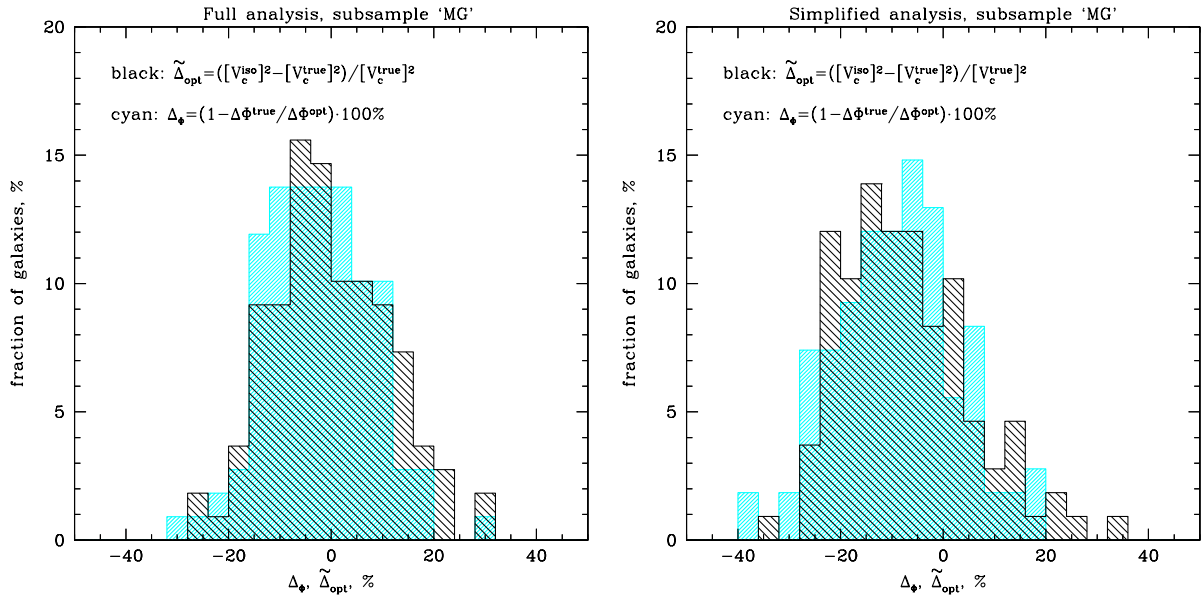


Figure 2.9: Accuracy of the derived potential of massive galaxies (merging and oblate objects seen along the rotation axis are excluded). In cyan shown the histogram for the quantity $\Delta_\Phi = (1 - \kappa) \cdot 100\%$, where $\kappa = \Delta\Phi^{true}/\Delta\Phi^{opt}$. In black shown the histogram for the deviation $\tilde{\Delta}_{opt}$ of the estimated at the sweet point $[V_c^{\text{iso}}]^2$ from the true one $[V_c^{\text{true}}]^2$. Left: Histograms for the full version of the analysis (equations (2.4)). The average value of κ is $\bar{\kappa} = 1.02 \pm 0.02$ and $RMS = 10.3\%$. The average value of the deviation $\tilde{\Delta}_{opt}$ is $(-0.2 \pm 1.9)\%$ and $RMS = 11.3\%$. Right: Histograms for the simplified version of the analysis (equations (2.6)). $\bar{\kappa} = 1.09 \pm 0.02$ and $RMS = 11.8\%$, $\bar{\tilde{\Delta}}_{opt} = (-7.2 \pm 2.1)\%$ and $RMS = 12.7\%$.

where $R \in (0.5R_{\text{eff}}, 3R_{\text{eff}})$ and V_c^{iso} can be found from the full version of the analysis (the first equation of (2.4)) or from the simplified version (the first equation of (2.6)). As the true potential is known we can write $\Phi^{\text{true}} = \kappa \cdot \Phi^{\text{opt}} + \text{const}$. In the ideal case $\kappa = \Delta\Phi^{\text{true}}/\Delta\Phi^{\text{opt}} = 1.0$. The accuracy of such an approach is illustrated in Figure 2.9. In cyan is shown the distribution of subsample ‘MG’ of galaxies as a function of $\Delta_\Phi = (1-\kappa) \cdot 100\%$. Just to remind this subsample consists of the massive galaxies with $\sigma(R_{\text{eff}}) > 150 \text{ km s}^{-1}$ and merging galaxies as well as oblate galaxies seen along their rotation axes are excluded. In case of the full analysis the distribution is almost unbiased (the average value of κ is 1.02 ± 0.02) with $RMS = 10.9\%$. For the simplified formula of V_c^{iso} we see some offset $\overline{kappa} = 1.09 \pm 0.02$ and $RMS = 11.8\%$. In approximation of small deviations RMS defined for the potential calculations is twice as large as RMS for the circular velocity calculations because the potential Φ scales as V_c^2 . To compare this approach with previous results let us introduce the deviation $\tilde{\Delta}_{\text{opt}} = ([V_c^{\text{iso}}]^2 - [V_c^{\text{true}}]^2)/[V_c^{\text{true}}]^2$ estimated at the sweet point R_{sweet} . Resulting distribution for the same subsample is shown in black in Figure 2.9. As expected the width of this distribution is nearly two times larger than the distribution of circular velocity estimates (Figure 2.8).

As we see the gravitational potential can be estimated via V_c^{iso} with reasonable accuracy. This fact is in agreement with the aforementioned statement that most massive galaxies in the sample have almost flat circular velocity profiles in broad range of radii.

2.4.4 Circular speed derived from the projected dispersion in a fixed aperture

When data on the velocity dispersion are available only in the form of aperture dispersions one can estimate the circular speed using the simple relation

$$V_c^2 = 3 \cdot \sigma_{ap}^2 (< R), \quad (2.9)$$

where $\sigma_{ap}(< R)$ is the velocity dispersion measured within some aperture R . To test this way of evaluating the circular speed we have computed the luminosity-weighted dispersion within the aperture of radius R (excluding the region $R < 2R_{\text{soft}} = 3 \text{ kpc}$ where softening may affect results of the analysis)

$$\sigma_{ap}^2 (< R) = \frac{\int_R^{2R_{\text{soft}}} I(x) \sigma^2(x) x dx}{\int_R^{2R_{\text{soft}}} I(x) x dx} \quad (2.10)$$

and calculated the deviation from the true circular speed at different radii: at the sweet point R_{sweet} for the full version of the analysis (equations (2.4)), at $R = 0.5R_{\text{eff}}$, R_{eff} and $2R_{\text{eff}}$. The resulting histograms for the subsample ‘MG’ are presented in Figure 2.10. Comparing with circular speed estimations at a single radius (in particular, at the sweet point) this method gives a biased result $\overline{\Delta}_{\text{opt}}(R_{\text{eff}}) = (1.0 \pm 1.3)\%$ and noticeably larger RMS (at R_{eff} RMS = 7.8%).

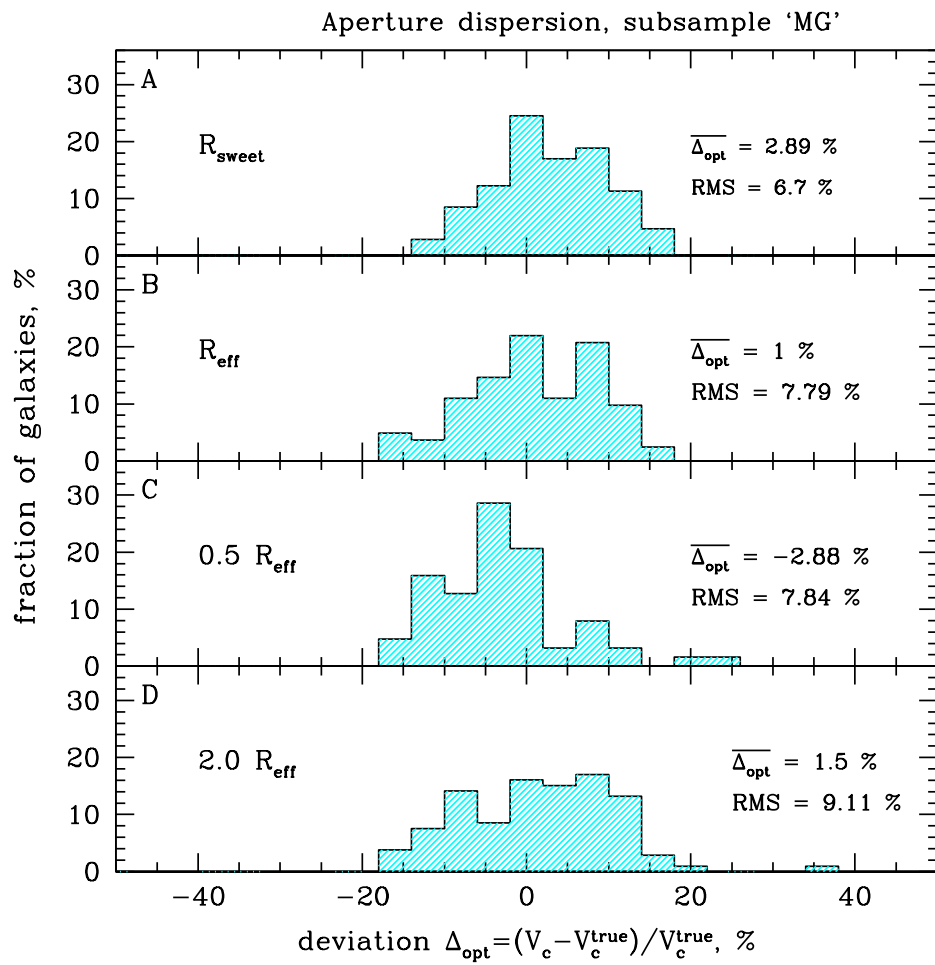


Figure 2.10: Distribution of galaxies from the subsample ‘MG’ (galaxies with $\sigma(R_{\text{eff}}) > 150$ km s⁻¹ when merging and oblate galaxies seen along the rotation axis are excluded).

2.4.5 Circular speed from X-ray data

Another way to measure the mass of galaxies comes from the analysis of the hot X-ray gas in galaxies. By measuring the gas number density n and the temperature T profiles from X-ray observations one can find the total mass assuming that the gas is in the hydrostatic equilibrium (HE) (e.g. Mathews, 1978; Forman, Jones and Tucker, 1985). Assuming spherical symmetry, the equation of HE can be written

$$-\frac{1}{\rho} \frac{dP}{dr} = \frac{d\Phi}{dr} = \frac{V_c^2}{r} = \frac{GM}{r^2}, \quad (2.11)$$

where $P = nkT$ is the gas pressure (n is the gas number density), $\rho = \mu m_p n$ is the gas density (m_p is the proton mass), Φ is the gravitational potential, V_c is a circular velocity and M is the total mass of the galaxy. In simulations the mean atomic weight μ is assumed to be equal to 0.58. Strictly speaking, assuming the HE one neglects possible non-thermal contribution to the pressure, which can be due to presence of (i) turbulence in the thermal gas, (ii) cosmic rays and magnetic fields (e.g. Churazov et al., 2008).

To estimate deviations from HE, the so called mass bias, we took a subsample of the most massive galaxies with $M > 6.5 \cdot 10^{12} M_\odot$. X-ray properties of low mass galaxies in the sample are influenced by gravitational softening in the central 3-4 kpc and are strongly dominated by cold and dense clumps in center. Moreover, we know from observations that only the most massive galaxies have massive X-ray atmospheres (e.g. O'Sullivan et al., 2001).

The typical profiles of the gas density and temperature extracted from simulations are shown in Figure 2.11. We used the median value of the electron density n_e and T determined in each spherical shell, so that we are free of cold dense clumps contamination (Zhuravleva et al., 2012). Calculated pressure and circular velocity (equation 2.11) are also shown in Figure 2.11. The spurious feature of simulations is that in the central 3-4 kpc cold and dense clumps are strongly dominating. Even using the median value does not remove these clumps, causing strong increase of density and drop of temperature in the center. These clumps are moving ballistically and are not in the HE.

Deviations from HE $\Delta_X = \frac{V_c - V_c^{\text{true}}}{V_c^{\text{true}}}$ were calculated at R_{eff} (cyan histogram in Figure 2.12) and $2R_{\text{eff}}$ (black histogram in Figure 2.12). The average over the subsample value of the deviation at R_{eff} is $\overline{\Delta_X} = (-3.0 \pm 1.3)\%$ and RMS=4.4%. At $2R_{\text{eff}}$ $\overline{\Delta_X} = (-4.0 \pm 1.1)\%$, RMS = 3.8 %. The average value of $\frac{V_{\text{true}}^2 - V_x^2}{V_{\text{true}}^2}$ over $R_{\text{eff}} < R < 2R_{\text{eff}}$ is 6.8 %.

To calculate averaged ratio of kinetic energy and thermal energy $\frac{E_{\text{kin}}}{E_{\text{therm}}}$ on $R_{\text{eff}} < R < 2R_{\text{eff}}$ one should exclude cold dense clumps since their contribution to the kinetic energy can be significant. The procedure to exclude clumps is described in Zhuravleva et al. (2012). In brief, in each radial shell, we exclude particles with density exceeding the median value by more than 2 standard deviations. An example of initial and diffuse projected densities is shown in Figure 2.13. Calculated mean ratio of $\frac{E_{\text{kin}}}{E_{\text{therm}}}$ for diffuse component is 4.4 %,

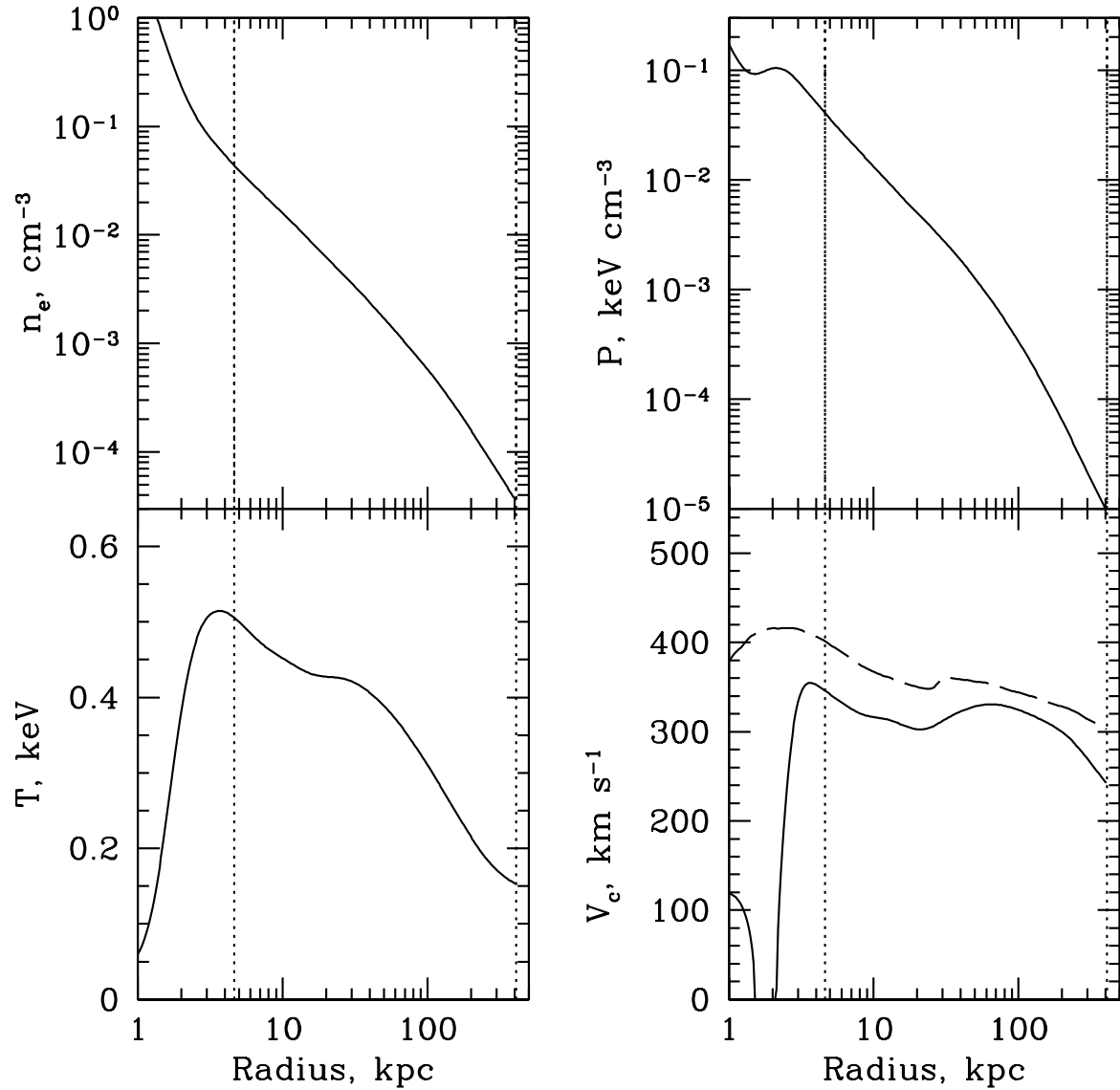


Figure 2.11: Profiles of hot gas electron number density, temperature, pressure and circular velocity of simulated galaxy. Dotted vertical curves show the upper and lower limits on R . V_c plot: solid and dashed curves show mass from HE and total mass from simulations respectively.

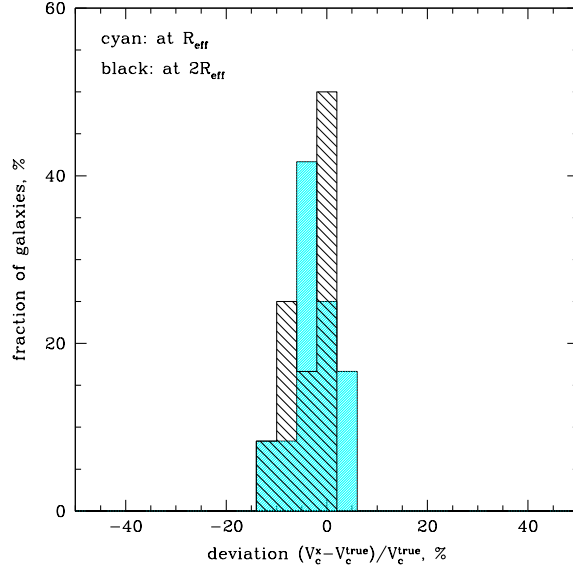


Figure 2.12: Distribution of galaxies according to their deviations of estimated circular speed from the true value at R_{eff} (shown in cyan) and at $2R_{\text{eff}}$ (shown in black). Circular speed is derived using the hydrostatic equilibrium equation for the hot gas. The sample consists of 12 galaxies.

which is close to the bias in mass from HE.

2.5 Testing the method on simulated galaxy clusters

The simple method for mass determination of elliptical galaxies from optical data is not restricted to analysis of stellar profiles. Planetary nebulae and globular clusters can also be used as tracers. Moreover, it can be applied to galaxy clusters for which we can use a spatial distribution and velocity dispersion of individual galaxies to get a reliable mass (or circular speed) estimate. To test the method we have applied it to a sample of simulated galaxy clusters from Dolag et al. (2009). Extracted light profile (number of galaxies per unit area) and line-of-sight velocity dispersion profile have much more scatter than those for the elliptical galaxies due to smaller number of tracers. So it is reasonable to use the simplified version of the analysis (equations (2.6)).

Figure 2.14 illustrates an example of applying the method to a simulated galaxy cluster. The projected number density $I(R)$ and the line-of-sight velocity dispersion profiles are shown in Figure 2.14, panel A and panel B, respectively. Using equations (2.6) we have computed V_c^{iso} , V_c^{rad} and V_c^{circ} and found a point R_{sweet} of their intersection at which we estimate the circular speed and calculated the deviation Δ_{opt} .

Figure 2.15 shows the histograms of the deviation Δ_{opt} for two cases: when number of galaxies (subhalos) is large, e.g. $N_{\text{subhalos}} > 100$ (Figure 2.15 , upper panel), and when the

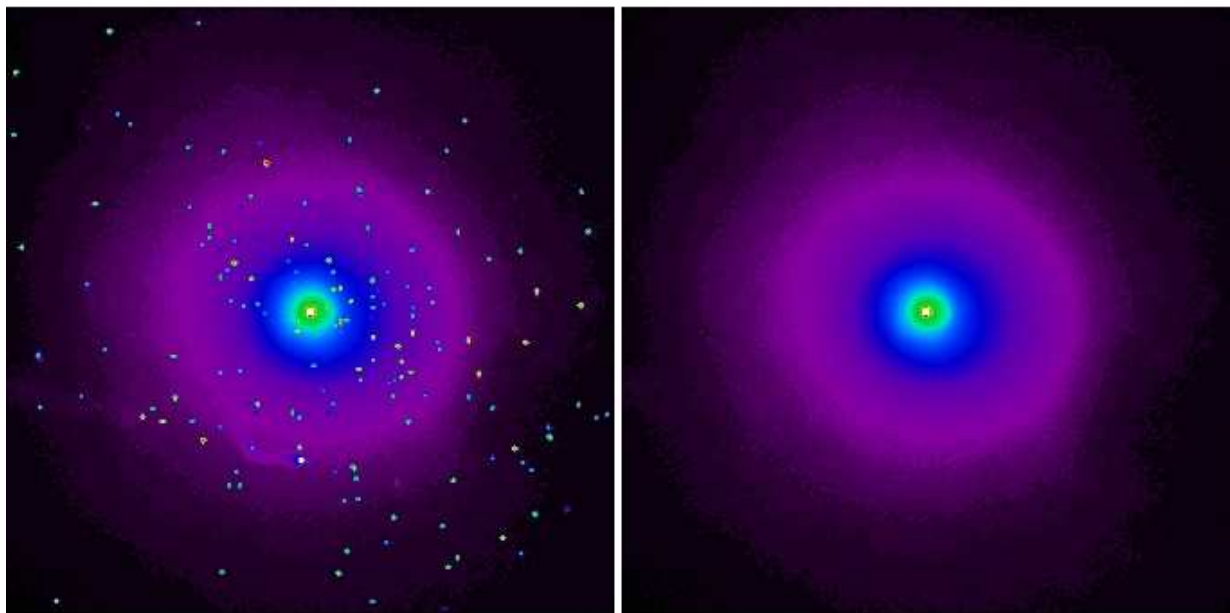


Figure 2.13: Projected number density of hot gas in simulated galaxy. Left: initial density, right: density with excluded clumps.

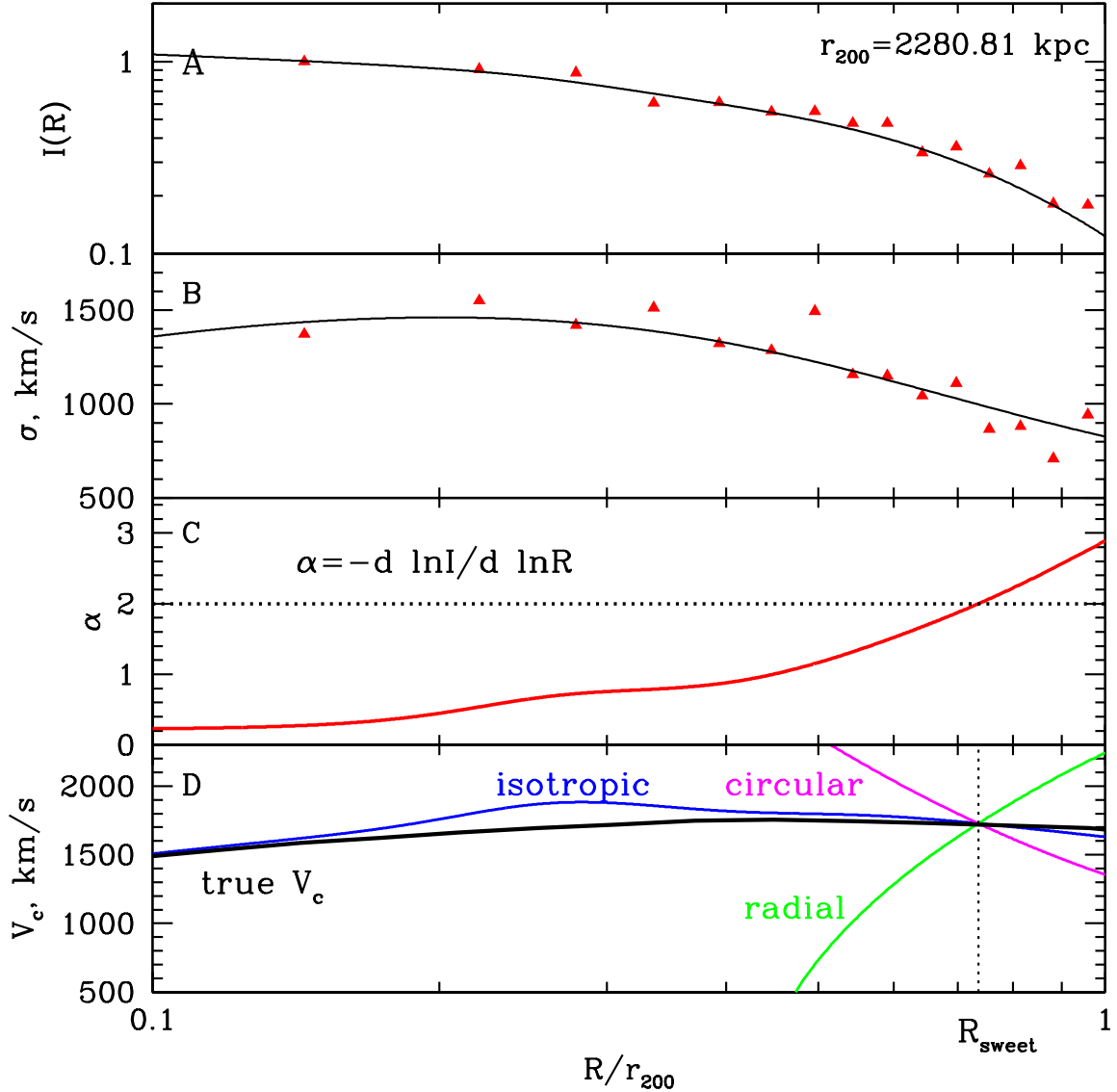


Figure 2.14: Circular speed estimation in the simulated galaxy cluster. The projected number density of galaxies and the line-of-sight velocity dispersion profiles are shown in panels (A) and (B), respectively (data are shown as red triangles, interpolated curves - as black solid lines). The slope of the surface brightness α is shown in panel (C) as a red solid line. Circular speed profiles for isotropic orbits of galaxies (blue solid line), pure radial (green dash-dotted) and pure circular (magenta dashed) orbits as well as the true circular speed (black thick curve) are shown in panel (D) for the simplified version of the analysis (equations (2.6)).

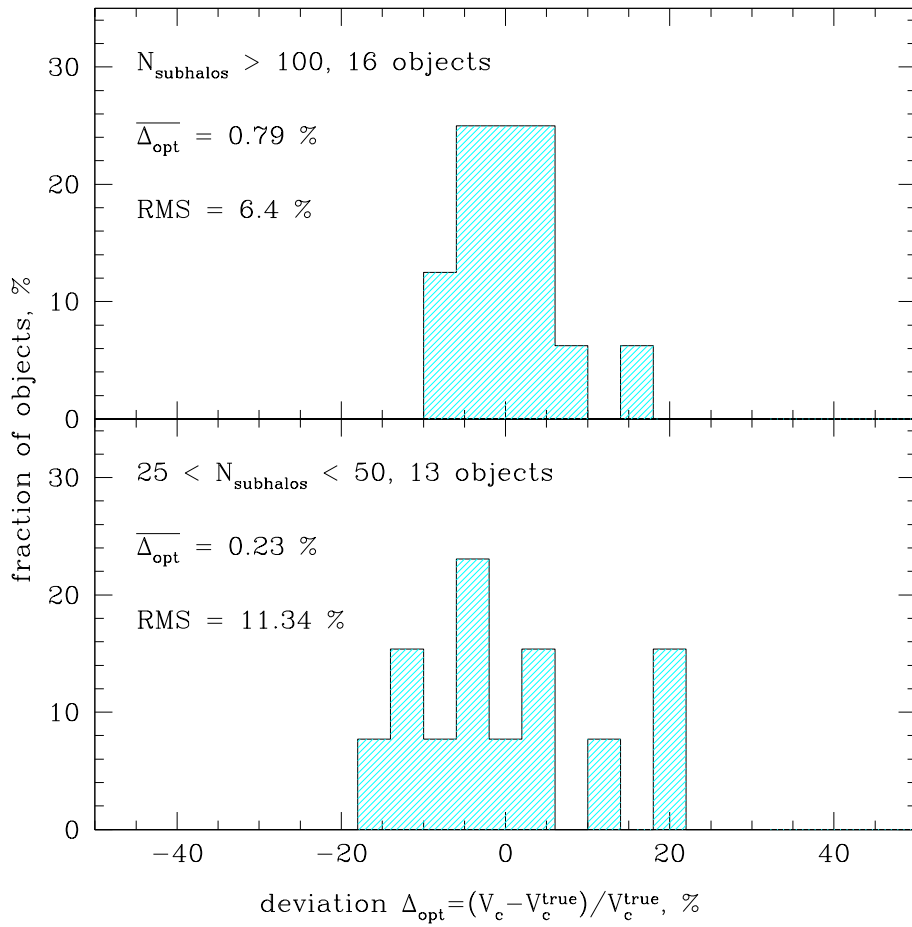


Figure 2.15: The fraction of galaxy clusters as a function of the deviation Δ_{opt} for two cases: rich (panel A) and small clusters (panel B).

Table 2.1: Summary of the methods discussed.

	A		G		M		MG	
	$\overline{\Delta}$, %	RMS, %	$\overline{\Delta}$, %	RMS, %	$\overline{\Delta}$, %	RMS, %	$\overline{\Delta}$, %	RMS, %
full analysis, R_{sweet}	-1.8	8.6	-1.2	6.8	0.2	7.7	0.0	5.4
full analysis, R_{eff}	-2.0	8.6	-2.4	5.9	-0.6	8.5	-1.0	5.1
simplified analysis, R_{sweet}	-5.9	9.6	-5.8	7.4	-3.3	9.2	-4.0	6.4
simplified analysis, R_{eff}	-4.3	8.9	-4.6	6.6	-2.7	8.7	-3.0	5.8
$\Phi^{\text{true}} = \kappa \cdot \Phi^{\text{opt}} + \text{const}$, eq.(2.4)	3.7	8.7	2.9	7.1	1.2	6.7	1.2	5.1
$\Phi^{\text{true}} = \kappa \cdot \Phi^{\text{opt}} + \text{const}$, eq.(2.6)	7.5	10.1	6.7	8.2	4.4	7.8	4.5	5.9
aperture dispersions, R_{eff}	-1.4	10.3	-1.5	9.2	1.1	9.2	1.0	7.8
	R_{eff}		$2R_{\text{eff}}$					
X-ray	$\overline{\Delta}, \%$ -3.0	RMS, % 4.4	$\overline{\Delta}, \%$ -4.0	RMS, % 3.8				

number of galaxies does not exceed 50 (Figure 2.15 , lower panel).

When averaged over a sample the deviation is close to zero which allows one to use the method for mass determination of even small clusters with $\sim 30 - 50$ data points available and for cross-calibration of other mass determination methods (X-ray analysis, weak lensing, etc).

2.6 Discussion

In Table 3.3 we summarize the bias and accuracy of all methods discussed above. The sample of simulated galaxies was divided into 4 subsamples: the whole sample without exceptions ('A'), the subsample 'G'('good') for which merging and oblate galaxies observed along the rotation axis are excluded, the subsample 'M' of massive galaxies with $\sigma(R_{\text{eff}}) > 150 \text{ km s}^{-1}$, and the subsample 'MG' of massive galaxies when merging and oblate galaxies seen along the rotation axis are excluded. For estimations of the potential the bias and the RMS are nearly twice large as those for the circular speed estimations. To avoid possible confusion all values in the table are associated with V_c - estimations.

In case of the subsample 'MG' the estimation of the circular speed at the sweet point with help of equations (2.4) gives the unbiased result ($\overline{\Delta}_{\text{opt}} \simeq 0\%$) and reasonable accuracy (RMS $\simeq 5 - 6\%$). To test whether the unbiased average is not just a coincidence we have performed a 'Jack knife' test. The resulting average for randomly chosen subsamples is less than 1%. The subsample 'MG' consists of 106 objects and the statistical uncertainty in this case is about 0.9%.

For the subsample 'M' of massive galaxies (127 objects, 26 of them (13.3%) are oblate, 3 of them (2.4%) are with ongoing merger activity) we also got almost the unbiased average ($\overline{\Delta}_{\text{opt}} = (0.2 \pm 1.2)\%$). From an observational point of view merging objects can be easily excluded while information on the 'oblateness' of galaxies may not be available. If we

exclude merging galaxies from the subsample ‘M’ we get the average value of the deviation $\overline{\Delta_{opt}} = -0.7\%$, RMS = 5.9%. So the result is almost unbiased. But if run the ‘Jack knife’ tests we get on average slightly underestimated values of the circular speed with $|\overline{\Delta_{opt}}|$ less than 1.5 %.

The method is not restricted to nearby galaxies, it also allows to recover the circular speed for high-redshift ellipticals. The circular speed estimate averaged over the subsample of massive and slowly or non-rotating simulated objects (mergers are excluded) at $z = 1$ is $\overline{\Delta_{opt}} = (-0.3 \pm 1.1)\%$ with RMS = 6.0 %, at $z = 2$ the average deviation is $\overline{\Delta_{opt}} = (0.9 \pm 2.2)\%$ and RMS = 8.0 %. So the V_c -estimates are also almost unbiased with modest scatter of 6 – 8% as in case of subsample ‘MG’ at $z = 0$.

While derivation of equations (2.4) and (2.6) is based on the assumption of the logarithmic form of the gravitational potential we have shown that the circular speed estimate at the sweet point is still reasonable even if true circular velocity is not flat.

The case of slowly changing V_c with radius can be illustrated by the following example. If we assume that V_c varies with radius as a power law along with other quantities $I(R) \propto R^{-\alpha}$, $\sigma_p^2 \propto R^{-\gamma}$, $\beta = \text{const}$ we end up with the following relation between V_c and σ_p (from Jeans equation):

$$V_c^2(R) = \sigma_p^2(R) \cdot \frac{1 + \alpha + \gamma - 2\beta}{(1 - \beta \cdot \frac{\alpha + \gamma}{1 + \alpha + \gamma})} \cdot \frac{\Gamma[\frac{\alpha}{2}] \cdot \Gamma[\frac{1+\alpha+\gamma}{2}]}{\Gamma[\frac{1+\alpha}{2}] \cdot \Gamma[\frac{\alpha+\gamma}{2}]}, \quad (2.12)$$

where $\Gamma[x]$ is the gamma function. This relation is insensitive to the anisotropy parameter β when $\alpha + \gamma = 2$. One can hope therefore that for slopes slowly varying with radius the sweet point will be located at the radius where this condition is met. Substituting $\alpha + \gamma = 2$ in equation (2.12) yields the relation between V_c and σ_p which coincides with equation (2.5) for isotropic orbits for $\alpha = 2$. Deviations of α from 2 by 10% cause modest $\sim 3\%$ variations in V_c .

Simulated galaxies are of course more complicated than the above example. For our sample we have investigated possible correlations between the deviation Δ_{opt} of the estimated V_c from the true one and local (at R_{sweet}) slopes of the velocity $d \ln V_c^{\text{true}} / d \ln r$, surface brightness $\alpha = -d \ln I(R) / d \ln R$ and velocity dispersion $\gamma = -d \ln \sigma^2 / d \ln R$ profiles. There is no obvious correlation between Δ_{opt} and α or γ . We do see a weak linear trend in Δ_{opt} and $d \ln V_c^{\text{true}} / d \ln r$, although it is much smaller than the scatter in Δ_{opt} . Most of the galaxies in the sample $V_c(R)$ slowly declines with radius near R_{sweet} (see Figure 2.1). However, even after subtracting this trend, the RMS-scatter in Δ_{opt} is reduced from 5.4% to 5.0%, i.e. only by 0.4%.

Comparable results are obtained using $\int [V_c^{\text{iso}}]^2 / r dr$ over $[0.5R_{\text{eff}}, 3R_{\text{eff}}]$ as an estimator of the gravitational potential.

The simplified version of the analysis (equations (2.6)) at the sweet point gives almost the same result as at the effective radius. So if one has no enough data to calculate all necessary for applying equations (2.4) derivatives it makes sense to derive V_c^{iso} from the first formula of (2.6) and use $V_c^{\text{iso}}(R_{\text{eff}})$ as an estimation of the circular speed. The quality of such approach depends on the ‘quality’ of the sample. In case of non-interacting and almost

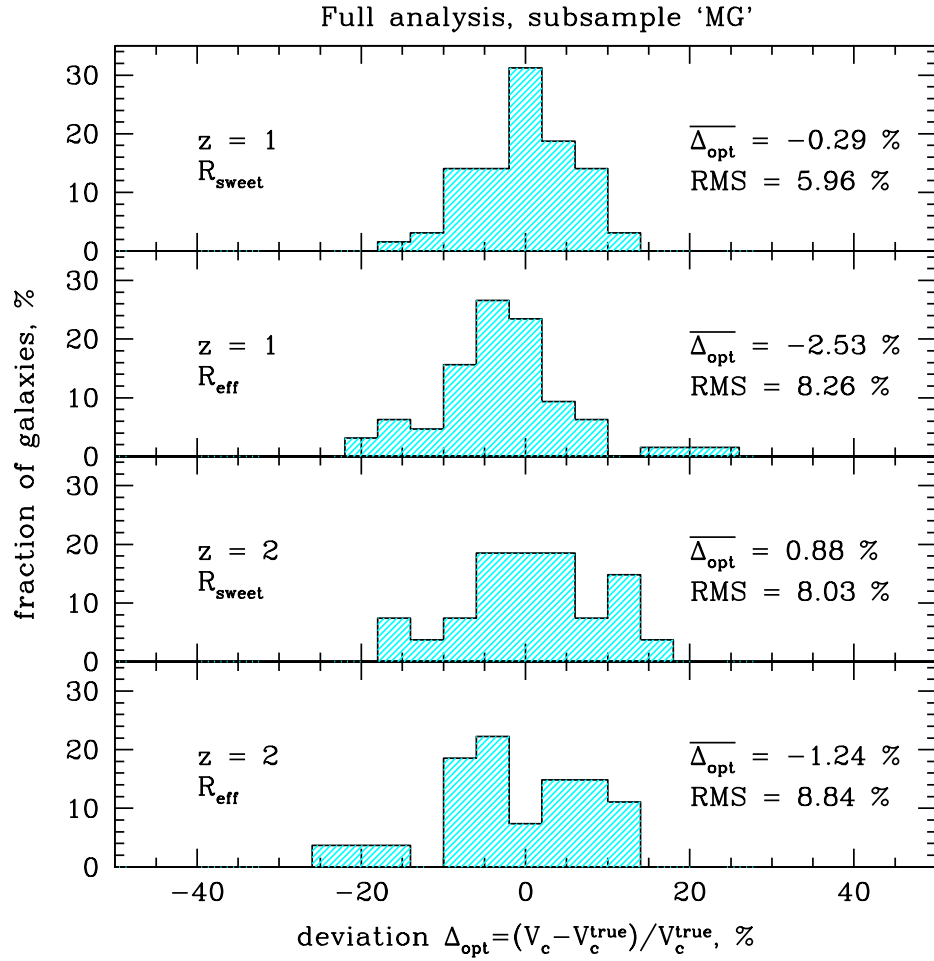


Figure 2.16: Distribution of high-redshift galaxies from the subsample ‘MG’ (massive galaxies with $\sigma(R_{\text{eff}}) > 150 \text{ km s}^{-1}$ when merging and oblate galaxies observed along the rotation axis are excluded) according to their circular speed deviations. Deviations are calculated at R_{sweet} (panels (A), (C)) and at R_{eff} (panels (B), (D)).

spherical galaxies the RMS is about 7% and the bias is about $(-4 \pm 1.1)\%$. Assuming flat projected velocity dispersion profile leads to the underestimation of the circular speed. If data on the line-of-sight velocity dispersion allow to estimate the overall trend $\Delta\sigma/\Delta R$ it may reduce the bias.

In general we can expect the sweet point to be not far from the radius R_2 where $-d\ln I(R)/d\ln R \simeq 2$. Indeed for a smooth surface brightness profile which gradually steepens with radius an integral $\int I(R)RdR$ diverges at low or high limits for $-d\ln I(R)/d\ln R$ greater or lower than 2 respectively. Therefore one can hope that at the radius R_2 the contributions to the integral of $R < R_2$ and $R > R_2$ to be comparable and $R_2 \sim R_{\text{eff}}$. Thus, $R_{\text{sweet}} \sim R_{\text{eff}}$. E.g. for a Sérsic model with index n (Graham and Driver (2005))

$$-\frac{d\ln I(R)}{d\ln R} \simeq 2 \left(\frac{R}{R_{\text{eff}}} \right)^{1/n}$$

and it can be easily seen that the sweet point for the circular speed estimation is of order of the effective radius. Moreover, as it was shown in Churazov et al. (2010) (Table 4) for Sérsic models the stellar anisotropy is close to minimal at about $0.5R_{\text{eff}}$ and this radius can be used as the sweet point for the circular speed determination.

We have tested the statement that $R_{\text{sweet}} \sim R_2 \sim R_{\text{eff}}$ on the sample of the simulated objects. If the slope of the surface brightness profile is close to -2 over some range of radii or $\alpha = -d\ln I(R)/d\ln R$ is not monotonic then there is an ambiguity in selecting R_{sweet} and R_2 . To avoid this ambiguity we have smoothed $I(R)$ and $\sigma(R)$ using the width of the window function $\Delta_I = \Delta_\sigma = 1.0$. As a result $\alpha(R)$ has become monotonic for majority of objects and newly determined \tilde{R}_{sweet} , \tilde{R}_2 follow the relationship $\tilde{R}_{\text{sweet}} \sim \tilde{R}_2 \sim R_{\text{eff}}$. However, a significant smoothing of data leads to a bias in estimating the circular speed $\overline{\Delta_{opt}} \simeq -2\%$ at both \tilde{R}_{sweet} and \tilde{R}_2 .

2.7 Conclusions

Being an important issue, the total mass estimation for elliptical galaxies is often quite difficult, especially for galaxies at high redshift. We used a large sample of cosmological zoom simulations of individual galaxies to test a simple and robust procedure (see equations (2.4), (2.6)) based on the surface brightness and velocity dispersion profiles to estimate the circular speed and therefore the total mass of a massive galaxy. The method is very simple and it does not require any assumptions on the stellar anisotropy profile. For massive ellipticals without significant rotation at redshifts $z = 0 - 2$ it gives an unbiased estimate of the circular speed (the bias $\Delta_{opt}(R_{\text{sweet}})$ is less than 1%) with 5-6% scatter. Therefore this method is suitable for the analyze of large samples of galaxies with limited observational data at low and high redshifts. The method works best for the most massive ellipticals ($\sigma(R_{\text{eff}}) > 200 \text{ km s}^{-1}$), which in the present simulations have almost isothermal circular velocity profiles over broad range of radii.

The method should be applied with caution to merging galaxies where the circular speed can be significantly overestimated. For rotating galaxies seen along the rotation axis

the procedure gives substantially underestimated V_c .

The best estimate of the circular speed is obtained at a sweet point R_{sweet} where the sensitivity of the recovered circular speed to the stellar anisotropy is expected to be minimal (see section 2.2). The R_{sweet} is expected to be not far from the projected radius where the surface brightness declines approximately as $I \propto R^{-2}$. This radius is in turn close (within factor of 2) to the effective radius R_{eff} of the galaxy. Our tests have shown that the accuracy (RMS scatter) of the circular speed estimates at $0.5 - 2 R_{\text{eff}}$ is $5 - 7\%$ for most massive ellipticals.

An even simpler method - based on the aperture velocity dispersion (equations (2.9), (2.10)) - is found to be less accurate, although the results are still reasonable. For example, for massive galaxies without significant rotation the sample averaged deviation of the circular speed at the effective radius is $\Delta_{\text{opt}}(R_{\text{eff}}) = (1.0 \pm 1.3)\%$ with RMS $\simeq 8\%$. Other flavors of the circular speed estimates are described in Section 2.4.4.

Using the same simulated set we have also tested the accuracy of the circular speed estimate from the hydrostatic equilibrium equation for the hot gas in massive ellipticals. We found a negative bias at the level of $3 - 4\%$ and the scatter of $\simeq 5\%$. The presence of bias is caused by the residual gas motions.

The method is not restricted to elliptical galaxies. It can also be applied to galaxy clusters. For galaxy clusters it is reasonable to use the simplified version of the analysis (equation (2.6)) as the number of tracers (and, as a consequence, the number of data points) is much smaller than in the case of galaxies. The recovered circular speed estimate remains almost unbiased for poor as well as rich galaxy clusters with a reasonable scatter, e.g. RMS = 11.3% for objects containing 25-30 tracer particles and rms reduces to 6.4% when more than 100 tracers available.

Given its simplicity, small bias and modest scatter the method can be applied for quick mass estimations for large samples of elliptical galaxies and galaxy clusters especially when the comprehensive study of each individual object is not justified.

2.8 Acknowledgments

We are grateful to the referee for very useful comments and suggestions. NL is grateful to the International Max Planck Research School on Astrophysics (IMPRS) for financial support. TN acknowledges support from the DFG Excellence Cluster "Origin and Structure of the Universe". The work was supported in part by the Division of Physical Sciences of the RAS (the program "Extended objects in the Universe", OFN-16).

Bibliography

- Auger M.W., Treu T., Bolton A.S., Gavazzi R., Koopmans L.V.E., Marshall P.J., Moustakas L.A., Burles S. 2010, ApJ, 724, 511
- Bernardi M., Shankar F., Hyde, J.B., Mei S., Marulli F., Sheth R.K. 2010, MNRAS, 404, 2087
- Bender R., Nieto J.-L. 1990, A&A, 239, 97
- Binney J. 1978, MNRAS, 183, 501
- Cappellar M., Bacon R., Bureau M., Damen M. C., Davies R. L., de Zeeuw P. T., Emsellem E., Falcón-Barroso J., Krajnović D., Kuntschner H., McDermid R. M., Peletier R. F., Sarzi M., van den Bosch R. C. E., van de Ven G. 2006, MNRAS, 366, 1126
- Cappellari M., Emsellem E., Bacon R., Bureau M., Davies R.L., de Zeeuw P.T., Falcón-Barroso J., Krajnović D., Kuntschner Harald, McDermid R.M., Peletier R.F., Sarzi M., van den Bosch R.C.E., van de Ven G. 2007, MNRAS, 379, 418
- Churazov E., Forman W., Vikhlinin A., Tremaine S., Gerhard O., Jones C. 2008, MNRAS, 388, 1062
- Churazov E., Tremaine S., Forman W., Gerhard O., Das P., Vikhlinin A., Jones C., Böhringer H., Gebhardt K. 2010, MNRAS, 404, 1165
- Dolag K., Borgani S., Murante G., Springel V. 2009, MNRAS, 399, 497
- Forman W., Jones C., Tucker W., 1985, ApJ, 293, 102
- Gavazzi R., Treu T., Rhodes J.D., Koopmans L.V.E., Bolton A.S., Burles S., Massey R.J., Moustakas L.A. 2007 ApJ, 667, 176
- Gerhard O.E. 1993, MNRAS, 265, 213
- Gerhard O., Jeske G., Saglia R.P., Bender R. 1998, MNRAS, 295, 197
- Gerhard O., Kronawitter A., Saglia R. P., Bender R. 2001, MNRAS, 121, 1936

- Graham A.W., Driver S.P. 2005, Publications of the Astronomical Society of Australia, 22, 118
- Humphrey P., Buote D., Gastaldello F., Zappacosta L., Bullock J., Brighenti F., Mathews W. 2006, ApJ, 646, 899
- Mamon G.A. and Boué G. 2010, MNRAS, 401, 2433
- Mandelbaum R., Seljak U., Kauffmann G., Hirata C.M., Brinkmann J. 2006, MNRAS, 368, 715
- Mathews W. G., 1978, ApJ, 219, 413
- Oser L., Ostriker J.P., Naab T., Johansson P.H., Burkert A. 2010, ApJ, 725, 2312
- Oser L., Naab T., Ostriker J.P., Johansson P.H., 2011, ApJ, 744, 630
- O'Sullivan E., Forbes D. A., Ponman T. J. 2001, MNRAS, 328, 461
- Thomas J., Jesseit R., Naab T., Saglia R.P., Burkert A., Bender R. 2007, MNRAS, 381, 1672
- Thomas J., Saglia R.P., Bender R., Thomas D., Gebhardt K., Magorrian J., Corsini E.M., Wegner G., Seitz S. 2011, MNRAS, 415, 545
- Wolf J., Martinez G.D., Bullock J.S., Kaplinghat M., Geha M., Muñoz R.R., Simon J.D., Avedo F.F. 2010, MNRAS, 406, 1220
- Zhuravleva I., Churazov E., Kravtsov A., Sunyaev R. 2012, MNRAS, 422, 2712

Chapter 3

Stellar kinematics of X-ray bright massive elliptical galaxies

Mon.Not.R.Astron.Soc., submitted

N.Lyskova, E.Churazov, A.Moiseev, O.Silchenko, I.Zhuravleva

Abstract.

We discuss a simple and fast method for estimating masses of early-type galaxies from optical data and compare the results with X-ray derived masses. The optical method relies only on the most basic observables such as the surface brightness $I(R)$ and the line-of-sight velocity dispersion $\sigma_p(R)$ profiles and provides an anisotropy-independent estimate of the circular speed V_c of the galaxy. The mass-orbit degeneracy is effectively overcome by evaluating V_c at a characteristic radius R_{sweet} defined from *local* properties of observed profiles without making apriori assumptions on the global radial distribution of mass, tracers and/or orbital anisotropy. The sweet radius R_{sweet} is expected to lie close to R_2 where the surface brightness declines as R^{-2} . For monotonically steepening profiles R_{sweet} and R_2 should be not far from the effective radius R_{eff} . We apply the method to a sample of five X-ray bright elliptical galaxies observed with the 6-m telescope of the Special Astrophysical Observatory of the Russian Academy of Sciences (SAO RAS). We then compare the optical V_c -estimate with the X-ray derived value obtained from Chandra data under the assumption of the hydrostatic equilibrium, and discuss possible constraints on the non-thermal pressure in the hot gas and configuration of stellar orbits. We find that when averaged over the sample the ratio of the optical V_c -estimate to the X-ray one is equal to ≈ 0.98 with 11% scatter, i.e. there is no evidence for the large non-thermal pressure contribution in the gas at $\sim R_{\text{sweet}}$. From analysis of the Lick indices H β , Mgb, Fe5270 and Fe5335, we derive the ages, chemical abundance, stellar mass-to-light ratios, what allows us to calculate the mass of the stellar component within the sweet radius. We conclude that a typical fraction of dark matter inside R_{sweet} in the sample galaxies is $\sim 50\%$ for the Salpeter IMF and $\sim 70\%$ for the Kroupa IMF.

3.1 Introduction

Being the most massive galaxies in the local Universe, giant elliptical galaxies provide a natural laboratory to study galaxy formation, assembly and evolution processes. The current paradigm of galaxy formation is the hierarchical scenario which suggests that early-type galaxies have complex merging histories of assembling most of the mass through accretion of small galaxies with rare major merger events (e.g. de Lucia and Blaizot, 2007; Naab et al., 2007). Accurate mass determinations and disentangling a luminous and dark matter components at different redshifts are the key steps towards a consistent theory for elliptical galaxies formation.

Determining the mass profile of early-type galaxies is a notoriously difficult problem as there are no dynamical tracers with the known intrinsic shape and structure of orbits, so that circular velocity curves of elliptical galaxies cannot be measured directly. A number of methods are in use for constraining the mass of early-type galaxies and the shape of dark matter halos, each having its own set of assumptions and limitations. Comparison of the mass profiles obtained from different independent techniques is necessary to get reliable estimates. It also helps to control the systematic uncertainties, inherent in all methods, as well as leads to interesting constraints on properties of elliptical galaxies.

One of the mass estimation techniques comes from X-ray observations of extended hot X-ray-emitting coronae of massive elliptical galaxies. It is a powerful tool to probe the mass distribution over several decades in radius: from $\sim 0.1R_{\text{eff}}$ out to $\sim 10R_{\text{eff}}$. In this approach spherical symmetry of a galaxy and hydrostatic equilibrium of the gas are commonly assumed. While the spherical symmetry approximation introduces only a small bias, if any (e.g. Piffaretti et al., 2003; Buote and Humphrey, 2012c), validity of the hydrostatic equilibrium assumption is the subject of debate. When one is able to quantify deviations from hydrostatic equilibrium, it allows to estimate (although indirectly) pressure of the non-thermal gas motions. Most simulations suggest that in relaxed systems hydrostatic approximation works well, with non-thermal support at the level of 5% to 35% of the total gas pressure (e.g. Nagai, Vikhlinin and Kravtsov, 2007). When X-ray observations are combined with, for instance, optical data on the stellar kinematics, then comparison between the X-ray gravitating mass profile and the optical mass allows one to estimate the magnitude of the non-thermal motions of the hot gas, to constrain the mass-to-light ratio, to disentangle stellar and dark matter contributions to the total gravitating mass profile and to characterize the distribution of stellar orbits.

Although elliptical galaxies suffer from a lack of ‘ideal’ traces like disc rotation curves in spiral galaxies and there is an inherent degeneracy between anisotropy and mass, studies of stellar kinematics and dynamics provide the tools for measuring the gravitating mass profile with sufficient accuracy (up to $\sim 15\%$, Thomas 2010). Methods based on the Schwarzschild modeling of stellar orbits in axisymmetric (or even triaxial) potentials are considered to be the state-of-the-art techniques in this field. The most sophisticated approaches operate with full information on the line-of-sight velocity distribution including higher-order moments. The orbit-based methods allow to infer not only the total mass profile, but also to measure the dark matter content, derive mass-to-light ratios and get

the distribution function of stellar orbits. Among the drawbacks of these methods are the high computational cost and the necessity to have high-quality observational data. So only nearby elliptical galaxies can be studied by means of Schwarzschild modelling, and for a large sample of objects, especially with noisy photometric and/or kinematical data, such an approach is not justified.

In this paper we discuss a simple approach for estimating the mass from the stellar kinematics (Churazov et al., 2010; Lyskova et al., 2012) that relies only on the most basic observables such as the surface brightness and line-of-sight velocity dispersion profiles. By design the method is simple and fast and has a modest scatter ($\Delta V_c/V_c \sim 5 - 10\%$, Lyskova et al. 2012). This makes it suitable for large samples of elliptical galaxies even with limited and/or noisy observational data. Of course, the method is not intended to replace a thorough investigation of each individual galaxy.

We apply the method to a small and rather arbitrarily selected sample of massive elliptical galaxies located at the centers of groups and clusters, and bright in X-rays. The surface brightness and projected velocity dispersion profiles up to several effective radii have been measured with optical long-slit spectroscopic facilities on the 6-m telescope of the Special Astrophysical Observatory of the Russian Academy of Sciences (SAO RAS). Using publicly available Chandra data we also derive the X-ray mass profile and compare it with simple optical estimates.

The paper is organized as follows. In Section 3.2, we provide a brief description of the method. We apply it to real elliptical galaxies in Section 3.3, starting with the illustration of the method on the example of the extensively studied giant elliptical galaxy M87 in Section 3.3.1. Details on the observations of the sample of early-type galaxies are presented in Section 3.3.2. We derive circular speed estimates from optical and X-ray analyses and estimate stellar contributions in Sections 3.3.3-3.3.6. Results are summarized in Section 3.4, and Section 3.5 contains conclusions.

3.2 Description and justification of the method

Recent studies of massive elliptical galaxies based on different approaches (stellar dynamical methods, weak and strong lensing, hydrostatic mass modeling, and their combinations) suggest that the gravitational potential $\Phi(r)$ is close to isothermal (e.g. Gerhard et al., 2001; Treu et al., 2006; Koopmans et al., 2006; Fukazawa et al., 2006; Churazov et al., 2010). For a singular isothermal sphere the gravitational potential can be written as $\Phi(r) = V_c^2 \ln(r)$, the circular velocity curve is flat, $V_c(r) = \text{const}$, and the mass profile scales as $M(r) \propto r$. So if the total gravitational potential of the galaxy is indeed isothermal, it can be characterized with a single parameter - the circular speed V_c . Therefore to the first approximation it is sufficient to determine V_c at any radius and the task is to identify the radius at which the circular speed can be measured most accurately.

Stars in early-type galaxies can be considered as a collisionless system immersed in a gravitational field. Let us consider a spherical galaxy in the equilibrium state. Stars in such systems obey the Jeans equations which in the spherical coordinates (r, θ, ϕ) can be

simply written as

$$\frac{d}{dr} j \sigma_r^2 + 2 \frac{\beta}{r} j \sigma_r^2 = -j \frac{d\Phi}{dr} = -j \frac{GM(r)}{r}, \quad (3.1)$$

where $j(r)$ ¹ is the stellar number density, $\sigma_r(r)$ is the radial velocity dispersion (weighted by luminosity), $\beta(r) = 1 - \frac{\sigma_\phi^2 + \sigma_\theta^2}{2\sigma_r^2}$ is the stellar anisotropy parameter, $M(r)$ is the total mass profile². The anisotropy $\beta(r)$ reflects the distribution of stellar orbits. If all stars in a galaxy are on circular orbits, then $\beta \rightarrow -\infty$, for pure radial orbits $\beta = 1$, and $\beta = 0$ for isotropic distribution of orbits.

We can link the unobservable quantites $j(r)$, $\beta(r)$ and $\sigma_r(r)$ with observable ones - a surface brightness $I(R)$ and a line-of-sight velocity dispersion $\sigma_p(R)$ profiles - via the following equations:

$$I(R) = 2 \int_R^\infty \frac{j(r)r dr}{\sqrt{r^2 - R^2}}, \quad (3.2)$$

$$\sigma_p^2(R) \cdot I(R) = 2 \int_R^\infty j(r) \sigma_r^2(r) \left(1 - \frac{R^2}{r^2} \beta(r)\right) \frac{r dr}{\sqrt{r^2 - R^2}}. \quad (3.3)$$

Nevertheless, the set of equations (3.1)-(3.3) is not closed. An inherent mass-anisotropy degeneracy does not allow us to solve it for the mass $M(r)$ and anisotropy $\beta(r)$ profiles simultaneously. Traditionally the degeneracy is overcome by assuming some parametric form of the mass or anisotropy profiles and fitting the resulting models to the observed $I(R)$ and $\sigma_p(R)$. However, both $M(r)$ and $\beta(r)$ are still poorly constrained from observational data alone (i.e., $I(R)$ and $\sigma_p(R)$) without resorting to the state-of-the-art modeling or adding detailed information on the line profiles. Here we discuss a technique that allows to estimate the mass of a galaxy without apriori parametrization of $M(r)$ and/or $\beta(r)$.

Assuming the logarithmic (isothermal) form of the gravitational potential $\Phi(r) = V_c^2 \ln(r) + const$ one can solve analytically the spherical Jeans equation coupled with equations (3.2)-(3.3) for three types of tracers' orbits - isotropic ($\beta = 0$), radial ($\beta = 1$) and circular ($\beta \rightarrow -\infty$). Note that for a typical stellar distribution $j(r)$ the projected velocity dispersion profile $\sigma_p(R)$ behaves differently depending on the value of β . In case of pure radial stellar orbits $\sigma_p(R)$ rapidly declines with the projected radius R , for the isotropic distribution of orbits $\sigma_p(R)$ declines much slower and, finally, $\sigma_p(R)$ increases with R for the circular orbits (e.g. Richstone and Tremaine, 1984; Churazov et al., 2010, Figure 3). So there is an ‘optimal radius’ where the projected velocity dispersion profiles for different values of anisotropy (almost) intersect each other. The existence of such a radius is discussed in Richstone and Tremaine (1984), Gerhard (1993). The method based on this observation is presented in detail in Churazov et al. (2010) and Lyskova et al. (2012).

It is practical to express the circular speed in terms of the observable surface brightness and line-of-sight velocity dispersion profiles. For the logarithmic form of the gravitational

¹Throughout this paper we denote a projected 2D radius as R and a 3D radius as r .

²Here we treat stars as test particles in the gravitational field $\Phi(r)$.

potential $\Phi(r) = V_c^2 \ln(r)$ the circular velocity V_c profiles for isotropic, radial and circular orbits are given by Churazov et al. (2010):

$$\begin{aligned} V_c^{\text{iso}} &= \sigma_p(R) \sqrt{1 + \alpha + \gamma} \\ V_c^{\text{circ}} &= \sigma_p(R) \sqrt{2 \frac{1 + \alpha + \gamma}{\alpha}} \\ V_c^{\text{rad}} &= \sigma_p(R) \sqrt{(\alpha + \gamma)^2 + \delta - 1}, \end{aligned} \quad (3.4)$$

where

$$\alpha \equiv -\frac{d \ln I(R)}{d \ln R}, \quad \gamma \equiv -\frac{d \ln \sigma_p^2}{d \ln R}, \quad \delta \equiv \frac{d^2 \ln [I(R) \sigma_p^2]}{d (\ln R)^2}. \quad (3.5)$$

Often the subdominant terms γ and δ can be neglected, i.e. the dispersion profile is assumed to be flat and the curvature of $I(R)$ to be small, and equations (3.4) are simplified to:

$$\begin{aligned} V_c^{\text{iso}} &= \sigma_p \sqrt{\alpha + 1} \\ V_c^{\text{circ}} &= \sigma_p \sqrt{2 \frac{\alpha + 1}{\alpha}} \\ V_c^{\text{rad}} &= \sigma_p \sqrt{\alpha^2 - 1}. \end{aligned} \quad (3.6)$$

Let us call a ‘sweet spot’ R_{sweet} the radius at which all three curves $V_c^{\text{iso}}(R)$, $V_c^{\text{circ}}(R)$ and $V_c^{\text{rad}}(R)$ are very close to each other. At this radius the circular speed uncertainty due to the unknown stellar anisotropy is minimal. From the equations (3.6) it is clear that for $\alpha = 2$ the relation between V_c and σ_p is the same for all types of orbits. So in the general case the sweet spot is expected to be located not far from the radius R_2 where the surface brightness declines as R^{-2} which is in turn close to the half-light radius R_{eff} (see also Wolf et al. 2010). If $I(R) \propto R^{-2}$ over some range of radii $[R_1, R_2]$, then the V_c -estimates based on equations (3.4) or (3.6) should work well over the whole range $[R_1, R_2]$.

While the derivation of equations (3.4), (3.6) relies on the assumption of a flat circular velocity profile, it works well even in case of slowly varying $V_c(r)$. Lyskova et al. (2012) have tested the method on a sample of cosmological simulations of elliptical galaxies from Oser et al. (2010) and have shown that the circular speed can be recovered to a reasonable accuracy. The rms-scatter in the circular velocity estimate has been found to be 5.4% for present-day simulated massive elliptical galaxies without signs of significant rotation, while the sample averaged bias is less than 1%.

3.2.1 Rotation of galaxies.

Elliptical galaxies can be divided into two broad families: (1) normal ellipticals, which show significant rotation, tend to be flattened and have an oblate-spheroidal shape; and (2) giant ellipticals, which are almost non-rotating, less flattened and tend to be triaxial

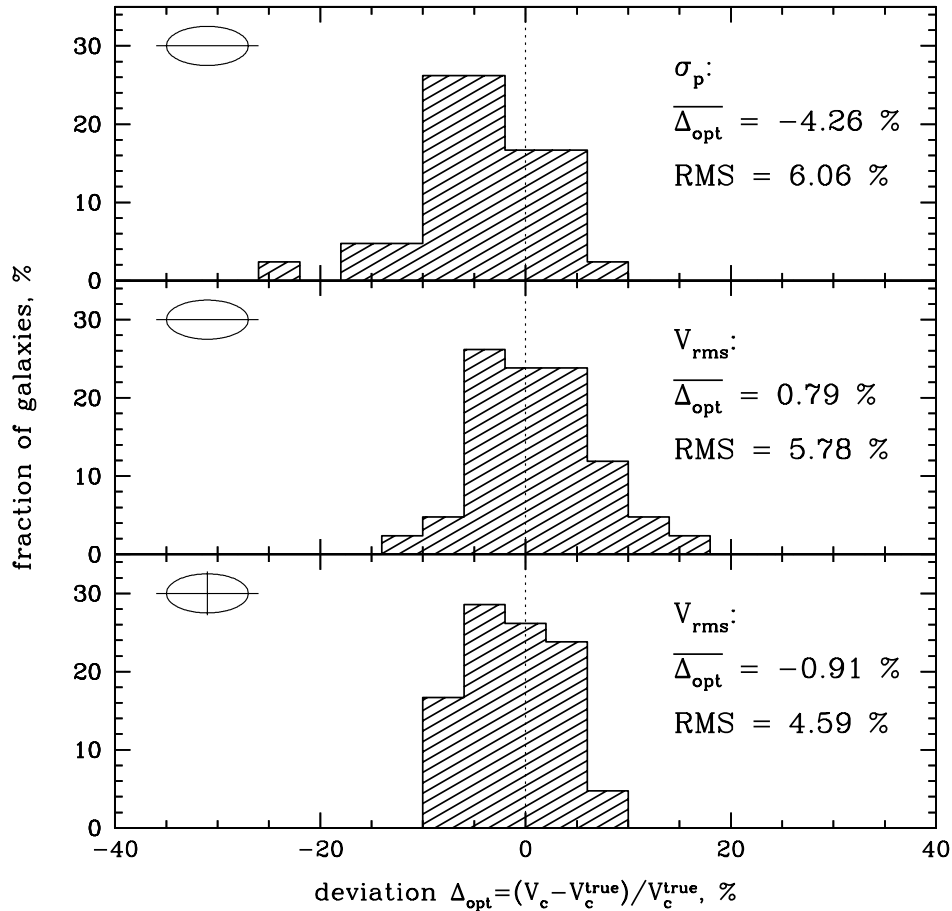


Figure 3.1: The fraction of galaxies (in %) as a function of deviation $\Delta_{opt} = (V_c^{\text{iso}} - V_c^{\text{true}}) / V_c^{\text{true}}$ for the sample of simulated galaxies with $\sigma_p(R_{\text{eff}}) > 150 \text{ km s}^{-1}$. Each galaxy is analysed for a set of random projections. For each projection the values of $I(R)$, $\sigma_p(R)$ and $V_{\text{rot}}(R)$ are calculated. The resulting V_c -estimates for all possible inclination angles for each galaxy are averaged. The black histogram in the upper panel results from ‘traditional’ analysis of $I(R)$ and $\sigma_p(R)$ profiles measured along a slit that is aligned with a major axis of a galaxy without taking into account $V_{\text{rot}}(R)$. In this case the V_c -estimate when averaged over the sample is biased low. The bias could be compensated when considering $V_{\text{rms}}(R) = \sqrt{\sigma_p(R) + V_{\text{rot}}(R)}$ instead of $\sigma_p(R)$ in equations (3.4), which is shown in the middle panel. The histogram in the lower panel shows V_c -estimates, when profiles along major and minor axes are available and V_{rms} is used. The averaged over the sample estimate is almost unbiased, the distribution looks roughly symmetric and the rms-scatter is moderate.

(e.g. Kormendy et al., 2009; Emsellem et al., 2007). Strictly speaking, the method in its original form is applicable only to non-rotating spherical galaxies, i.e. to no real ellipticals. Nevertheless, as tests on simulated galaxies show, the method still allows to recover the circular speed for massive elliptical galaxies without signs of significant rotation. For galaxies with rotational support the value of V_c derived from the observed $\sigma_p(R)$ using equations (3.4) or (3.6) will be likely underestimated. Can we reduce a bias arising from rotation to extend the method on fast-rotating elliptical galaxies?

Let us consider a disk rotating with the velocity $\tilde{V}_{\text{rot}}(R)$. When observed at an inclination angle i , where $i = 0^\circ$ corresponds to a face-on projection, the observed rotation velocity along an apparent major axis is simply $V_{\text{rot}}(R) = \tilde{V}_{\text{rot}}(R) \sin i$. After averaging over different inclination angles $0 \leq i \leq \pi/2$ we get

$$\langle V_{\text{rot}}^2 \rangle = \int_0^{\pi/2} V_{\text{rot}}^2 \cos i \, di = \int_0^{\pi/2} \tilde{V}_{\text{rot}}^2 \sin^2 i \cos i \, di = \frac{1}{3} \tilde{V}_{\text{rot}}^2. \quad (3.7)$$

Thus the true rotation velocity is $\sqrt{3}$ times larger than the sample averaged observed velocity. This relation is similar to the relation between the simple V_c -estimate and the observed projected velocity dispersion near the sweet point (eq. 3.6, $\alpha = 2$). As the conversion coefficient at the sweet point does not (strongly) depend on the unknown configuration of stellar orbits, one can use the quantity $V_{\text{rms}}^2(R) = \sigma_p^2(R) + V_{\text{rot}}^2(R)$ (rms-speed), where $V_{\text{rot}}(R)$ is the observed rotation velocity, instead of $\sigma_p(R)$ in equation (3.4) or (3.6) to estimate the circular speed of a sample of galaxies that includes also fast rotators. It is clear that for oblate rotating galaxies the V_c inferred from V_{rms} is overestimated for the edge-on view and underestimated when the disk is viewed face-on. But after averaging over different inclination angles the bias disappears. The conjecture on using V_{rms} instead of $\sigma_p(R)$ in equation (3.4) or (3.6) has been further tested on a sample of resimulated galaxies from the high-resolution cosmological simulations of Oser et al. (2010). The sample includes both fast and slow rotators in a proportion that is generally consistent with findings of ATLAS^{3d} project (Emsellem et al., 2007, 2011; Naab et al., 2013).

First, for each simulated galaxy in the sample we measure the surface brightness, projected velocity dispersion and rotational velocity profiles along the apparent major axis of the galaxy, mimicing long-slit observations. Then we estimate the circular speed in two ways: 1) using information about $\sigma_p(R)$ (eq. 3.4) and 2) using $V_{\text{rms}}(R) = \sqrt{\sigma_p^2(R) + V_{\text{rot}}^2(R)}$ instead of $\sigma_p(R)$. As a next step we calculate the average deviation Δ_{opt} of the estimated circular speed from the true one $V_c^{\text{true}}(r) = \sqrt{GM()/r}$, after averaging over all possible inclination angles. We consider only galaxies with the value of the projected velocity dispersion at the effective radius $\sigma_p(R_{\text{eff}})$ greater than 150 km s⁻¹ (when the galaxy is viewed edge-on). The sample consists of 26 objects. The results of the analysis are presented in the form of histograms (fraction of galaxies versus deviation of the V_c -estimate from the true value) in Figure 3.1. In the upper panel of Figure 3.1 we show the histogram for the case when rotation is neglected. On average V_c is underestimated by $\overline{\Delta_{\text{opt}}} = -4.3\%$. If we substitute $\sigma_p(R)$ with $V_{\text{rms}}(R) = \sqrt{\sigma_p^2(R) + V_{\text{rot}}^2(R)}$ then we get almost unbiased (within

statistical errors) estimate of the circular speed with rms-scatter of $\approx 6\%$ (the middle panel of Figure 3.1). While for oblate ellipticals observations along the major axis carry all information needed for simple mass estimation, for triaxial galaxies rotation along the apparent minor axis might be significant. In a case when information is available along major and minor axes of a galaxy, using $V_{\text{rms}}^2 = \frac{I_1 V_{\text{rms},1}^2 + I_2 V_{\text{rms},2}^2}{I_1 + I_2}$ makes the distribution of $\Delta_{\text{opt}} = (V_c - V_c^{\text{true}})/V_c^{\text{true}}$ more symmetric than for the ‘one slit’ case and reduces the rms-scatter down to 4.6% (lower panel of Figure 3.1). Note, that for the sample consisting of oblate rotating galaxies only there is no sense to use the weighted rms-speed $V_{\text{rms}}^2 = \frac{I_1 V_{\text{rms},1}^2 + I_2 V_{\text{rms},2}^2}{I_1 + I_2}$ as it leads to the underestimated value of V_c (compare the averaged deviations in the middle and lower panels). But for the sample containing also triaxial halos this approach helps to reduce the scatter and does not strongly bias the V_c -estimate. At least, for our sample of 26 simulated objects the bias is not significant, i.e., $\overline{\Delta_{\text{opt}}} < RMS/\sqrt{N}$.

3.2.2 An algorithm for estimating V_c

Based on the results of Lyskova et al. (2012) and the arguments presented in the previous section, the following algorithm has been developed:

1. Calculate the logarithmic derivatives α , γ and δ from the observed surface brightness $I(R)$ and line-of-sight velocity dispersion $\sigma_p(R)$ profiles using equations (3.5).
2. Calculate the circular speed $V_c(R)$ for isotropic, radial and circular stellar orbits using equations (3.4) in the case of reliable data (full analysis) or equations (3.6) in the case of poor or noisy observational data (simplified analysis). For rotating galaxies use $V_{\text{rms}}(R)$ instead of $\sigma_p(R)$ in equations (3.4) or (3.6).
3. Estimate V_c as $V_c^{\text{iso}}(R_{\text{sweet}})$ at the sweet spot R_{sweet} - the radius at which all three curves $V_c^{\text{iso}}(R)$, $V_c^{\text{circ}}(R)$ and $V_c^{\text{rad}}(R)$ are maximally close to each other. At R_{sweet} the sensitivity of the method to the anisotropy parameter β is believed to be minimal so the estimation of the circular speed at this particular point is not affected much by the unknown distribution of stellar orbits.

3.3 Analysis

3.3.1 M87, revisited. Illustration of the Method

In this section we illustrate all the steps of the described algorithm on one massive galaxy - M87 (NGC4486). M87 is a nearby (16.1 Mpc) giant elliptical galaxy, luminous in X-rays. Its mass profile has been investigated in detail by a variety of methods. A technique analogous to the one described in Section 3.2.2 has already been applied to M87 (Churazov et al., 2010). However, new data on stellar kinematics warrant a reanalysis of the data.

Since the 1960s M87 has been extensively explored and there is a large amount of observational data. We focus here on a recent work by Murphy et al. (2011) (hereafter ‘M11’), who estimated M87’s mass profile from axisymmetric orbit-based modeling and compared the resulting total enclosed mass profile with other mass estimates available in the literature.

Schwarzschild modeling (Schwarzschild, 1979) is considered to be a state-of-the-art method for dynamical investigation of nearby galaxies which allows one to recover masses and orbital anisotropies with $\sim 15\%$ accuracy (Thomas et al., 2005). This technique consists in analysis of the three-dimensional orbital structure of a stellar system in an assumed gravitational potential and representation of the observed photometric and kinematic data by a superposition of constructed orbits. The system is assumed to be in dynamical equilibrium and as a rule to be viewed edge-on (e.g. Gebhardt et al., 2000, 2003; Thomas et al., 2004, 2005).

We assume that the mass and circular speed profiles for M87 derived in M11 are accurate and unbiased (as significant inherent systematic uncertainties are not expected to be in dynamical models (e.g. Thomas et al., 2007)) and compare our simple estimates with these curves.

For the analysis we use the same set of data as in M11. Namely, the stellar surface brightness profile comes from Kormendy et al. (2009) (the V-band photometry), the stellar kinematic data come from the publicly available SAURON data set (Emsellem et al., 2004) and from M11 (VIRUS-P instrument).

We first compute the auxiliary coefficients α , γ and δ (eq. 3.5) from the smoothed $I(R)$ and $\sigma_p(R)$ profiles (the smoothing procedure is described in Churazov et al. 2010). The profiles $I(R)$ and $\sigma_p(R)$ for M87 are shown in Figure 3.2, panels (A) and (B). The stellar surface density from Kormendy et al. (2009) is shown as red squares. The velocity dispersion measurements from SAURON and VIRUS-P are shown as red circles and black squares, respectively. When smoothing the projected velocity dispersion profile, we use only SAURON data in the radial range $R \lesssim 8''$, both SAURON and VIRUS-P between $8'' \leq R \leq 16''$ and only VIRUS-P for $R \geq 16''$ as is done in M11. The logarithmic derivatives are shown in panel (C). Note that $\alpha \approx 2$ in the range $100'' \leq R \leq 600''$. In this radial range we expect a weak dependence on the anisotropy parameter β and the isotropic curcular velocity curve to be a good representation of the true circular speed profile. Using equations (3.4) we calculate $V_c(R)$ for an isotropic distibution of stellar orbits (shown in blue), for pure radial and pure circular orbits (in green and magenta, correspondingly). These three curves intersect each other at the sweet spot $R_{\text{sweet}} \approx 115''$ where we estimate $V_c^{\text{opt}}(R_{\text{sweet}}) \equiv V_c^{\text{iso}}(R_{\text{sweet}}) \approx 510.8 \text{ km s}^{-1}$. The relative error of this estimate at R_{sweet} with respect to the circular speed $V_c^M(R_{\text{sweet}})$ from M11 (Figure 3.2, panel (D), solid black line) is equal to $\Delta = (V_c^{\text{opt}} - V_c^M) / V_c^M = 4.3\%$. Within expected uncertainties³ our simple estimate at the sweet point agrees well with the circular speed obtained from Schwarzschild modeling.

³5.4% was found in Lyskova et al. (2012) for a sample of simulated massive slowly rotating simulated galaxies

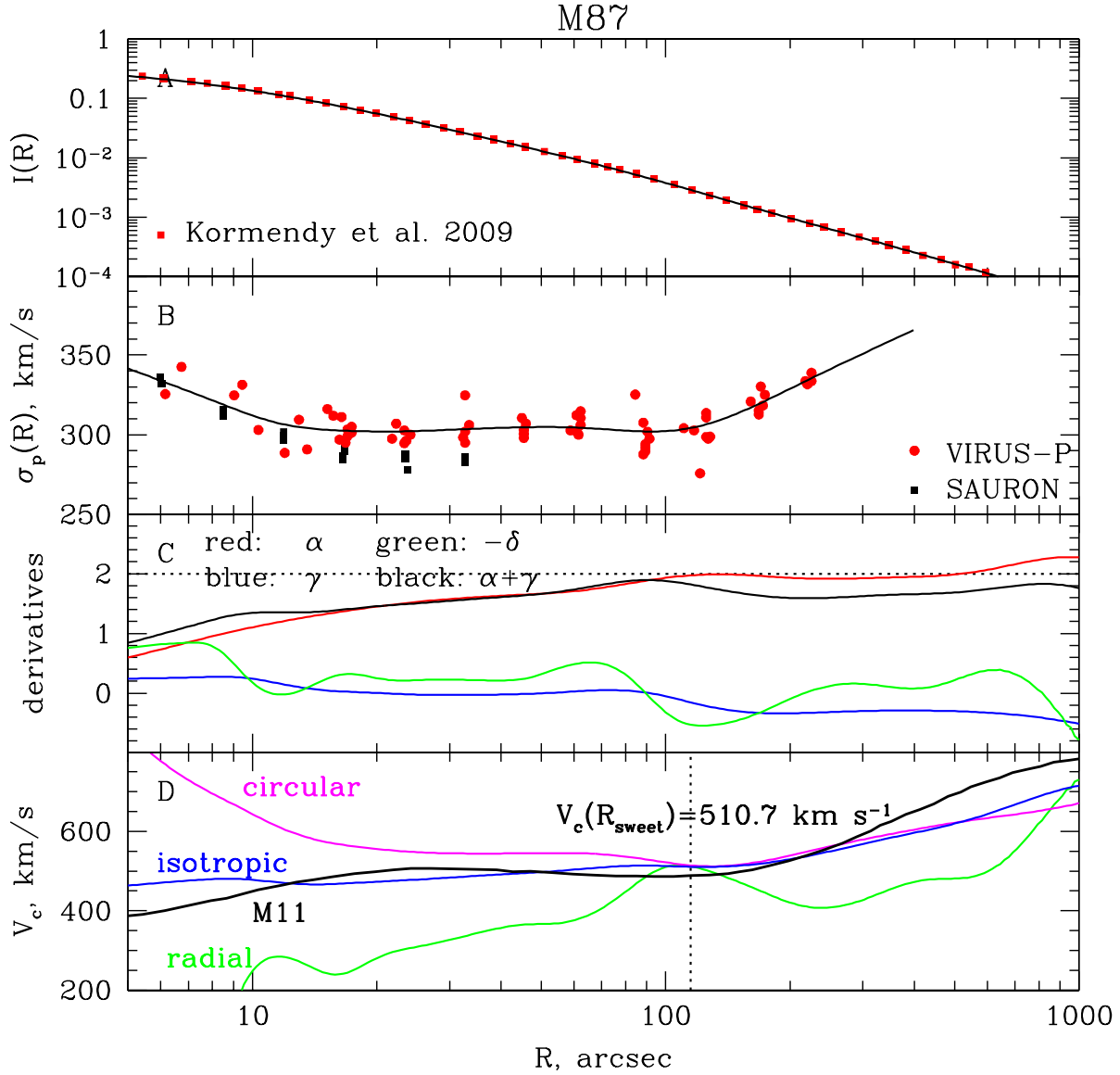


Figure 3.2: Circular speed estimate of M87. The stellar surface brightness and the line-of-sight velocity dispersion profiles are shown in panels (A) and (B) correspondingly. Data are represented as points and smoothed curves used to compute the auxiliary coefficients α, γ, δ as black solid lines. The logarithmic derivatives $\alpha, \gamma, -\delta$ and $\alpha + \gamma$ (eq. 3.5) are shown in panel (C) in red, blue, green and black, respectively. Circular velocity curves for isotropic orbits of stars (in blue), pure radial (green) and pure circular (magenta) orbits as well as the circular speed (in black) derived in M11 are presented in panel (D).

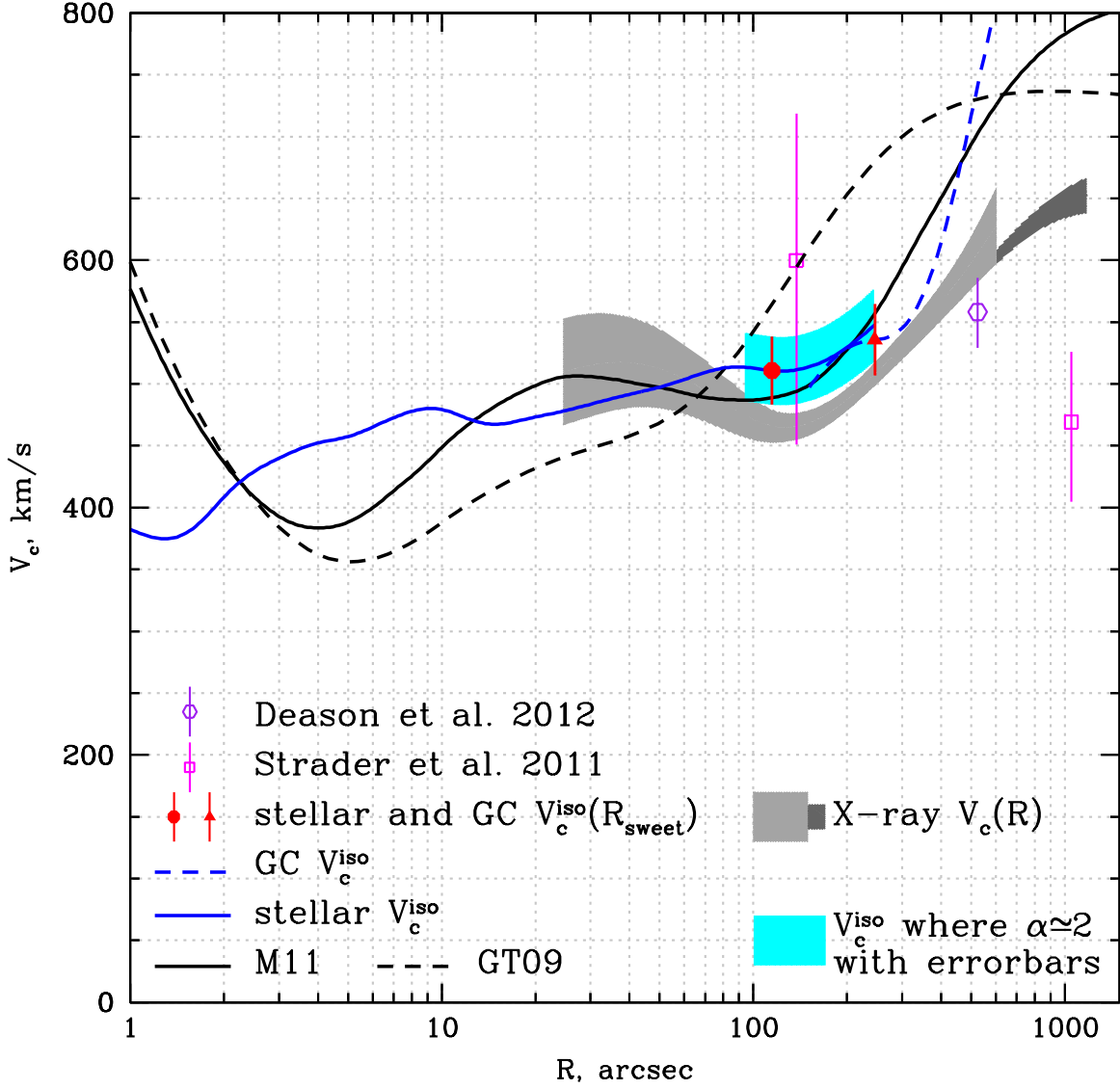


Figure 3.3: Comparison of the simple circular speed estimates for M87 with V_c -profiles inferred from the state-of-the-art modeling. The solid line shows the best-fitting model of M11, the dashed line - the V_c -profile from GT09. V_c^{iso} resulting from the same set of data (mainly, stellar kinematic and photometry) as used in M11 is shown as a blue solid line. The dashed blue line is V_c^{iso} -profile derived from GC data as used in GT09. The red circle and the red triangle represent our simple V_c -estimates derived on the basis of same data sets used in M11 and in GT09, respectively. Shown in grey are V_c -profiles from Chandra and XMM data with errorbars. V_c -estimates from recent works (Deason et al. 2012 and Strader et al. 2011) are shown as purple and magenta dots with errorbars.

The method under consideration is not only simple and fast in implementation, the resulting estimate does not strongly depend on the quality of observational data. To demonstrate this we apply the analysis to the set of data used in the state-of-the-art modeling of M87 by Gebhardt and Thomas (2009) (hereafter ‘GT09’). GT09 as well as M11 derive the mass profile of M87 employing basically the same axisymmetric orbit-based dynamical models. The only difference is the observational data used. GT09 use stellar kinematic data from SAURON (Emsellem et al., 2004) and from van der Marel (1994) at $R \lesssim 40''$. At larger radii GT09 use the surface density profile from McLaughlin (1999) for the globular clusters (GC) and individual globular cluster velocities reported in Côté et al. (2001). For this data set our analysis results in $V_c = 535.6 \text{ km s}^{-1}$ at $R_{\text{sweet}} = 245.5''$. This estimate is basically based only on the GC data. It is about 21% smaller than the circular speed derived by GT09 but it agrees well ($\Delta = 3.8\%$) with the rotation curve from M11. Figure 3.3 shows the circular speed profiles resulting from different methods. The profiles derived from detailed dynamical modeling of M11 and GT09 are shown as black solid and dashed lines, respectively. The simple estimates derived in this work are shown as a red circle (based on the set of data used in M11) and a red triangle (from data used in GT09). The grey shaded region represents the result of the X-ray analysis of available archive XMM and Chandra data. The X-ray data are deprojected assuming spherical symmetry to derive gas density and temperature profiles (see Section 3.3.3 for more detail). Using derived profiles and the hydrostatic equilibrium equation the mass profile is derived. The width of the shaded area is determined mainly by systematic deviations of $V_c(R)$ derived under an assumption of a fixed or free metal abundances (see details in Section 3.3.3) rather than statistical variations. The dark grey shaded region is based on XMM data only. The discrepancy between the profiles from dynamical modeling and from X-ray analysis can be explained by the contribution of a gas non-thermal pressure to the total pressure (Churazov et al., 2008). A wiggle in the X-ray-based $V_c(R)$ at $R \sim 200''$ is due to a quasi spherical shock generated by the supermassive black hole at the center of M87.

If we compare the optical circular speed estimate for M87 at the sweet spot with the X-ray based one at the same radius, we get $\frac{V_c^{\text{opt}}}{V_c^X} \approx 1.1$, what implies $\sim 20\%$ non-thermal pressure support. It should be noted, however, that the sweet radius happens to lie in the vicinity of the shock front (Forman et al., 2007) and the X-ray circular speed might be underestimated in the region of a ‘dip’. Previously, the comparison of the X-ray data on M87 with the analysis of the optical data in Romanowsky and Kochanek (2001) and GT09 has been done in Churazov et al. (2008) and Churazov et al. (2010) respectively. In the first case (Romanowsky and Kochanek 2001 + X-Rays) no evidence for non-thermal pressure in excess of $\sim 10\%$ of the thermal pressure was found, while the comparison with GT09 results yielded a large non-thermal component of order 50%. This discrepancy can be traced to the difference in the optical data. With new data and analysis of M11 this discrepancy largely goes away. Note also, that in Churazov et al. (2008, 2010) the circular speed estimate $\sim 440 \text{ km s}^{-1}$ was derived from X-rays via fitting the gravitational potential by $\Phi(R) = V_c^2 \ln r + \text{const}$ in the broad radial range from $0.1'$ to $5'$.

Table 3.1: Sample of elliptical galaxies. The columns are: (1) - common name of the galaxy; (2) - redshift from the NASA/IPAC Extragalactic Database; (3) - adopted distance; (4) - central velocity dispersion from HyperLeda; (5) - hydrogen column density from (Dickey and Lockman, 1990).

Name (1)	z (2)	D , Mpc (3)	σ_c , km s $^{-1}$ (4)	N_H , 10 20 cm $^{-2}$ (5)
NGC 708	0.016195	68.3	229.8 ± 9.7	5.37
NGC 1129	0.017325	73.1	329.5 ± 15.1	9.81
NGC 1550	0.012389	52.1	308.0 ± 6.2	11.5
NGC 4125	0.004523	23.9	226.8 ± 6.9	1.84
UGC 3957	0.034120	145.9	331.1 ± 35.1	4.63

Table 3.2: Log of the observations

Galaxy	Slit PA (deg)	Date	Slit width (arcsec)	Sp. range (rA)	Sp. resol. (rA)	Exp. time (min)	Seeing (arcsec)
NGC 708	-4	05.10.2011	1.0	4840–5610	2.2	180	1.1–1.2
	215	03.10.2011	1.0	4840–5610	2.2	185	1.4–3.5
NGC 1129	166	21.10.2012	0.5	4080–5810	3.0	180	1.2–1.4
	256	15.10.2012	0.5	4080–5810	3.0	180	1.4–1.5
NGC 1550	116	09.12.2012	1.0	3700–7200	5.1	180	1.5–1.6
	206	16-17.10.2012	0.5	4080–5810	3.0	180	1.3–1.6
NGC 4125	175	14.04.2013	1.0	4840–5610	2.2	160	1.2–1.3
	265	19.10.2012	0.5	4080–5810	3.0	200	1.6–1.7
UGC 3957	287	03.11.2010	1.0	4415–6015	2.2	180	1.1–1.5

3.3.2 Observations and data reduction

The spectroscopic observations at the prime focus of the SAO RAS 6-m telescope were made with the multi-mode focal reducer SCORPIO (Afanasiev and Moiseev, 2005) and its new version SCORPIO-2 (Afanasiev and Moiseev, 2011). When operated in the long-slit mode, both devices have same slit 6 arcmin in height with a scale of 0.36 arcsec per pixel. However, with a similar spectral resolution SCORPIO-2 provides twice larger spectral range. The CCDs employed were an EEV 42-40 in the SCORPIO and E2V 42-90 in the SCORPIO-2.

Table 3.1 lists the target galaxies and Table 3.2 gives the log of observations: the position angles of the spectrograph slit for each galaxy, the observing date, the slit width, spectral range, spectral resolution (estimated by the mean FWHM of air glow lines), total exposure T_{exp} , and seeing. Usually we observed targets with two slit positions: along photometric major and minor axes. The exceptions are NGC 708 (the second slit was placed along the dust lane crossed galaxy nucleus) and UGC 3957 where observations only along major axis have been performed.

The data reduction were made in a standard way using the IDL-based software package developed at the SAO RAS (Afanasiev and Moiseev, 2005). The measurements of the distribution of line-of-sight velocities V_{rot} and stellar velocity dispersion σ_p were carried out by cross-correlating the spectra of galaxies with the spectra of the template star observed on the same nights. The measurement technique has already been described in our previous papers (Moiseev, 2001; Sil'chenko, Moiseev A. V. and Shulga, 2010). We observed several template stars belonging to the spectral types III G8 - III K5 and also twilling light sky (i.e. solar spectrum). For the final measurements, we selected a template giving a maximum correlation coefficient. During the stellar kinematics parameters estimation we applied logarithmic binning along the slit to provide a sufficient signal-to-noise ratio ($S/N > 15-20$ per bin in each pixel). Also in each beam we calculated the surface brightness $I(R)$ as an integral intensity of stellar continuum at the range 5040 – 5140 rArA. The Figure 3.4 shows the results of our spectral observations together with V -band images of the galaxies taken at the same nights in the direct image mode of SCORPIO and SCORPIO-2.

3.3.3 Circular speed from X-ray data.

Using publicly available Chandra data we have derived the circular speed profiles for galaxies in our sample under the assumption of the hydrostatic equilibrium. We follow the procedure of the data analysis described in Churazov et al. (2010). Here we only outline the major steps.

First, in each observation we follow the reduction procedure described in Vikhlinin et al. (2005), i.e. filter out high background periods and apply the latest calibration corrections to the detected X-ray photons, and determine the background intensity.

As a next step we apply a non-parametric deprojection procedure described in Churazov et al. (2003, 2008). In brief, the observed X-ray spectra in concentric annuli are modeled as a linear combination of spectra in spherical shells; the two sequences of spectra are related by a matrix describing the projection of the shells into annuli. To account for the projected contribution of the emission from the gas at large distances from the center (i.e., at distances larger than the radial size r_{max} of the region well covered by actual observations) one has to make an explicit assumption about the gas density/temperature profile. We assume that at all energies the gas volume emissivity at $r > r_{\text{max}}$ declines as a power law with radius. The slope of this power law is estimated based on the observed surface brightness profile at $r \lesssim r_{\text{max}}$. Since we assume that the same power law shape is applicable to all energy bands, effectively this assumption implies constant spectral shape and therefore the isothermality of the gas outside r_{max} . The contribution of these layers is added to the projection matrix with the normalization as an additional free parameter. The final projection matrix is inverted and the shells' spectra are explicitly calculated by applying this inverted matrix to the data in narrow energy channels.

The resulting spectra are approximated in XSPEC (Arnaud, 1996) with the Astrophysical Plasma Emission Code (APEC) one-temperature optically thin plasma emission model (Smith et al., 2001). The redshift z (from the NASA/IPAC Extragalactic Database – NED) and the line-of-sight column density of neutral hydrogen N_H (Dickey and Lockman, 1990)

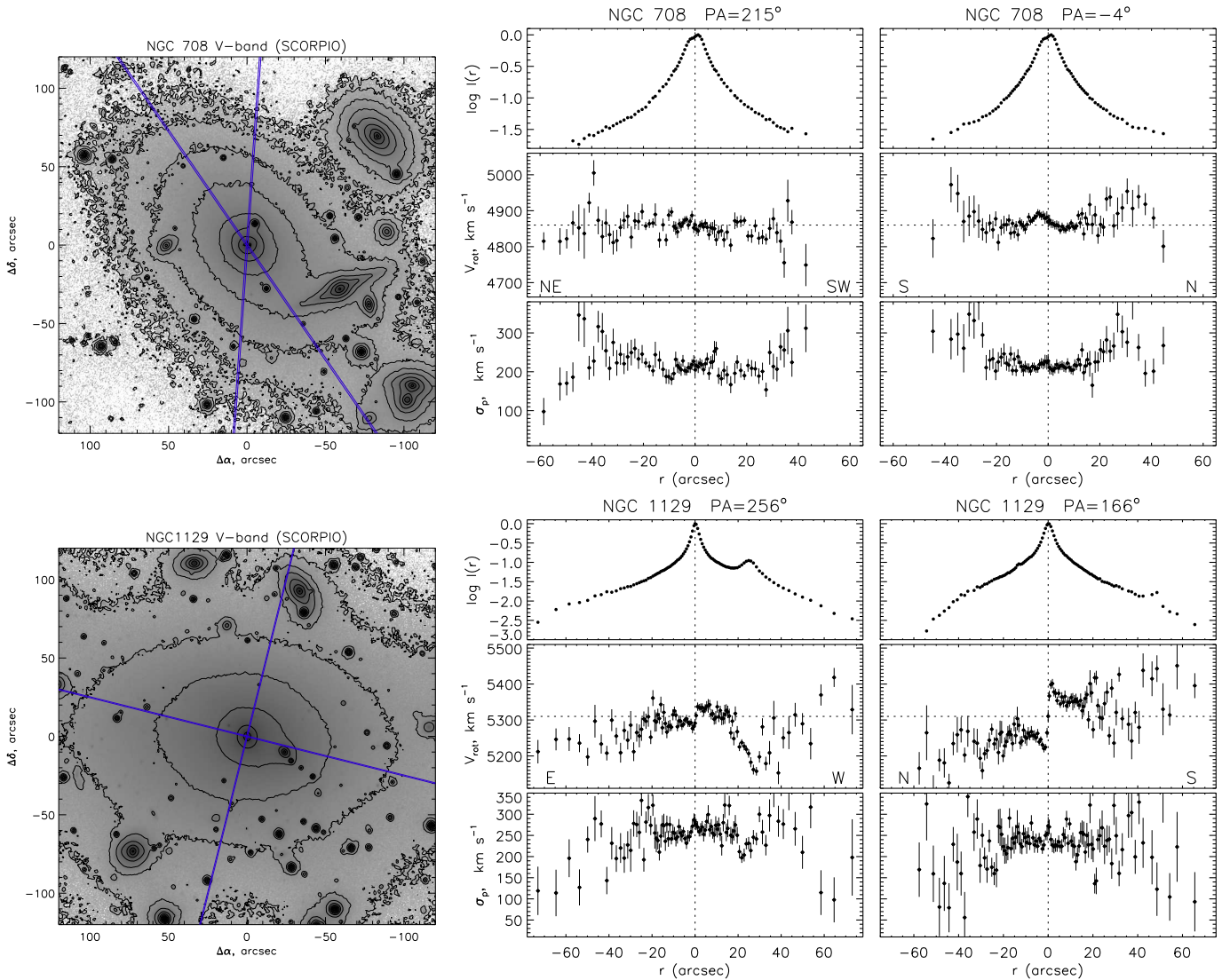


Figure 3.4: The results of the SAO RAS 6-m telescope observations. Left: V -band image in logarithmic grey-scale and positions of the spectrograph slits. Middle: the distributions of stellar continuum surface brightness, line-of-sight velocities and velocity dispersion of stars along major axis. The dotted lines mark the position of nucleus and accepted systemic velocity. In the case of NGC 1129 at $r \approx 20 - 30$ arcsec the slit crosses the companion galaxy. Right: the same for the second slit position.

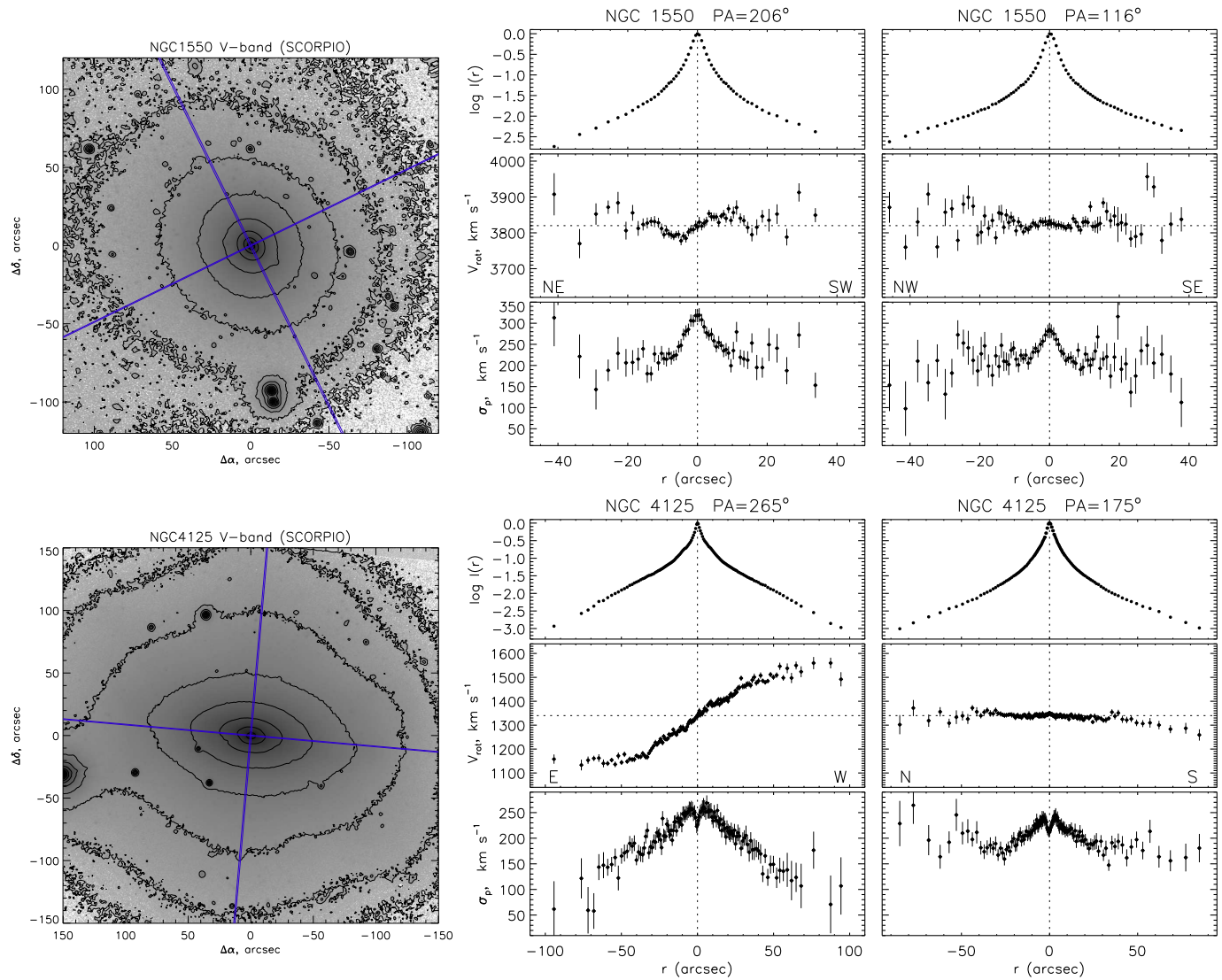


Figure 3.4: (continue)

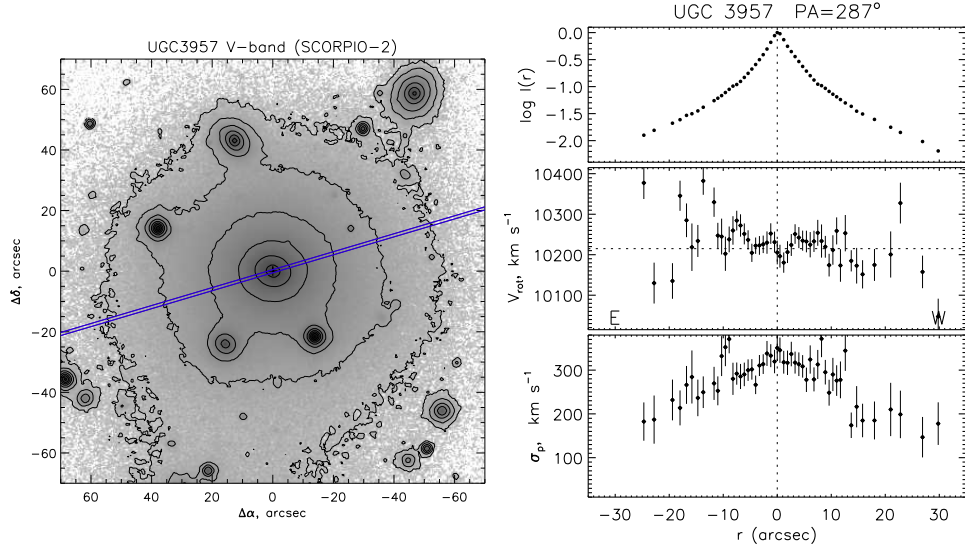


Figure 3.4: (continue)

have been fixed at the values given in Table 3.1. For each shell we determine the emission measure (and therefore gas density) and the gas temperature. These quantities are needed to evaluate the mass profile through the hydrostatic equilibrium equation. For cool (sub-keV) temperatures and approximately solar abundance of heavy elements, line emission provides a substantial fraction of the 0.5-2 keV flux. With spectral resolution of current X-ray missions the contributions of continuum and lines are difficult to disentangle. As a result the emission measure and abundance are anti-correlated, which can lead to a large scatter in the best-fit emission measures. As an interim (not entirely satisfactory) solution, we fix the abundance at 0.5 solar for all shells, using the default XSPEC abundance table of Anders & Grevesse (1989). We return to this issue below.

Knowledge of the gas number density n and temperature T in each shell allows us to evaluate the $M(R)$ or $V_c(R)$ profile by using the hydrostatic equilibrium equation:

$$-\frac{1}{\rho} \frac{dP}{dr} = \frac{d\Phi}{dr} = \frac{V_c^2}{r} = \frac{GM}{r^2}, \quad (3.8)$$

where $P = nkT$ is the gas pressure, $\rho = \mu m_p n$ is the gas density (m_p is the proton mass). The mean atomic weight μ is assumed to be equal to 0.61.

The resulting circular speed profiles $V_c^x(r)$ for all galaxies in our sample are shown as black thick lines with errorbars represented as black shaded regions in lower panels of Figure 3.6. One should keep in mind that in assuming hydrostatic equilibrium one neglects possible non-thermal contribution to the pressure, arising from turbulence in the thermal gas, cosmic rays, magnetic fields and non-radiating relativistic protons (e.g., Churazov et al., 2008). So comparing optical and X-ray estimates of the circular speed may provide constraints on the contribution of the non-thermal particles to the gas pressure. High-resolution cosmological simulations of galaxy clusters suggest that the gas motions contribute $\sim 5\%$ of the

total pressure support at the center and up to $\sim 15 - 20\%$ at r_{500} in relaxed systems (e.g. Lau, Kravtsov, Nagai, 2009; Zhuravleva et al., 2013). Recent studies on combining X-ray mass measurements and sophisticated stellar dynamical methods imply up to $\sim 50\%$ non-thermal support (e.g. Shen and Gebhardt 2010, Rusli et al. 2011, GT09), although the uncertainties in model assumptions may be significant (Buote and Humphrey, 2012). As our simple method provides a mass-estimate that is robust and largely insensitive to the orbital anisotropy at the sweet point, we interpret the offset at R_{sweet} between the X-ray and optical measurements as a signature of deviations from hydrostatic equilibrium. In particular, the ratio $f_{nt} = (M_{opt} - M^X)/M_{opt}$ provides an estimate of the fractional contribution of the nonthermal pressure to the total pressure, provided that this fraction does not vary with radius. In this approximation $M^{X,c}(r) = M^X(r)/(1 - f_{nt})$ is an estimate of the mass at other radii.

As the gas pressure is assumed to be isotropic, mismatch between the corrected X-ray circular speed $V_c^{X,c}$ and the isotropic one V_c^{iso} derived from the Jeans equation may give a clue regarding the orbital structure of the galaxy. E.g., at small radii $V_c^{X,c} > V_c^{\text{iso}}$ would suggest more circular orbits, while at larger radii this would correspond to more radial orbits. Of course, the reliability of such analogy strongly depends on the derived V_c^X and V_c^{iso} .

We now illustrate the impact of our assumption of a flat abundance profile $Z = 0.5Z_\odot$ and estimate arising errors on the inferred circular speed.

At low temperatures ($\lesssim 2$ keV) metal abundances derived from X-ray spectra with the limited energy resolution of current X-ray missions suffer from the ambiguity of disentangling line emission and continuum. While derived circular velocity is weakly sensitive to the particular value of metallicity in the spectral models, it can be significantly affected by the radial variations of the heavy-element abundance (e.g. Johnson et al., 2009; Churazov et al., 2010).

Since abundance measurements can be biased (e.g. Buote, 2000) we tried to make a conservative estimate of the varying abundance profile impact by setting by hand several model metallicity profiles and fitting the deprojected data again, leaving the normalization and temperature as free parameters.

As an example, we show in Figure 3.5 the derived density, temperature and circular speed profiles⁴ for NGC 0708. The estimated statistical errorbars come from 1000 Monte Carlo simulations. Here we consider 3 models: (i) flat abundance profile $Z = 0.5Z_\odot$ (shown in red), (ii) fit to the deprojected abundance with a ‘dip’ at the center (in blue) and (iii) physically motivated model (in green), where the metal abundance rises to the galaxy center as is generally expected for elliptical galaxies (e.g. Humphrey and Buote, 2006). Compared to the flat abundance profile, the metallicity monotonically increasing towards the center leads to the flattening of the gas density profile and lowering the final circular speed estimate. In contrast, the decreasing to the center $Z(r)$ ‘boosts’ inferred V_c^X , as is

⁴As eq. (3.8) requires differentiation, to calculate derivatives we smooth density, temperature and pressure profiles following the procedure described in Churazov et al. (2010). The typical value of the smoothing width is ~ 0.55 .

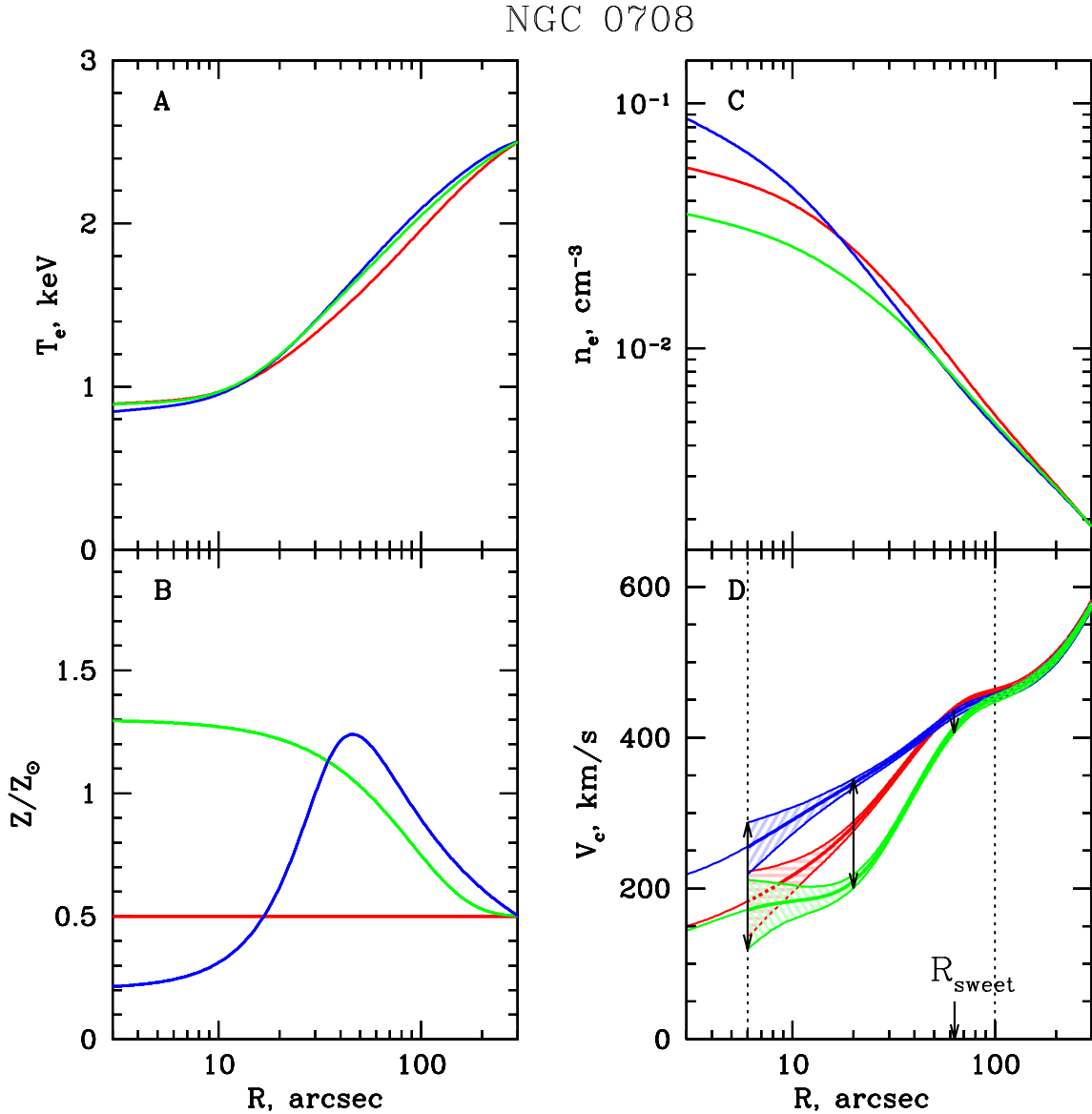


Figure 3.5: The effect of the abundance gradient on the calculated circular speed profile. Panel (A) shows the deprojected temperature for NGC 0708, panel (B) - assumed models for the metallicity, panel (C) - gas density profiles and panel (D) - resulting circular velocity curves with 1σ errors from 1000 Monte Carlo realizations. The vertical dotted lines indicate a region of interest where both optical and X-ray data are available. The arrows show the spread in circular speed estimates coming from different abundance profiles.

clearly seen from Figure 3.5.

Other galaxies in our sample show only monotonical increase of the deprojected metal abundance to the center, so the spread in final V_c^X -esimates is smaller. The circular velocity profiles corresponding to the flat abundance (thick solid black lines) and 1σ -errors from 1000 Monte Carlo simulations (black shaded area enclosed by two thin black lines) are shown in Figure 3.6.

3.3.4 Optical Rotation Curves

All observed galaxies in the sample are quite massive, close to spherical and slowly rotating (except maybe NGC 4125). This makes them suitable for our analysis. According to the algorithm for estimating the circular speed described in Section 3.2.2 we perform the following steps:

1. First, given the surface brightness I_i , projected velocity dispersion σ_{pi} with its errors $\Sigma_{\sigma i}$ and rotational velocity $V_{\text{rot}i}$ with its errors $\Sigma_{\text{rot}i}$ along two slits ($i = 1, 2$) we construct the average profiles

$$I = \frac{I_1 + I_2}{2}; \quad (3.9)$$

$$\sigma_p^2 = \frac{I_1 \sigma_{p1}^2 / \Sigma_{\sigma 1}^2 + I_2 \sigma_{p2}^2 / \Sigma_{\sigma 2}^2}{I_1 / \Sigma_{\sigma 2}^2 + I_2 / \Sigma_{\sigma 2}^2}. \quad (3.10)$$

If rotation velocity along the slit $V_{\text{rot}i}$ is not negligible, then instead of σ_p we use V_{rms} defined as

$$V_{\text{rms}}^2 = \frac{I_1 V_{\text{rms}1}^2 / \Sigma_{\text{rms}1}^2 + I_2 V_{\text{rms}2}^2 / \Sigma_{\text{rms}2}^2}{I_1 / \Sigma_{\text{rms}1}^2 + I_2 / \Sigma_{\text{rms}2}^2}, \quad (3.11)$$

where $\Sigma_{\text{rms}i}^2 = \Sigma_{\sigma i}^2 + \Sigma_{\text{rot}i}^2$; $\Sigma_{\text{rot}i}$ are the errorbars assigned to rotation velocity measurements.

2. Then we calculate the logarithmic derivatives α , γ and δ from the derived profiles using equations (3.5).
3. Next, we compute the circular speed $V_c(R)$ for isotropic, radial and circular stellar orbits using equations (3.4) in case of reliable data (full analysis) or equations (3.6) in case noisy or systematics affected observational line-of-sight velocity dispersion profile (simplified analysis). As discussed above, for rotating galaxies one should use $V_{\text{rms}}(R)$ instead of $\sigma_p(R)$ in equations (3.4) or (3.6).
4. $V_c^{\text{iso}}(R_{\text{sweet}})$ is taken as a final estimate of V_c at the sweet spot R_{sweet} - the radius at which all three curves $V_c^{\text{iso}}(R)$, $V_c^{\text{circ}}(R)$ and $V_c^{\text{rad}}(R)$ are maximally close to each

Table 3.3: V_c -estimates for our sample of elliptical galaxies derived from optical and X-ray analyses. The columns are: (1) - common name of the galaxy; (2) - sweet radius; (3) - optical V_c -estimate at R_{sweet} ; (4) - V_c -estimate at R_{sweet} from X-ray, in parentheses are presented the conservative error estimates ; (5) - gas temperature at R_{sweet} .

Name (1)	$R_{\text{sweet}}, \text{arcsec}$ (2)	$V_c^{\text{iso}}, \text{km s}^{-1}$ (3)	$V_c^X, \text{km s}^{-1}$ (4)	kT, keV (5)
NGC 708	63.1	371^{+53}_{-53}	$437^{+4}_{-4} (-31)$	1.7
NGC 1129	45.7	444^{+31}_{-44}	464^{+20}_{-25}	3.0
NGC 1550	30.9	382^{+12}_{-19}	$383^{+5}_{-6} (-29)$	1.2
NGC 4125	44.7	375^{+45}_{-36}	$322^{+7}_{-9} (-18)$	0.5
UGC 3957	14.8	476^{+43}_{-43}	$518^{+45}_{-66} (+47)$	2.2

other. At R_{sweet} the sensitivity of the method to the anisotropy parameter β is expected to be minimal so the estimation of the circular speed at this particular point is not affected much by the unknown distribution of stellar orbits. In case of the simplified version of the analysis $R_{\text{sweet}} \equiv R_2$, where $\alpha = -\frac{d \ln I(R)}{d \ln R} = 2$.

- Finally, we compare derived V_c -estimates with the X-ray circular speed at the same radius. Table 3.3 summarizes the results, providing both optical and X-ray circular speed estimates as well as the temperature of the hot gas at R_{sweet} . The scatter in optical V_c arises from differences in observed $I(R)$ and $\sigma_p(R)$ along two slits or from measurement errors of $\sigma_p(R)$ when information is available along one slit only. Errors for X-ray derived V_c comes from 1000 Monte Carlo realizations. In parentheses we present the conservative estimate of errors for the case of radially varying metallicity.

In Figure 3.6 we present results of the analysis. The logarithmic slope of the surface brightness profile for each galaxy in our sample is shown in panel A. Thin red lines correspond to slopes measured along the individual slits, while the thick lines show the average profiles (eq. 3.9). The shaded area indicates the scatter in profiles arising from different slits (when available). The derived profiles for V_c^{iso} , V_c^{circ} and V_c^{rad} are shown in panel B in blue, magenta and green correspondingly. Again, the thin lines represent the V_c -curves resulting from measurements along each individual slit, while the thick lines demonstrate the average profiles coming from equations (3.9)-(3.11). If information is available along two slits, then the shaded regions (paleblue for V_c^{iso} , plum for V_c^{circ} and palegreen for V_c^{rad}) show the scatter between these slits, in a case when profiles are measured along one slit only, the shaded regions indicate the measurements errors of $\sigma_p(R)$. The circular speed profiles derived from Chandra data are overplotted with errorbars in black. Stellar contribution to the circular velocity derived for the Salpeter and Kroupa IMF is shown in yellow (see Section 3.3.6).

3.3.5 Comments on individual galaxies.

- NGC0708

NGC 0708 (Figure 3.6, upper left corner) is a cD galaxy located at the center of Abell 262 galaxy cluster. The surface brightness and the projected velocity dispersion profiles are available for two slit positions oriented at P.A. = -4° and at P.A. = 215° . The surface brightness profile along the slit at P.A. = -4° declines very slowly, the logarithmic slope $\alpha = -d \ln I(R)/d \ln R$ does not exceed 1.5 in observed range of radii leading to a diverging total stellar mass. Such a behaviour may be a result of influence of cluster gravitational potential. So for our analysis we use information along the slit at P.A. = 215° only. The projected velocity dispersion is close to being flat at $R \lesssim 30''$ and gets systematics affected at larger radii. So we use the simplified version of the analysis. Results of our analysis are presented in the upper left corner of Figure 3.6. The surface brightness slope (for the slit at P.A. = 215°) is shown in panel A, derived circular velocity profiles different types of orbits are plotted in panel B. The shaded areas indicate uncertainties in derived V_c^{iso} (paleblue), V_c^{circ} (plum) and V_c^{rad} (palegreen), coming from measurement errors of $\sigma_p(R)$. The sweet radius where the sensitivity of the method to the anisotropy is minimal is located at $63''$, i.e slightly beyond the range of radii where optical data are available. Although the reliability of such the estimate is unclear the extrapolated V_c^{iso} lies quiet close to the circular speed curve derived from X-ray analysis.

- NGC1129

NGC 1129 is a giant elliptical galaxy located in the center of a poor cluster AWM 7. In Figure 3.6 (upper right) are shown results of optical and X-ray analyses. Before estimating the circular speed from optical data we have excluded regions where the surface brightness profile seems to be contaminated by projection of companions. The exclusion is done on the basis of visual inspection. So we consider the surface brightness profile along the slit positioned at P.A. = 166° in radial range from $-55''$ till $41''$ and in case of P.A. = 256° slit - at $R \leq 0''$. The projected velocity dispersion profile looks nearly flat at $R \lesssim 20''$ and is getting noisy at $R \gtrsim 20''$, so we assume $\sigma_p(R) \equiv \text{const} = 257 \text{ km s}^{-1}$ (the surface brigness weighted average value). Optical V_c^{iso} -estimate in the sweet region (which is coincident with a range of radii where $\alpha \approx 2$) is consistent with the circular speed derived from hydrostatic equilibrium of hot gas in the galaxy. Moreover, V_c^{iso} and V_c^X agree within errorbars over the range of radii where both optical and X-ray data are available. It should be noted that NGC1129 shows significant minor axis rotation, indicating a triaxial intrinsic shape of the galaxy.

- NGC1550

NGC 1550 is a S0 galaxy lying at the center of a luminous galaxy group. The surface brightness and the projected velocity dispersion profiles are available for two slit positions oriented at P.A. = 116° and at P.A. = 206° . Rotation velocity is

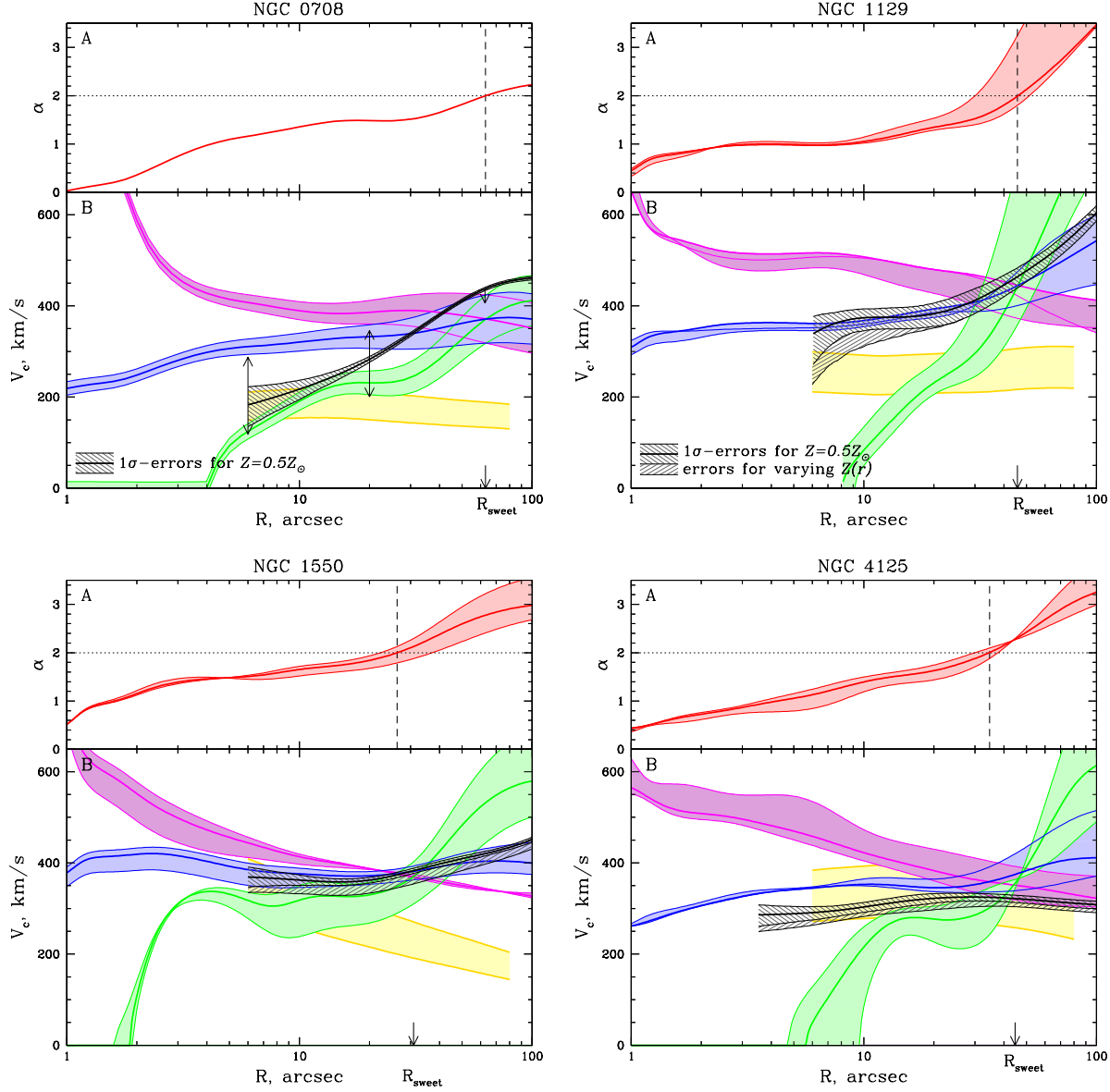


Figure 3.6: Panel A - the surface brightness slope $\alpha = d \ln I(R) / d \ln R$. Panel B - circular velocity profiles for isotropic (blue lines and paleblue shaded area), pure radial (green lines and palegreen shaded area) and pure circular (magenta lines and plum shaded area) orbits. The $V_c(R)$ derived from Chandra data under the assumption of hydrostatic equilibrium is shown as the black thick line. The shaded area shows statistical errorbars for the flat and varying with radius metallicity. For NGC 708 arrows are the same as in Figure 3.5 and indicate the conservative lower and upper limits on X-ray circular speed coming from radial variations of metal abundance. The right arrow (the shortest one) is located at the optical sweet radius. The stellar contribution to the circular speed profile is presented in yellow (see Section 3.3.6). Location of $R_{\text{eff}}^{\text{slit}}$ defined from the de Vaucouleurs fit to the long-slit surface brightness profile is marked with the dotted line.

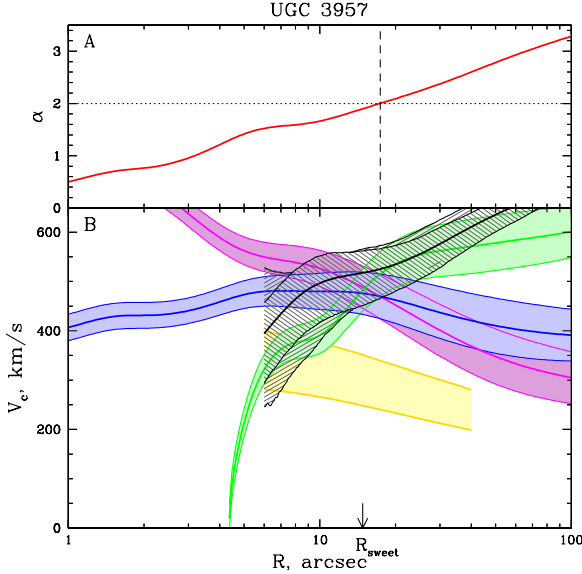


Figure 3.6: (continue)

consistent with zero. The profiles do not have any peculiar features so we use all available information to estimate the circular speed. The results of our analysis are shown in Figure 3.6, left side of a middle panel. Note that the circular velocity corresponding to the isotropic distribution of stellar orbits is nearly constant over the whole available range of radii and it coincides within errorbars with the X-ray circular speed profile. This fact could indicate that the gravitational potential of NGC 1550 is close to isothermal and the galaxy is dynamically relaxed with hot gas being in hydrostatic equilibrium.

- NGC4125

NGC4125 (Figure 3.6, middle right side) is a E6 galaxy located at the center of NGC 4125 group of galaxies. It is the only galaxy in our sample with significant rotation. To take the rotation into account we use $V_{\text{rms}}(R) = \sqrt{\sigma_p(R)^2 + V_{\text{rot}}(R)^2}$ instead of $\sigma_p(R)$ in equations (3.4). The isotropic circular speed V_c^{iso} slightly exceeds V_c^X over the whole range of radii where the optical observations are available what may indicate the non-thermal pressure support at the level of $f_{nt} \approx 36\%$ at the sweet point.

- UGC3957

UGC3957 (Figure 3.6, lower panel) is an elliptical galaxy at the center of UGC 03957 group. It has been observed using only one slit positioned at P.A. = 287°. As in case with NGC 0708 shaded areas indicate uncertainties in derived V_c -profiles, arising from measurement errors of $\sigma_p(R)$. At the sweet point V_c -estimate from optical data agrees with X-ray derived one. The discrepancy between optical $V_c(R)$ and X-ray

$V_c^X(R)$ may indicate that at $r \gtrsim 20''$ anisotropy parameter $\beta > 0$ if the hydrostatic equilibrium approximation is valid.

3.3.6 Stellar populations: properties, mass-to-light ratios, contributions to the total mass

By using the same SCORPIO/BTA long-slit spectral data, we have calculated Lick indices H β , Mgb, Fe5270, and Fe5335 along the slit, to derive the ages and chemical abundances which are in turn used to estimate mass-to-light ratios of the stellar component varying along the radius and to calculate properly the mass contributed by the stellar component within the radius R_{sweet} . Our approach to the Lick index calibrations can be found in Baes et al. (2007).

Our spectral data are rather deep and have provided the profiles of high-precision Lick indices up to 1.1–2.2 effective radii from the center in four galaxies of five. Figure 3.7 presents the comparison of the major-axis Lick index profiles in NGC 4125 according to our measurements with those by Pu et al. (2010) obtained at the 9.2m Hobby-Eberly telescope. The agreement is rather good, and the index point-to-point scatters are comparable. Figure 3.8 compares our data for NGC 708 with the data from Wegner et al. (2012) at two slit positions (we don't compare H β measurements near the center because we have not been able to correct them properly for the emission contamination). This time our data are much more precise, and the Lick index profiles are much more extended than the data by Wegner et al. (2012) obtained at the 2.4m Hiltner Telescope.

We have confronted our Lick index measurements along the radii in the galaxies under consideration to the Simple Stellar Population (SSP) models by Thomas et al. (2003) which allow to vary magnesium-to-iron ratio. Indeed, giant elliptical galaxies are known to be magnesium-overabundant (Trager et al., 2000) so it must be taken into account when age diagnostics are applied. By confronting $\langle \text{Fe} \rangle \equiv (\text{Fe5270} + \text{Fe5335})/2$ vs Mgb, we have found that indeed in four galaxies $[\text{Mg}/\text{Fe}] = +0.3$ being constant along the radius, while only in NGC 4125 $[\text{Mg}/\text{Fe}] = +0.1$ with slightly different behaviour along the major and the minor axes: in the latter cross-section, at large radii the $[\text{Mg}/\text{Fe}]$ comes to $+0.3$. This difference, together with the fast rotation along the major axis, gives an evidence for an embedded stellar disc in NGC 4125; so we would prefer to give more weight to the stellar mass-to-light ratio profile along the minor axis (see below). The estimates of the SSP-equivalent (mean, star luminosity-weighted) ages made by confronting the H β index to the complex metal-line index $[\text{Mg}/\text{Fe}]$ indicate mostly old stellar population, older than 8 Gyr, beyond the very centers of the galaxies; however the stellar nuclei of UGC 3957, NGC 1129, and NGC 1550 may be as young as 5 Gyr old (in NGC 708 we cannot estimate the age of the nuclear stellar population because of the very strong gaseous emission contaminating the H β index).

Figure 3.9 presents the metallicity radial variations in five ellipticals. The metallicity values $[\text{Z}/\text{H}]$ are plotted against normalized radius, R/R_{eff} , taking into account different values of R_{eff} along the major and the minor axes. The centers of all galaxies demonstrate

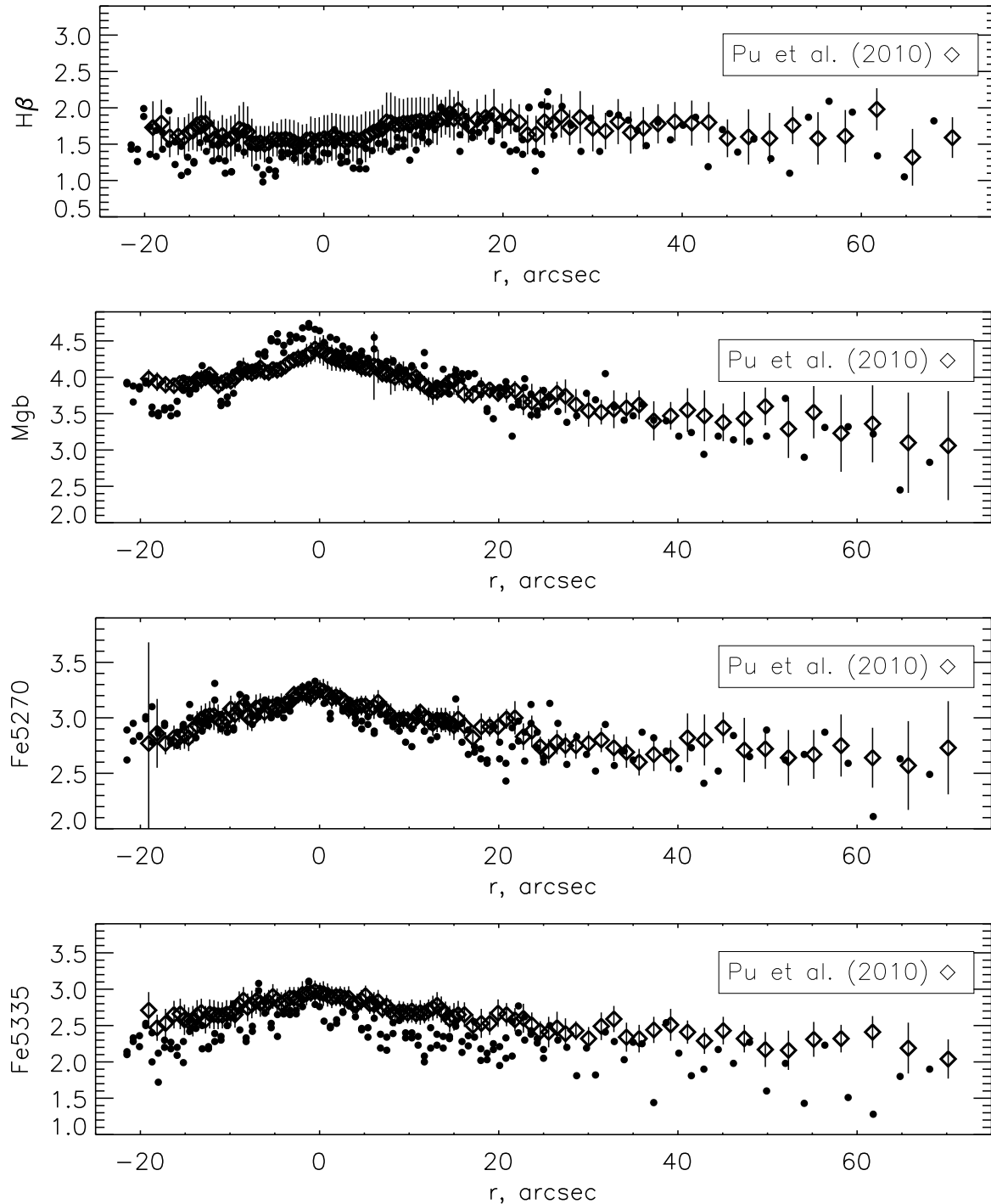


Figure 3.7: The comparison of the Lick index profiles along the major axis in NGC 4125, according to our data and to the data by Pu et al. (2010).

Table 3.4: Metallicity gradient within and beyond the half effective radius.

Galaxy	$\Delta[\text{Z}/\text{H}]/\Delta \log R$, dex per dex ($R < 0.5R_{\text{eff}}$)	$\Delta[\text{Z}/\text{H}]/\Delta \log R$, dex per dex ($R > 0.5R_{\text{eff}}$)
NGC 0708 maj. axis	-0.74 ± 0.07	0?
NGC 0708 $PA = -4$	-0.45 ± 0.11	0?
NGC 1129 maj. axis	-0.41 ± 0.07	the same?
NGC 1129 min. axis	-0.50 ± 0.15	the same?
NGC 1550 min. axis	-0.69 ± 0.04	the same?
NGC 4125 min. axis	-0.52 ± 0.05	-0.27 ± 0.18
UGC 3957	—	-2.07 ± 0.33

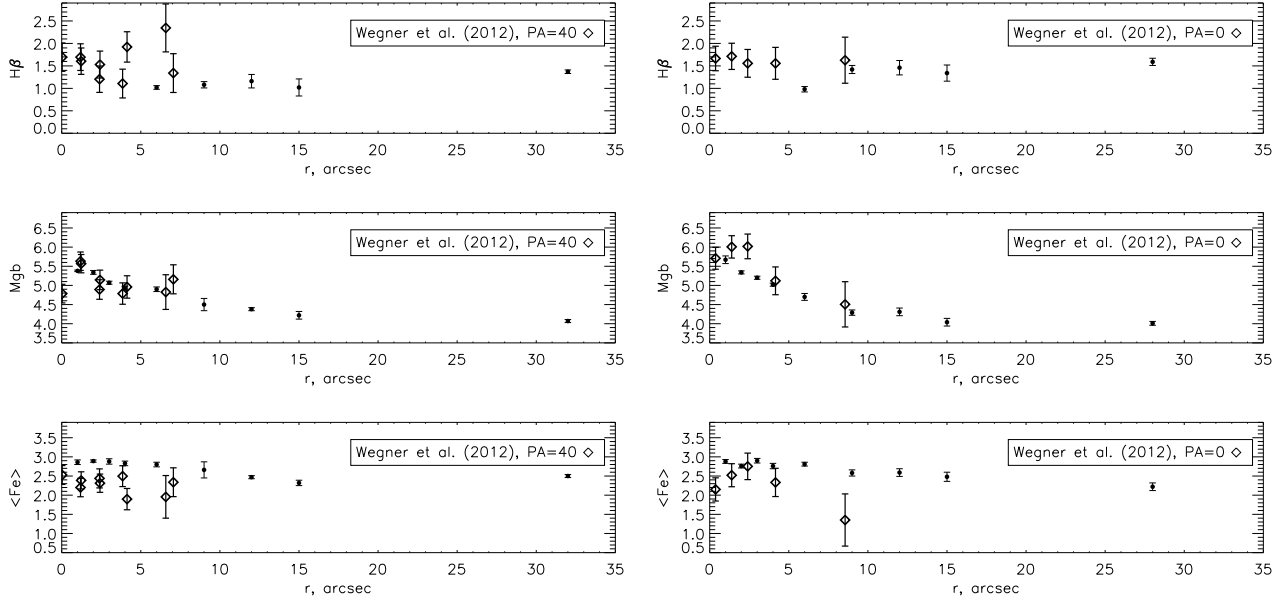


Figure 3.8: The comparison of the Lick index profiles in NGC 708, according to our data and to the data by Wegner et al. (2012), in two slit orientation.

supersolar metallicity, which is even beyond the model grid of Thomas et al. (2003) in the most massive and luminous galaxy, UGC 3957; however in the outer parts the stellar metallicity drops below the solar value everywhere. The metallicity gradients in our sample ellipticals are negative and can be estimated mostly as from -0.4 to -0.7 dex per dex. In NGC 4125 and NGC 1550 the outer metallicity profiles along the major axes go on above the minor-axis profiles that reveals once more the probable presence of the discs aligned with the major axes, formed in some dissipative events including heavy-element enrichment. We have estimated the metallicity gradients in the spheroids within $0.5R_{\text{eff}}$, $R < 0.5R_{\text{eff}}$ and beyond $0.5R_{\text{eff}}$, $R > 0.5R_{\text{eff}}$ (Table 3.4), because earlier we have found breaks of the metallicity gradients just near this radius in another sample of elliptical galaxies studied with the long-slit spectroscopy of the SCORPIO/BTA (Baes et al., 2007). Now we have found breaks between steep metallicity gradients and nearly zero ones at $0.5R_{\text{eff}}$ in two galaxies having the lower mass – in NGC 0708 and NGC 4125. In massive NGC 1129, NGC 1550, and UGC 3957 the outer metallicity gradients look as steep as the inner ones. Perhaps, for these galaxies we have not reached the radius of break because in the central Coma cluster galaxy NGC 4889 the metallicity gradient break is found at $R = 1.2R_{\text{eff}}$ (Coccato et al., 2010); perhaps the position of break radius correlates with the mass of a galaxy. However, the inner metallicity gradients in our galaxies (and the outer one in UGC 3957) are all steeper than -0.3 dex per dex; it means that these inner parts of the elliptical galaxies under consideration could not be formed by major merger (Kobayashi, 2004).

Radial variations of the stellar population mass-to-light ratio in this case reflect mostly the variations of the metallicity. We have calculated $M/L(V)(R)$ in every galaxy by using

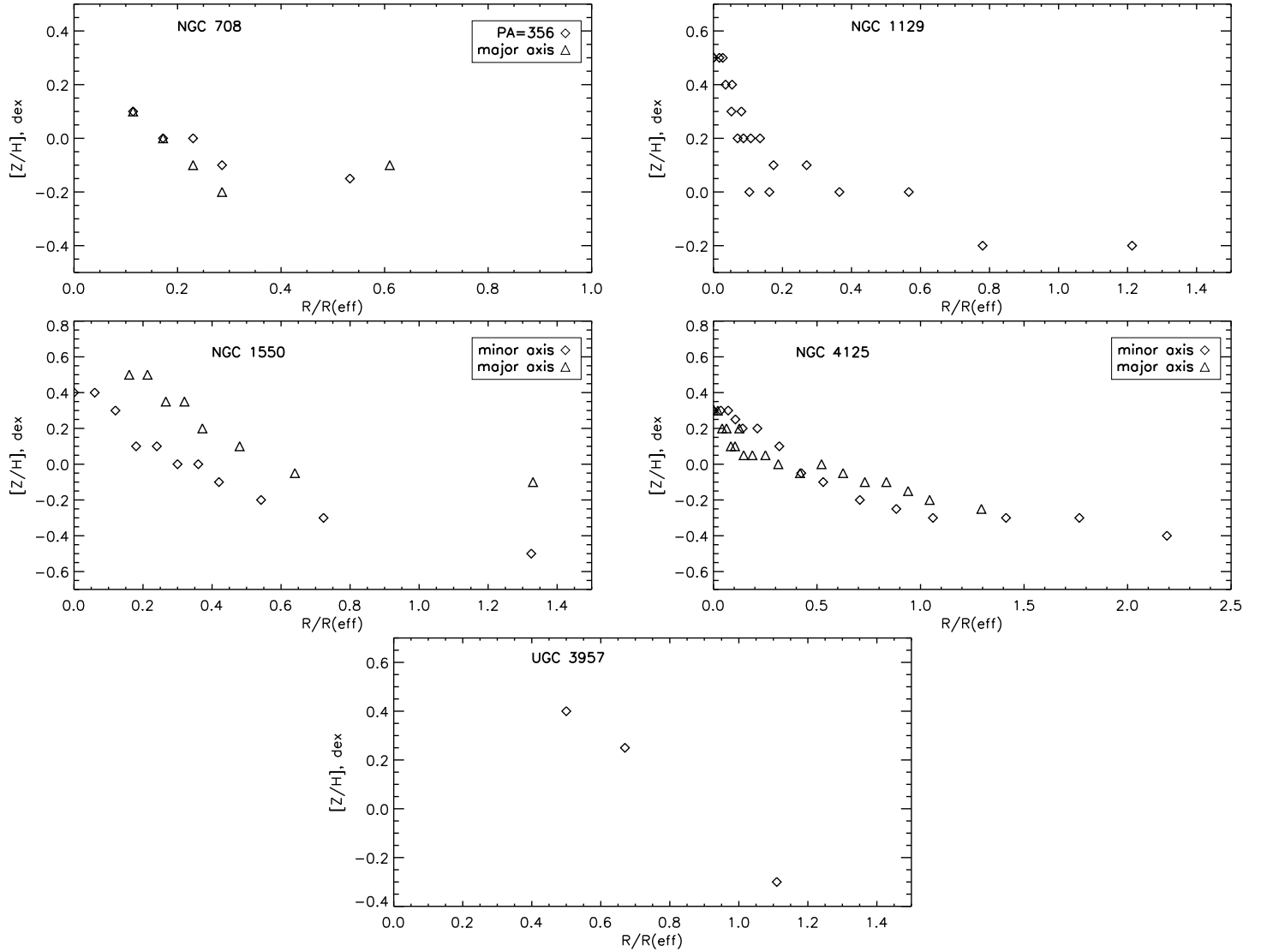


Figure 3.9: The radial variations of the stellar population metallicity along the radius in five elliptical galaxies under consideration; in NGC 1129 both cross-sections are united since they give coincident dependencies.

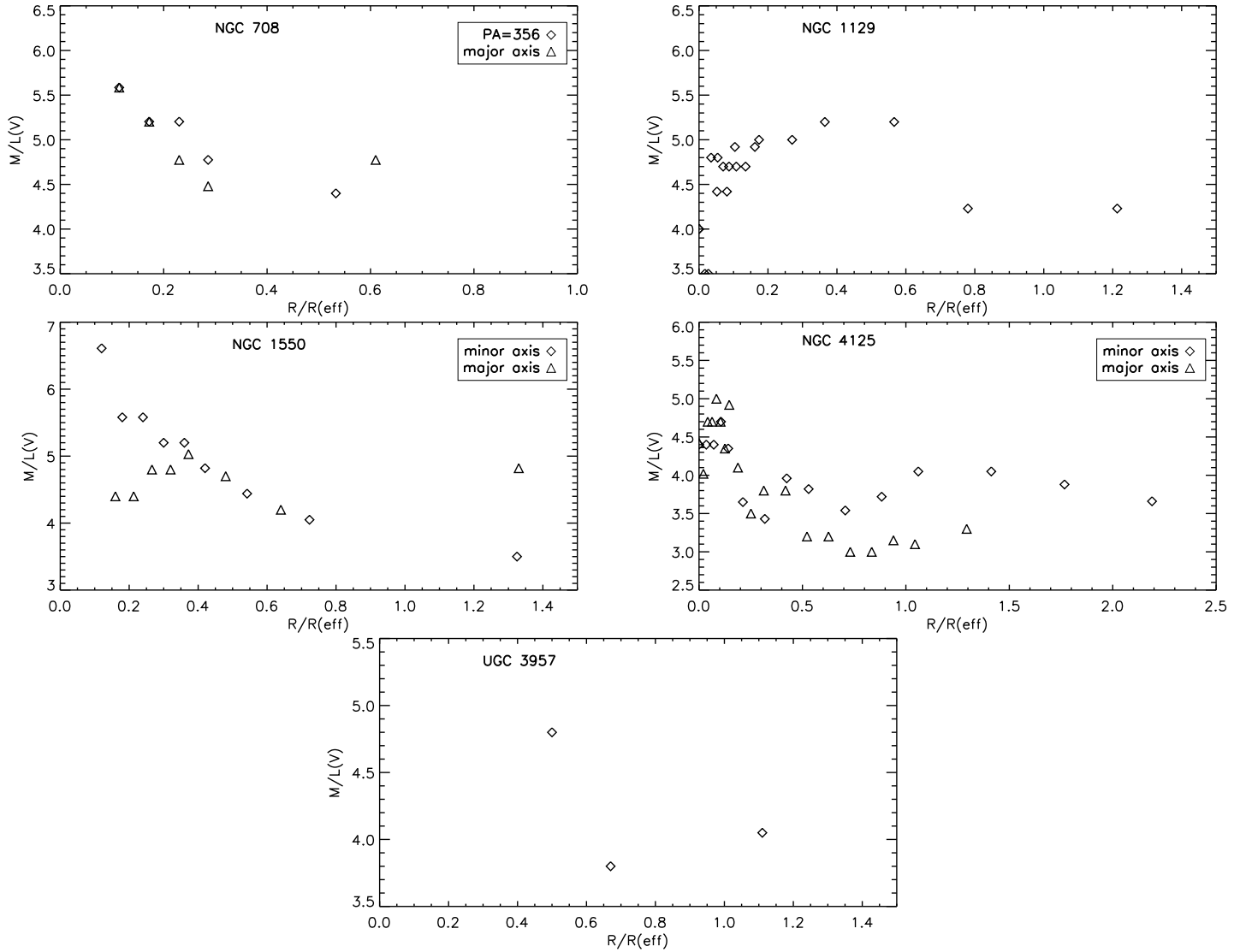


Figure 3.10: The variations of the stellar population mass-to-light ratios along the radius in five elliptical galaxies under consideration; in NGC 1129 both cross-sections are united since they give coincident dependencies.

Table 3.5: Stellar masses and the fraction of dark matter (DM) within R_{sweet} for Kroupa (K) and Salpeter (S) IMF.

Galaxy	V_c (K), km s $^{-1}$	% of DM	V_c (S), km s $^{-1}$	% of DM
NGC 0708	133	87	188	74
NGC 1129	215	76	303	54
NGC 1550	190	75	268	51
NGC 4125	256	53	361	7
UGC 3957	244	74	344	48

the recent model grid BASTI by Percival et al. (2009); the [Mg/Fe], [Z/H], and ages found from the Lick indices above have been substituted into the BASTI tables. The radial profile of $M/L(V)$ for every galaxy is shown in Figure 3.10. The models BASTI are calculated for the Kroupa IMF; if we prefer the classic Salpeter one, all the $M/L(V)$ values should be increased by a factor of 2 (Bell et al., 2003).

We have approximated the profiles of Figure 3.10 by smooth logarithmic curves and have used the dependencies derived to transform the surface brightness profiles (this time, the surface brightness profiles obtained from the isophote analysis, with the corresponding azimuthally averaged values of R_{eff}) into surface mass density profiles (Figure 3.11). Our aim was to estimate, though under very simple assumptions, the stellar mass which is contained within the radii R_{sweet} , to compare it with the dynamical masses derived in previous subsections. The profiles of Figure 3.11 were then deprojected with the formulae invented by Kholopov (1949), and after that we have integrated the volume mass density profiles up to R_{sweet} under the assumption of spherical symmetry. It is obvious that the assumption of spherical symmetry is very rude for our objects, especially for NGC 708 and NGC 4125, and the fact that the surface mass density profiles are not going to infinity but are cut at arbitrary radii provides only lower limits of the stellar mass estimates, however some feeling of the dark matter fraction within the optical borders of the giant elliptical galaxies can be obtained.

As we can see in Table 3.5, there is a range of dark mass presence among our small sample. In particular, NGC 4125 may hold all its dynamical mass mainly in stars. However, if we refer to the Salpeter IMF, a typical fraction of dark matter within R_{sweet} is $\sim 50\%$. For the Kroupa IMF the sample averaged fraction is $\sim 70\%$.

3.4 Discussion

We discuss one simple and fast, but nevertheless reliable method for estimating masses of early-type galaxies from the stellar surface brightness and the line-of-sight velocity dispersion profiles only. The method is based on the ansatz that the relation between the projected velocity dispersion and the circular speed is almost insensitive to the anisotropy of stellar orbits at a characteristic radius R_{sweet} where derived circular speed profiles for isotropic distribution of stars, pure circular and pure radial stellar orbits are close to each

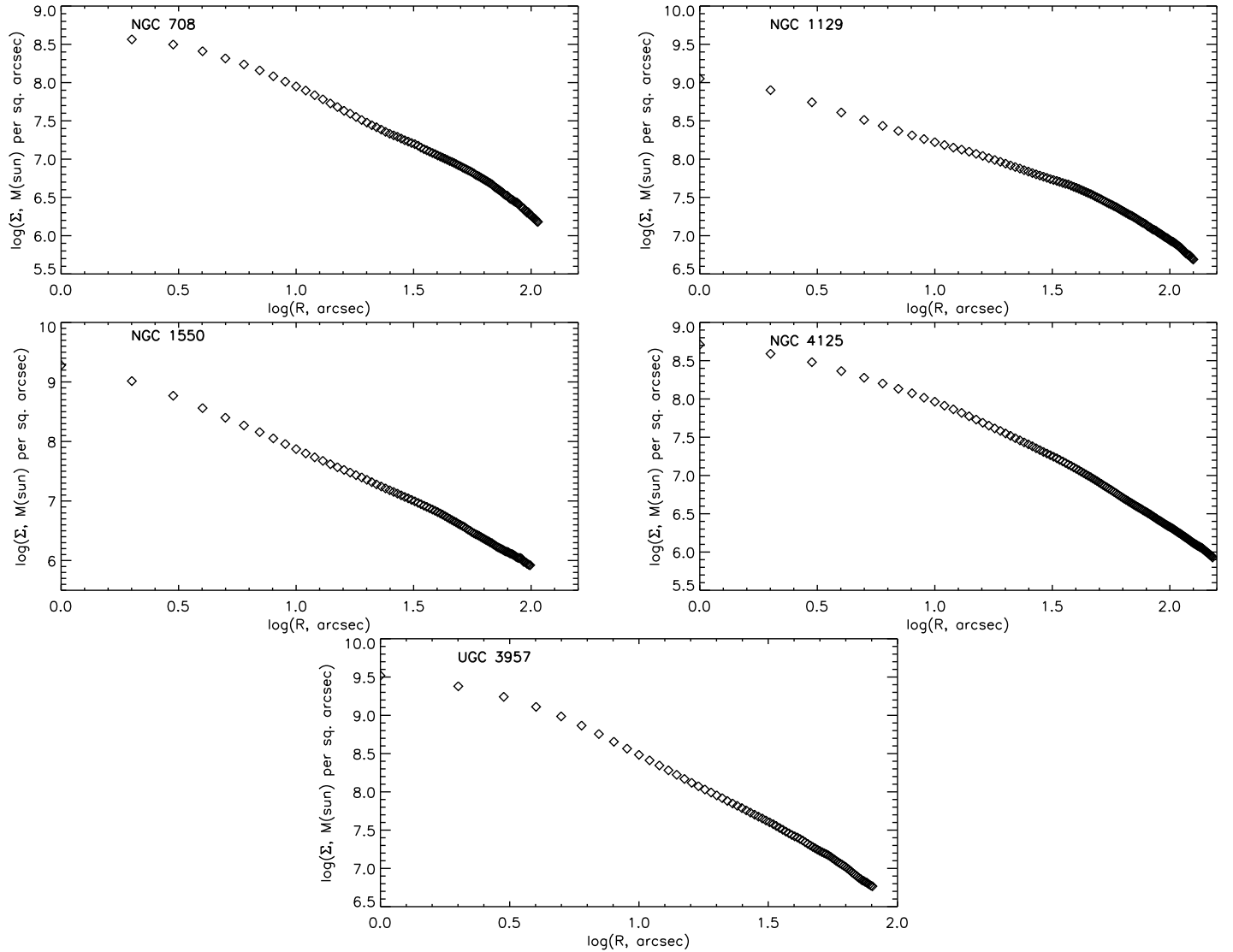


Figure 3.11: The radial profiles of the surface **mass** density along the radius in five elliptical galaxies under consideration.

Table 3.6: Ellipticity and effective radius for the sample galaxies. The columns are: (1) - galaxy name; (2) - ellipticity; (3) - effective radius defined from the de Vaucouleurs fit to the ellipse-averaged surface brightness profile; (4) - effective radius defined from the de Vaucouleurs fit to the average surface brightness profile (eq. 3.9).

Name (1)	Ellipticity (2)	R_{eff} , arcsec (3)	$R_{\text{eff}}^{\text{av}}$, arcsecc (4)
NGC 708	0.45	63.5 ± 1.5	49.6
NGC 1129	0.22	86.7 ± 2.4	77.6
NGC 1550	0.11	25.7 ± 0.7	17.5
NGC 4125	0.46	56.4 ± 0.4	38.8
UGC 3957	0.1	33.9 ± 0.8	14.4

other. R_{sweet} lies close to the radius R_2 where the surface brightness $I(R)$ declines as R^{-2} , which is in turn not far from the effective radius of the galaxy R_{eff} . Although the method allows to estimate mass within some particular radius only (or in radial range where $I(R) \propto R^{-2}$), it does not require any apriori parametrization of mass or anisotropy profiles and the resulting estimate does not depend significantly on the quality of data. The method has already been tested on a sample of 65 simulated galaxies drawn from cosmological simulations by Oser et al. (2010) in Lyskova et al. (2012). When averaged over the subsample of massive ($\sigma_p(R_{\text{eff}}) > 150 \text{ km s}^{-1}$) slowly rotating galaxies the recovered circular speed is almost unbiased ($\overline{\Delta_{\text{opt}}} < 1\%$) with modest scatter (RMS = 5.4 %). Note that in Lyskova et al. (2012) the surface brightness and the line-of-sight velocity dispersion profiles were calculated in a set of logarithmic concentric annuli around the center of the simulated galaxy. In this paper we (i) mimic the long-slit observations by computing the profiles along the slits, and also (ii) extend our analysis to rotating elliptical galaxies by considering $V_{\text{rms}}(R) = \sqrt{\sigma_p^2(R) + V_{\text{rot}}^2(R)}$ instead of $\sigma_p(R)$ in equations (3.4) or (3.6), where $V_{\text{rot}}(R)$ is the observed rotational velocity. Tests have been performed on the sample of massive simulated galaxies ($\sigma_p(R_{\text{eff}}) > 150 \text{ km s}^{-1}$, edge-on view) that includes both fast and slow rotators in proportion close to the observed one reported by ATLAS^{3d} team (Emsellem et al., 2007). We find that the circular speed recovered from $I(R)$ and $\sigma_p(R)$ measured along the slit aligned with the apparent major axis of the galaxy is on average underestimated by 4 – 5% and the RMS-scatter is about 6%. The bias almost vanishes when $\sigma_p(R)$ in equations (3.4) is substituted with $V_{\text{rms}}(R) = \sqrt{\sigma_p^2(R) + V_{\text{rot}}^2(R)}$ and the RMS-scatter remains the same. If profiles are measured along apparent major and minor axes of the galaxy then we can reduce the scatter arising from triaxiality of elliptical galaxies. Indeed, in this case the RMS-scatter is reduced down to 5%.

X-ray circular speed profiles for all galaxies are inferred under an assumption of constant metallicity ($Z = 0.5Z_{\odot}$), although the errorbars are estimated in a conservative way, allowing for the abundance gradients. If the abundance steadily increases to the galaxy center, then the assumption of the flat metallicity profile would lead to overestimated

circular velocity. The decreasing at small radii abundance would imply instead that V_c^X is underestimated. Abundance measurements for low temperature ($\lesssim 1.5$ keV) systems remains among the most important uncertainties in X-ray determination of the circular speed of elliptical galaxies. For hotter systems the impact of abundance is much less severe. For instance, the conservative estimate for NGC0708 suggests that the circular speed may be over-/underestimated as much as 25-30 % (at $R \lesssim 30 - 40''$).

The inferred circular speed estimates from optical data and from X-ray for all galaxies in our sample agree with each other remarkably well, especially for NGC 1550 and NGC 1129, indicating the relaxed dynamical state of these galaxies, close to isotropic distribution of stellar orbits within 1-2 effective radii and that hot gas in these objects is in the hydrostatic equilibrium. The only rotating galaxy in our sample, NGC 4125, is also the only galaxy with non-negligible nonthermal pressure support (at the level of $\approx 36\%$). For UGC 3957 both X-ray and optical methods give the same (within errorbars) result at the sweet point and at larger radii we observe that $V_c^X(R) > V_c^{\text{iso}}(R)$ what may be interpreted as the radially biased stellar velocity anisotropy. NGC 708 is the most difficult galaxy for interpretation. At $R \lesssim 30''$ where optical data are quite reliable $V_c^X(R)$ lies below $V_c^{\text{iso}}(R)$. Then at $30'' \gtrsim R \gtrsim 60''$ these two curves are roughly consistent with each other. At the sweet spot which is located slightly beyond the radial range with available optical data the X-ray mass estimate exceeds the optical one by $\sim 40\%$ although the reliability of the V_c^{iso} at this radius is under question and errorbars are quite large. The average ratio between the optical V_c^{iso} and V_c^X at the sweet spot is equal to 0.98 with ≈ 0.11 rms-scatter⁵. Given the scatter, this result indicates that on average the non-thermal contribution to the total gas pressure is consistent with zero. Two galaxies - NGC 4125 and NGC 0708 - that have the lowest central velocity dispersions and are showing the largest deviation of $\left\langle \frac{V_c^{\text{iso}}}{V_c^X} \right\rangle$ from the mean value, appear to be especially prone to abundance uncertainties in X-ray analysis. Low temperature of NGC 4125 ($T \approx 0.5$ keV) does not allow to disentangle reliably continuum and emission lines. In its turn, NGC 0708 has higher temperature at the sweet radius (≈ 1.7 keV) but shows significant abundance gradients, what leads to large spread in the resulting circular velocity curves. If we exclude these two galaxies, then the average ratio is $\left\langle \frac{V_c^{\text{iso}}}{V_c^X} \right\rangle \approx 0.96$ with $RMS \approx 0.03$. This scatter is comparable to the expected value of 5.4% coming from the analysis of a sample of simulated massive elliptical galaxies without significant rotation (Lyskova et al. 2012).

It should be mentioned that for our analysis we deliberately use the surface brightness profiles measured along the slit rather than ellipse-averaged radial profiles. On one hand, $I(R)$ along specific PA could be affected by local inhomogeneities in brightness and the signal-to-noise ratio is smaller compared to azimuthally-averaged profiles. On the other hand, analysing the projected velocity dispersion and surface brightness profiles measured in the same way seems to be more self-consistent and justified. Moreover, we aim to

$${}^5\bar{x} = \frac{\sum x}{N} \pm \frac{RMS}{\sqrt{N}}, RMS = \sqrt{\frac{\sum (x-\bar{x})^2}{N}}$$

demonstrate performance of our simple mass estimator using the most basic observables, thus on purpose neglecting all possible complications. Apart from using the original surface brightness distribution along the specific PA, we also simplify the analysis by neglecting departures from spherical symmetry (see eq. 3.9-3.11). If we take into account information on ellipse-averaged radial profiles and ellipticity of a given galaxy, we will get the V_c -estimate similar to the reported one (within errorbars), although the averaged surface profiles are slightly shallower than original ones pushing R_{sweet} towards larger radii where kinematics is getting less reliable.

The full version of analysis, i.e. equations (3.4), is recommended to use when the projected velocity dispersion profile is reliable over the radial range of interest. As the circular speed $V_c^{\text{rad}}(R)$ recovered for pure radial orbits depends on the second derivative $\delta = \frac{d^2 \ln[I(R)\sigma_p^2(R)]}{d(\ln R)^2}$, it relies on the quality of $\sigma_p(R)$. If the dispersion profile is noisy and does not decline steeply, then R_2 - the radius where $\alpha = d \ln I(R) / d \ln R = 2$ - can be used as the sweet spot. For our sample of galaxies the average ratio $\left\langle \frac{V_c^{\text{iso}}(R_{\text{sweet}})}{V_c^{\text{iso}}(R_2)} \right\rangle$ of circular speed estimates calculated from equations (3.4) at R_{sweet} and at R_2 is equal to 1.03 with $RMS = 0.022$. When the observational data do not allow to use the full analysis, then the circular speed can be estimated using the simplified analysis (eq. 3.6). The average ratio $\left\langle \frac{V_c^{\text{iso}}(R_{\text{sweet}})}{V_c^{\text{iso},s}(R_2)} \right\rangle$ equals to 1.05 with $RMS = 0.022$, where $V_c^{\text{iso},s}$ is calculated using equations (3.6).

As expected the sweet radius is found to lie close to R_2 and also not too far from the effective radius R_{eff} of a galaxy (effective radii used here, R_{eff}^{av} , are listed in Table 3.6). For our sample the average ratio $\left\langle \frac{R_{\text{sweet}}}{R_2} \right\rangle \approx 1.14$ with rms-scatter $RMS \approx 16\%$, while $\left\langle \frac{R_{\text{sweet}}}{R_{\text{eff}}^{av}} \right\rangle \approx 1.23$ with $RMS \approx 30\%$ scatter. It should be noted that the value of the effective radius strongly depends on a measurement technique. R_{eff} could vary significantly depending on (i) whether it is measured with or without extrapolation of data, (ii) parametric form of the stellar distribution profile used to fit the data, (iii) radial range used to fit, for instance, the Sérsic profile, (iv) quality of photometric data (see, e.g., Kormendy et al., 2009; Cappellari et al., 2013). In contrast with the simple mass estimator proposed by (Wolf et al., 2010) our estimator is not tied to the effective radius. The sweet spot is defined from *local* properties of $I(R)$ and $\sigma_p(R)$ or even from $I(R)$ alone.

3.5 Conclusion

We discuss a simple mass estimator that allows one to estimate the circular speed V_c from *local* properties of the surface brightness and the line-of-sight kinematics at a characteristic radius where the V_c -estimate is largely insensitive to the unknown anisotropy of stellar orbits. Although the method is designed for non-rotating spherical galaxies, we extend it

also to mildly rotating axisymmetric and slowly-rotating triaxial ones, substituting $\sigma_p(R)$ in equation 3.4 or 3.6 with $V_{\text{rms}}(R) = \sqrt{\sigma_p^2(R) + V_{\text{rot}}^2(R)}$, where $V_{\text{rot}}(R)$ is the rotational velocity. Tests on the sample of massive simulated galaxies show that the recovered from $I(R)$ and $\sigma_p(R)$ measured along apparent major and minor axes of the galaxy circular speed is almost unbiased with the RMS-scatter of $\sim 5\%$.

We apply the method to M87 and compare our simple mass estimate with circular speed profiles derived from X-rays and the state-of-the-art Schwarzschild modeling, thus revisiting the results of Churazov et al. (2008, 2010). At the sweet radius $R_{\text{sweet}} = 115''$ we derive $V_c^{\text{opt}} = 511 \text{ km s}^{-1}$, that agrees well with the circular speed obtained in Murphy et al. (2011). After comparing the optical V_c -estimate with the X-ray derived one, we conclude that at the sweet radius the non-thermal contribution to the total gas pressure is $\sim 20\%$. The true value of the non-thermal contribution in M87 could be even lower, since X-ray data near the sweet radius are affected by the shock (Forman et al., 2007).

We observe a sample of five X-ray bright elliptical galaxies with the 6-m telescope of the SAO RAS and measure the surface brightness, line-of-sight velocity and velocity dispersion distribution of stars up to two effective radii along one or two slits. We apply our simple method to estimate the circular speed and compare it with the circular speed measurements based on the X-ray analysis of Chandra data. We conclude that optical and X-ray V_c -estimates agree with each other remarkably well implying the sample averaged non-thermal pressure support of $\sim 4\% \pm 20\%$, i.e. to be consistent with zero.

From deep long-slit spectral data obtained with SCORPIO/BTA we derive high-precision Lick indices profiles out to ~ 2 effective radii, which in turn used to estimate the radial variations of the stellar population mass-to-light ratios and the dark matter fraction within R_{sweet} , typical value of the latter is $\sim 50\%$ for the Salpeter IMF and $\sim 70\%$ for the Kroupa IMF.

3.6 Acknowledgments

NL is grateful to the International Max Planck Research School on Astrophysics (IMPRS) for financial support. NL acknowledges helpful discussions with Scott Tremaine and Thorsten Naab. This research has made use of the NED which is operated by the Jet Propulsion Laboratory, California Institute of Technology, under contract with the National Aeronautics and Space Administration. This work was partly supported by the Research Program OFN-17 of the Division of Physics, Russian Academy of Sciences. AM is also grateful for the financial support of the ‘Dynasty’ Foundation. We thank Azamat Valeev, Timur Fatkhullin and Alexander Vinokurov for supporting the SCORPIO observations, and especially Victor Afanasiev for his great contribution to spectroscopy at the 6 m telescope.

Bibliography

- Afanasiev V. L., Moiseev A. V. 2005, Astron. Letters, 31, 194
- Afanasiev V. L., Moiseev A. V. 2011, Baltic Astronomy, 20, 363
- Anders E., Grevesse N. 1989, Geochim. Cosmochim. Acta, 53, 197
- Arnaud K. A. 1996, Astronomical Data Analysis Software and Systems V, 101, 17
- Baes M., Sil'chenko O. K., Moiseev A. V., Manakova E. A. 2007, A& A, 467, 991
- Bell E. F., McIntosh D. H., Katz N., Weinberg M. D. 2003, ApJ Suppl Ser, 149, 289
- Buote D. A. 2000, MNRAS, 311, 176
- Buote D. A., Humphrey P. J. 2012, in Kim D.-W., Pellegrini S., eds, Astrophysics Space Science Library Vol. 378, Hot Interstellar Matter in Elliptical Galaxies. Springer, Berlin, p. 235
- Buote D. A., Humphrey P. J. 2012, MNRAS, 421, 1399
- Cappellari M. et al. 2013, MNRAS, 432, 1709 (Paper XV)
- Churazov E., Forman W., Jones C., Böhringer H. 2003, ApJ, 590, 225
- Churazov E., Forman W., Vikhlinin A., Tremaine S., Gerhard O., Jones C. 2008, MNRAS, 388, 1062
- Churazov E., Tremaine S., Forman W., Gerhard O., Das P., Vikhlinin A., Jones C., Böhringer H., Gebhardt K. 2010, MNRAS, 404, 1165
- Coccato L., Gerhard O., Arnaboldi M. 2010, MNRAS Letters, 407, L26
- Côté P., McLaughlin D.E., Hanes D.A., Bridges T.J., Geisler D., Merritt D., Hesser J.E., Harris G.L.H., Lee M.G. 2001, ApJ, 559, 828
- de Lucia G., Blaizot J. 2007, MNRAS, 375, 2
- Dickey J. M., Lockman F. J. 1990, ARAA, 28, 215

- Emsellem E., Cappellari M., Peletier R. F., McDermid R. M., Bacon R., Bureau M., Copin Y., Davies R. L., Krajnović D., Kuntschner H., Miller B.W., de Zeeuw P.T. 2004, MNRAS, 352, 721
- Emsellem E., Cappellari M., Krajnović D., van de Ven G., Bacon R., Bureau M., Davies R. L., de Zeeuw P. T., Falcón-Barroso J., Kuntschner H., McDermid R., Peletier R. F., Sarzi M. 2007, MNRAS, 379, 401
- Emsellem E., Cappellari M., Krajnović D., Alatalo K., Blitz L., Bois M., Bournaud F., Bureau M., Davies R. L., Davis T. A., de Zeeuw P. T., Khochfar S., Kuntschner H., Lablanche P.-Y., McDermid R. M., Morganti R., Naab T., Oosterloo T., Sarzi M., Scott N., Serra P., van de Ven G., Weijmans A.-M., Young L. M. 2011, MNRAS, 414, 888
- Forman W., Jones C., Tucker W. 1985, ApJ, 293, 102
- Forman W., Jones C., Churazov E., Markevitch M., Nulsen P., Vikhlinin A., Begelman M., Böhringer H., Eilek J., Heinz S., Kraft R., Owen F., Pahre M. 2007, ApJ, 665, 1057
- Fukazawa Y., Botoya-Nonesa J. G., Pu J., Ohto A., Kawano N. 2006, AJ, 636, 698
- Gebhardt K., Richstone D., Kormendy J., Lauer T.R., Ajhar E.A., Bender R., Dressler A., Faber S. M., Grillmair C., Magorrian J., Tremaine S. 2000, AJ, 119, 1157
- Gebhardt K., Richstone D., Tremaine S., Lauer T.R., Bender R., Bower G., Dressler A., Faber S. M., Filippenko A.V., Green R., Grillmair C., Ho L.C., Kormendy J., Magorrian J., Pinkney J. 2003, ApJ, 583, 92
- Gebhardt K., Thomas J. 2009, Apj, 700, 1690
- Gerhard O.E. 1993, MNRAS, 265, 213
- Gerhard O., Kronawitter A., Saglia R. P., Bender R. 2001, AJ, 121, 1936
- Humphrey P. J., Buote D. A. 2006, ApJ 639, 136
- Johnson R., Chakrabarty D., O'Sullivan E., Raychaudhury S. 2009, ApJ, 706, 980
- Kholopov P. N. 1949, AZh, 26, 298
- Kobayashi C. 2004, MNRAS, 347, 740
- Koopmans L. V. E., Treu T., Bolton A. S., Burles S., Moustakas L. A. 2006, ApJ, 649, 599
- Kormendy J., Fisher D. B., Cornell M. E., Bender R. 2009, ApJS, 182, 216
- Lau E. T., Kravtsov A. V., Nagai D. 2009, ApJ, 705, 1129

- Lyskova N., Churazov E., Zhuravleva I., Naab T., Oser L., Gerhard O., Wu X. 2012, MNRAS 423, 1813
- Mamon G.A. and Boué G. 2010, MNRAS, 401, 2433
- McLaughlin D.E 1999, AJ, 117, 2398
- Moiseev A.V. 2001, Bull. SAO., 51, 11 (astro-ph/0111219)
- Murphy J. D., Gebhardt K., Adams J. J. 2011, ApJ, 729, 129
- Naab T., Johansson P. H., Ostriker J. P., Efstathiou G. 2007, ApJ, 658, 710
- Naab T., Oser L., Emsellem E., Cappellari M., Krajnović, McDermid R.M., Alatalo K., Bayet E., Blitz L., Bois M., Bournaud F., Bureau M., Crocker A., Davies R.L., Davis T.A., de Zeeuw P.T., Duc P.-A., Hirschmann M., Johansson P.H., Khochfar S., Kuntschner H., Morganti R., Oosterloo T., Sarzi M., Scott N., Serra P., van de Ven G., Weijmans A., Young L.M. MNRAS, submitted
- Nagai D., Vikhlinin A., Kravtsov A. V. 2007, ApJ, 655 98
- Oser L., Ostriker J.P., Naab T., Johansson P.H., Burkert A. 2010, ApJ, 725, 2312
- Percival S. M., Salaris M., Cassisi S., Pietrinferni A. 2009, ApJ, 690, 427
- Piffaretti R., Jetzer Ph., Schindler S. 2003, AA, 398, 41
- Pu S. B., Saglia R. P., Fabricius M. H., Thomas J., Bender R., Han Z. 2010, A& A, 516, A4
- Richstone D. O., Tremaine S. 1984, ApJ 286, 27
- Romanowsky A. J., Kochanek C. S. 2001, ApJ, 553, 722
- Rusli S. P., Thomas J., Erwin P., Saglia R. P., Nowak N., Bender R. 2011, MNRAS, 410, 1223
- Schwarzschild M. 1979, ApJ, 232, 236
- Shen J., Gebhardt K. 2010, ApJ, 711, 484
- Sil'chenko O. K., Moiseev A. V., & Shulga, A. P. 2010, AJ, 140, 1462
- Smith R.K., Brickhouse N.S., Liedahl D.A., Raymond J.C. 2001, ApJ, 556, L91
- Thomas D., Maraston C., Bender R. 2003, MNRAS, 339, 897
- Thomas J., Saglia R.P., Bender R., Thomas D., Gebhardt K., Magorrian J., Richstone D. 2004, MNRAS, 353, 391

- Thomas J., Saglia R.P., Bender R., Thomas D., Gebhardt K., Magorrian J., Corsini E.M., Wegner J. 2005, MNRAS, 360, 1355
- Thomas J., Jesseit R., Naab T., Saglia R. P., Burkert A., Bender R. 2007, MNRAS, 381, 1672
- Thomas J. 2010, arXiv:1007.359
- Trager S. C., Faber S. M., Worthey G., González J. J. 2000, AJ, 120, 165
- Treu T., Koopmans L. V., Bolton A. S., Burles S., Moustakas L. A. 2006, ApJ, 640, 662
- van der Marel R.P. 1994, MNRAS, 270, 271
- Vikhlinin A., Markevitch M., Murray S.S., Jones C., Forman W., Van Speybroeck L. 2005, ApJ, 628, 655
- Wegner G. A., Corsini E. M., Thomas J., Saglia R. P., Bender R., Pu S. B. 2012, AJ, 144, A78
- Wolf J., Martinez G.D., Bullock J.S., Kaplinghat M., Geha M., Muñoz R.R., Simon J.D., Avedo F.F. 2010, MNRAS, 406, 1220
- Wu X., Gerhard O., Naab T., Oser L., Martinez-Valpuesta I., Hilz M., Churazov E., Lyskova N. MNRAS, submitted
- Zhuravleva I., Churazov E., Kravtsov A., Lau E. T., Nagai D., Sunyaev R. 2013, MNRAS, 428, 3274

Chapter 4

Performance of simple mass estimators for elliptical galaxies

in prep.

N.Lyskova, E.Churazov, S. Tremaine, J. Thomas, T. Naab

Abstract. We compare performance of theoretical simple mass estimators of elliptical galaxies relying on the most basic observables, namely, the surface brightness and velocity dispersion profiles, without invoking computationally expensive detailed modeling. These methods recover the mass at a special radius where the mass estimate is expected to be almost insensitive to the anisotropy of stellar orbits. One method (Wolf et al. 2010) uses the total luminosity-weighted velocity dispersion and evaluates the mass at a deprojected half-light radius $r_{1/2}$, i.e. depends on the *global* galaxy properties. Another approach (Churazov et al. 2010) relies on the *local* properties and estimates the mass at a radius R_2 where the surface brightness declines as R^{-2} . Hereafter we refer to these two methods as ‘global’ and ‘local’ methods.

We performed tests on analytical models, simulated galaxies and real elliptical galaxies which have already been modeled by the Schwarzschild orbit-superposition technique. The tests show that both estimators recover an almost unbiased circular speed estimate (when averaged over a sample) with a modest RMS-scatter ($\lesssim 10\%$). Tests on analytical models and simulated galaxies indicate that the local estimator has a smaller RMS-scatter than the global one. We show, that the projected velocity dispersion at R_2 could serve as a good proxy for the virial galaxy mass. For simulated galaxies the total halomass scales with $\sigma_p(R_2)$ as $M_{vir} [M_\odot h^{-1}] \approx 6 \cdot 10^{12} \left(\frac{\sigma_p(R_2)}{200 \text{ km s}^{-1}} \right)^4$ with RMS-scatter $\approx 40\%$.

4.1 Introduction

Being one of the basic properties, the galaxy masses play a key role in our understanding of formation and evolution of these objects. While observations of disc rotation curves allows one to determine spiral galaxy masses directly, the situation with early-type galaxies is more problematic due to lack of mass tracers on known orbits. Approaches of different level of sophistication and generality have been developed for mass determination of elliptical galaxies. Dynamical modeling using the orbit superposition Schwarzschild method is considered to be the state-of-the-art technique that allows one to recover the galaxy gravitational potential and an orbital structure with an accuracy of $\lesssim 15\%$ (Thomas et al., 2005). Schwarzschild modeling is now widely used for mass measurements of supermassive black holes, for determination of total mass profile and its decomposition into luminous and dark matter components as well as for constraining the orbital structure. As such approach requires high quality observational data on the line-of-sight velocity moments (namely, the third and the fourth order Gauss-Hermite moments), it can be applied only to nearby galaxies. Moreover, numerical experiments show that due to intrinsic degeneracies not all the model parameters can be uniquely constrained even from the best-available integral-field stellar kinematics (e.g., van den Bosch and van de Ven, 2009).

Large astronomical surveys are extremely important for galaxy studies as they facilitate a number of statistical investigations of galaxy properties. Galaxy mass determination at different redshifts is a critical ingredient for galaxy formation studies and for tracing the assembly of galaxy mass over time. For large surveys containing information on galaxy photometry and kinematics usage of detailed dynamical modeling could be not practical/justified especially in a case of poor and/or noisy observational data. It is desirable to have simple and robust techniques based on the most basic observables that provide an unbiased mass estimate with a modest scatter.

There have been recently suggested two simple mass estimation methods (Churazov et al. 2010 and Wolf et al. 2010) which evaluate mass at a special radius from the surface brightness and projected velocity dispersion profiles without involving detailed modeling. Although these approaches allow one to recover mass at some particular radius only and do not recover the mass distribution with radius, these estimates could be used (i) to estimate non-thermal contribution to the total gas pressure when compared with X-ray mass estimate at the same radius; (ii) to derive a slope of the mass profile when combined with the mass estimate from strong lensing; (iii) as a virial mass proxy.

The central thesis of this work is to compare a performance of simple mass estimators on analytical models, simulated galaxies and real elliptical galaxies that have been already studied in detail with the state-of-the-art Schwarzschild method. The paper is organized as follows. In section 4.2, we provide a brief description of the simple mass estimators. We present results of the tests of these methods on analytical models and a sample of simulated galaxies in section 4.3 and on real elliptical galaxies - in section 4.4. A possibility to use simple estimates as a proxy for a virial mass is discussed in section 4.5. A summary on the bias and accuracy of the methods and conclusions are given in section 4.6.

4.2 Mass approximation formulae.

Observational constraints on a stellar surface brightness and line-of-sight velocity dispersion profiles of galaxies are the basis of various dynamical modeling techniques of different level of the sophistication and generality. Unfortunately, all available dynamical methods suffer from the common problem - even the best-available kinematics and photometry are unable to uniquely resolve degeneracies for all the model parameters. The key degeneracies are (i) the degeneracy between the unknown total mass profile and velocity anisotropy β (Binney and Tremaine, 2008) and (ii) the deprojection of the surface brightness profile $I(R)$ into a three-dimensional stellar number/mass density even for axisymmetric bodies (e.g., Rybicki, 1987; Gerhard and Binney, 1996).

The (scalar) virial theorem provides the straightforward way to estimate mass (or circular velocity) of an elliptical galaxy satisfying two assumptions. Namely, for a closed stationary spherical system in an isothermal gravitational potential $\Phi(r) = V_c^2 \ln(r) + \text{const}$ a circular velocity V_c is related to the average (luminosity-weighted) line-of-sight velocity dispersion as

$$V_c^2 = 3 \langle \sigma_p^2 \rangle = 3 \frac{\int_0^\infty \sigma_p^2(R) I(R) R dR}{\int_0^\infty I(R) R dR}. \quad (4.1)$$

The mass is then equal to $M(< r) = rV_c^2/G$, where G is the gravitational constant. Apart from the simplicity the main advantage of this approach is its rigorous independence from the velocity anisotropy. However, in practice, observed galaxies are not guaranteed (i) to have spectroscopic data over the full extent of the systems, (ii) be closed, (iii) spherically symmetric and/or (iv) to have the isothermal gravitational potential.

To weaken some of these assumptions it is common to use the spherical Jeans equation which relates the velocity anisotropy parameter β , a volume number density of stars $j(r)$ and a radial velocity dispersion $\sigma_r(r)$:

$$\frac{d}{dr} j \sigma_r^2 + 2 \frac{\beta}{r} j \sigma_r^2 = -j \frac{d\Phi}{dr}, \quad (4.2)$$

where $\beta(r) = 1 - \sigma_\theta^2/\sigma_r^2$ for the spherically symmetric case ($\sigma_\theta(r)$ is the tangential velocity dispersion).

In principle, one can derive $M(< r)$ from the Jeans equation linking 3D quantities $j(r)$ and $\sigma_r(r)$ to the observable surface brightness $I(R)$ and projected velocity dispersion $\sigma_p(R)$ via

$$I(R) = 2 \int_R^\infty \frac{jr dr}{\sqrt{r^2 - R^2}}, \quad (4.3)$$

$$\sigma_p^2(R) I(R) = 2 \int_R^\infty \left(1 - \frac{R^2}{r^2} \beta\right) \frac{j \sigma_r^2 r dr}{\sqrt{r^2 - R^2}} \quad (4.4)$$

for any given anisotropy profile.

Unfortunately observational data alone do not allow one to constrain $\beta(r)$ without invoking sophisticated detailed modeling. From considering relation (4.4) one might expect to find some characteristic radius R_{char} where uncertainty in a circular speed estimate arising from the unknown anisotropy is minimal, thus mitigating the mass-anisotropy degeneracy. The existence of such the radius is first noted in Richstone and Tremaine (1984). In this case the mass estimator can be expressed in the following form:

$$V_c^2(R_{char}) = k\sigma_p^2, \quad (4.5)$$

where k is a coefficient that relates observed velocity dispersion to the circular speed at some radius R_{char} .

This idea is the basis of the simple dynamical mass scaling relations discussed in detail by Churazov et al. (2010) and Wolf et al. (2010). In the paper we concentrate on these two simple mass estimator and test their performance.

4.2.1 Local estimator.

The Churazov et al. estimator is derived from the stationary non-streaming spherical Jeans equation under an assumption of the logarithmic form of the gravitational potential $\Phi(r) = V_c^2 \ln(r) + \text{const.}$ In this case circular speed profiles can be analytically derived for isotropic (assuming $\beta = 0$), radial ($\beta = 1$) and circular ($\beta \rightarrow -\infty$) stellar orbits:

$$\begin{aligned} V_c^{\text{iso}}(r) &= \sigma_p(R)\sqrt{1+\alpha+\gamma} \\ V_c^{\text{circ}}(r) &= \sigma_p(R)\sqrt{2\frac{1+\alpha+\gamma}{\alpha}} \\ V_c^{\text{rad}}(r) &= \sigma_p(R)\sqrt{(\alpha+\gamma)^2+\delta-1}, \end{aligned} \quad (4.6)$$

where

$$\alpha \equiv -\frac{d \ln I(R)}{d \ln R}, \quad \gamma \equiv -\frac{d \ln \sigma_p^2}{d \ln R}, \quad \delta \equiv \frac{d^2 \ln[I(R)\sigma_p^2]}{d(\ln R)^2}. \quad (4.7)$$

The characteristic radius - $R_{char} = R_{\text{sweet}}$ - where the circular speed estimate is expected to be largely insensitive to β is defined as a point of intersection of V_c^{iso} , V_c^{circ} and V_c^{rad} , i.e. where circular speed estimates for different β give similar values. As seen from equations above, R_{sweet} depends only on the *local* properties of the observed surface brightness $I(R)$ and projected velocity dispersion $\sigma_p(R)$ profiles.

For massive elliptical galaxies the spatial variation of $\sigma_p(R)$ is typically much smaller compared to those of $I(R)$, i.e. $\gamma \ll \alpha$ and $\delta \ll \alpha$. In this case equations (4.6) can be simplified to:

$$\begin{aligned} V_c^{\text{iso}} &= \sigma_p(R)\sqrt{\alpha+1} \\ V_c^{\text{circ}} &= \sigma_p(R)\sqrt{2\frac{\alpha+1}{\alpha}} \end{aligned} \quad (4.8)$$

$$V_c^{\text{rad}} = \sigma_p(R) \sqrt{\alpha^2 - 1}.$$

Note, that for $\alpha = 2$ the relation between the circular speed and the observed velocity dispersion (eq. 4.8) does not depend on the anisotropy parameter (Gerhard , 1993), i.e. for the simplified case of nearly flat projected velocity dispersion profile the characteristic radius $R_{\text{char}} = R_2$ where the surface brightness declines as R^{-2} . For the general case R_{sweet} is expected to lie not far from R_2 which is in turn close to the 2D half-light radius $R_{1/2}$. So three quantities can be used as the circular speed estimates: (i) $V_c(R_{\text{sweet}})$ - V_c -estimate from eq. (4.6) at R_{sweet} , (ii) $V_c(R_2)$ - V_c -estimate from eq. (4.6) at R_2 and (iii) $V_c^s(R_2)$ - simplified V_c -estimate from eq. (4.8) at R_2 .

4.2.2 Global estimator.

The mass estimator suggested by Wolf et al. (2010) is derived from the spherical Jeans equation combined with the scalar virial theorem under an assumption of a fairly flat line-of-sight velocity dispersion profile $\sigma_p(R)$. Wolf et al. show that the mass uncertainty arising from the unknown anisotropy of stellar orbits β is minimized at the radius r_3 where the 3D stellar density profile $j(r)$ decays as r^{-3} . Within this radius the galaxy mass can be inferred from the luminosity-weighted average of the observed projected velocity dispersion profile $\langle \sigma_p^2 \rangle$:

$$M(r_3) = 3G^{-1} \langle \sigma_p^2 \rangle r_3, \quad (4.9)$$

As discussed in Wolf et al. (2010), for a wide range of stellar distributions (e.g. for exponential, Gaussian, King, Sérsic profiles) r_3 is close to a 3D half-light radius $r_{1/2}$, which is in turn approximately equal to $4/3R_{1/2}$, where $R_{1/2}$ is a projected half-light radius. The mass approximation formula can be expressed as

$$M_{1/2} \simeq 3G^{-1} \langle \sigma_p^2 \rangle r_{1/2} \simeq 4G^{-1} \langle \sigma_p^2 \rangle R_{1/2}, \quad (4.10)$$

or in terms of the circular speed

$$V_c^2 \left(\frac{4}{3} R_{1/2} \right) \simeq 3 \langle \sigma_p^2 \rangle. \quad (4.11)$$

This theoretical mass estimator is derived for galaxies that (i) are spherical, (ii) non-rotating, (iii) have spatially resolved kinematics over the entire galaxy and (iv) the projected velocity dispersion does not vary with radius.

Although both Churazov et al. and Wolf et al. mass scaling relations are based on the spherical Jeans equation and allow to determine total mass enclosed within a sphere of some characteristic radius R_{char} only, at which the mass estimate is not sensitive to the anisotropy, the final equations and expressions for R_{char} look quite different. The crucial difference between these mass estimators is the following: the Churazov et al. V_c -estimate depends only on local properties of the observed profiles ($\sigma_p(R)$ and log-slopes of $I(R)$ and $\sigma_p(R)$), while Wolf et al. formula requires averaging of the velocity dispersion over entire

extent of the galaxy and determination of the projected half-light radius, i.e. depends on the global galaxy properties. It should be noted that although $R_{1/2}$ is one of the most basic galaxy characteristics, it is not always uniquely determined from observations (see, e.g., Cappellari et al. 2013 for discussion). $R_{1/2}$ is sensitive to (i) quality and depth of photometric data, (ii) used radial range, (iii) methodology applied. Even for nearby galaxies various groups report different values of the effective (half-light) radius. A notable example is a well-studied massive nearby elliptical galaxy M87 (NGC 4486). On the basis of high-quality photometric data Kormendy et al. (2009) derive $R_{1/2} \simeq 194''$ for M87, while Chen et al. (2010) report $R_{1/2} \simeq 107''$ (see also Figure 11 in Chen et al. 2010).

Notice that both estimators give exactly the same characteristic radius and circular speed estimate for the pure power-law surface brightness profile $I(R) \propto R^{-\alpha}$ (the 3D stellar density scales as $j(r) \propto r^{-\alpha-1}$) in the isothermal gravitational potential. For this case the characteristic radius is $R_{char} = R_2 = r_3$ and the circular speed is well approximated by $V_c = \sqrt{3}\sigma_p(R_2) \equiv \sqrt{3\langle\sigma_p^2\rangle}$.

Main properties of Churazov et al. and Wolf et al. estimators are summarized in Table 4.1.

4.3 Tests

In order to compare performance of the local and global approaches, we test them on analytical models, simulated galaxies and real elliptical galaxies, that have already been analyzed using the-state-of-the art dynamical modeling.

4.3.1 Analytic models.

In the case of analytical models we solve the Jeans equation numerically for an assumed set of 3D stellar density, anisotropy and circular speed profiles. The 3D stellar density comes from a deprojected surface brightness profile (assuming spherical symmetry) which is described by the Sérsic law $I(R) = I(R_{1/2}) \exp[-b_n((R/R_{1/2})^{1/n} - 1)]$, where constant b_n is such that $\Gamma(2n) = 2\gamma(2n, b_n)$. The anisotropy is parametrized as $\beta(r) = \frac{\beta_2 r^c + \beta_1 r_a^c}{r^c + r_a^c}$, where c is a concentration parameter and r_a is a some characteristic scale length. Since in real early-type galaxies the distribution of stellar orbits is believed to be close to isotropic at the center and more radial in outer parts, we vary β_1 from -0.7 to 0.0 and β_2 - from 0.1 to 0.5 . Parameters r_a and c range from $0.1R_{1/2} \leq r_a \leq 3.2R_{1/2}$ and $0.1 \leq c \leq 5.1$ respectively.

The circular speed dependence on radius is parametrized as $V_c^2(r) \propto V_1 \frac{r^2}{r^2 + r_c^2} + V_2 \frac{\ln(1 + r/r_s) - r/(r + r_s)}{r/r_s}$ to mimic real V_c -profiles. Let us note that it is a simple analytical representation of the circular velocity and free parameters are chosen to cover the whole range of observed shapes and to probe different parts of real circular speed profiles

Table 4.1: Main properties of Churazov et al. and Wolf et al. estimators.

Estimator	Assumptions	Data	Characteristic radius	σ_p	k
local	dyn. equilibrium	log-slope of $I(R)$	R_{Sweet}	$\sigma_p(R_{\text{Sweet}})$	$\sqrt{1 + \alpha(R_{\text{Sweet}}) + \gamma(R_{\text{Sweet}})}$
	sph. symmetry	log-slope of $\sigma_p(R)$	or R_2	or	or
	no rotation			$\sigma_p(R_2)$	$\sqrt{1 + \alpha(R_2) + \gamma(R_2)}$
	isothermal $\Phi(r)$				or $\sqrt{1 + \alpha(R_2)}$
global	dyn. equilibrium	$\sigma_p(R)$ over whole galaxy	r_3	$\langle \sigma_p^2 \rangle$	$\sqrt{3}$
	sph. symmetry	deprojection of $I(R)$	or $r_{1/2}$		
	no rotation	or determination of $R_{1/2}$	or $4/3R_{1/2}$		
	flat $\sigma_p(R)$				

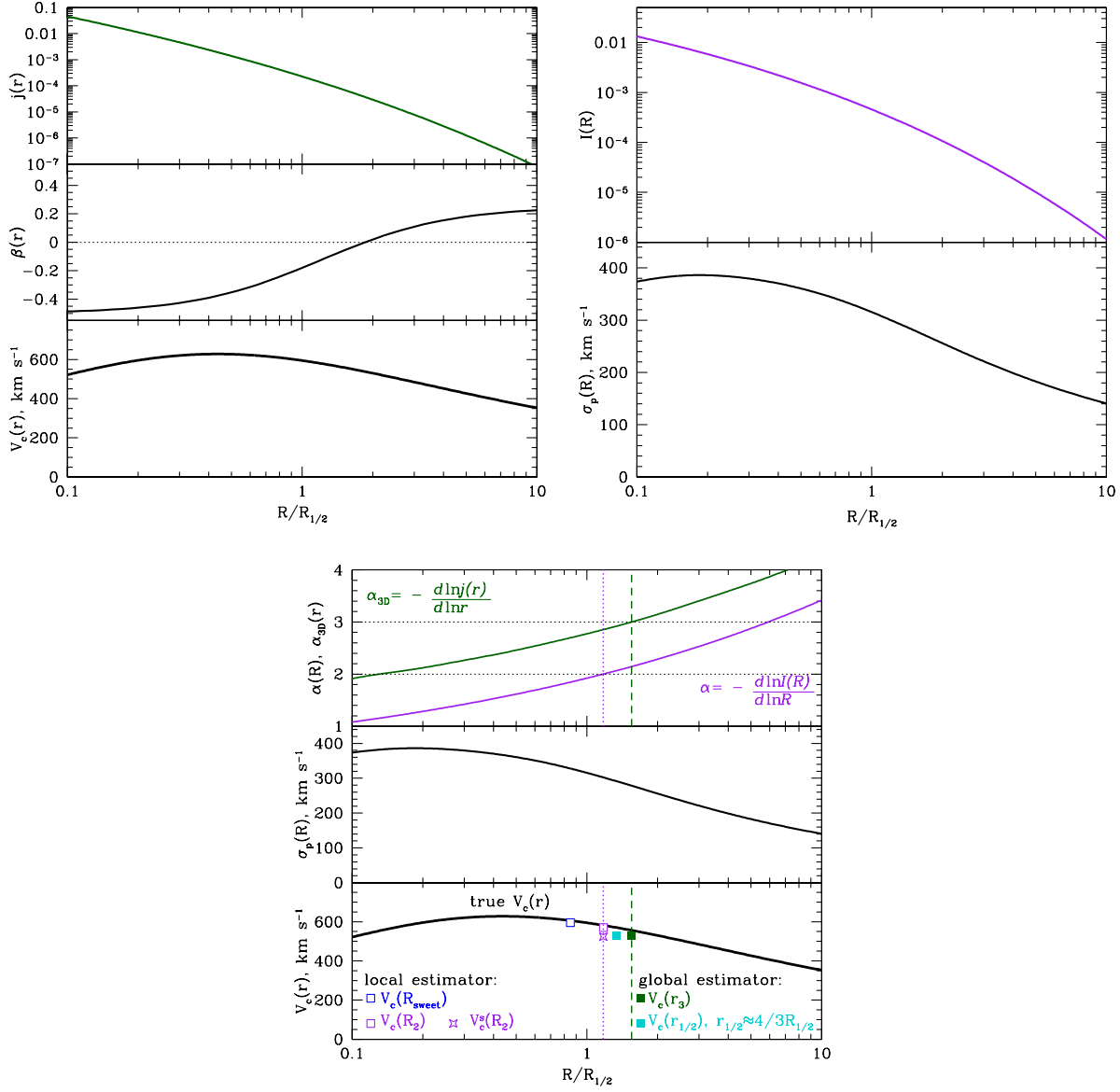


Figure 4.1: Typical profiles considered for a sample of analytical models. Upper left: assumed stellar density $j(r)$, anisotropy $\beta(r)$ and circular speed $V_c(r)$ as functions of $R/R_{1/2}$, where $R_{1/2}$ is a projected half-light radius. Upper right: surface brightness $I(R)$ corresponding to the projection of $j(r)$ (under the assumption of spherical symmetry) and velocity dispersion profile $\sigma_p(R)$ from the spherical Jeans equation. Low panel: profiles, used to get the simple V_c -estimates. Logarithmic slopes of $j(r)$ and $I(R)$ are shown in the top panel as dark green and purple curves respectively. r_3 and R_2 are marked as dark green dashed and purple dotted lines. The simple circular speed estimates are shown as opened and filled symbols of different colors: the filled dark green square is for the global V_c -estimate at r_3 , the filled cyan square - at $r_{1/2} \approx 4/3R_{1/2}$, the open blue square shows the local estimate at R_{sweet} and the open purple square - at R_2 , the open purple star shows the simplified version of the local estimator (eq. 4.8).

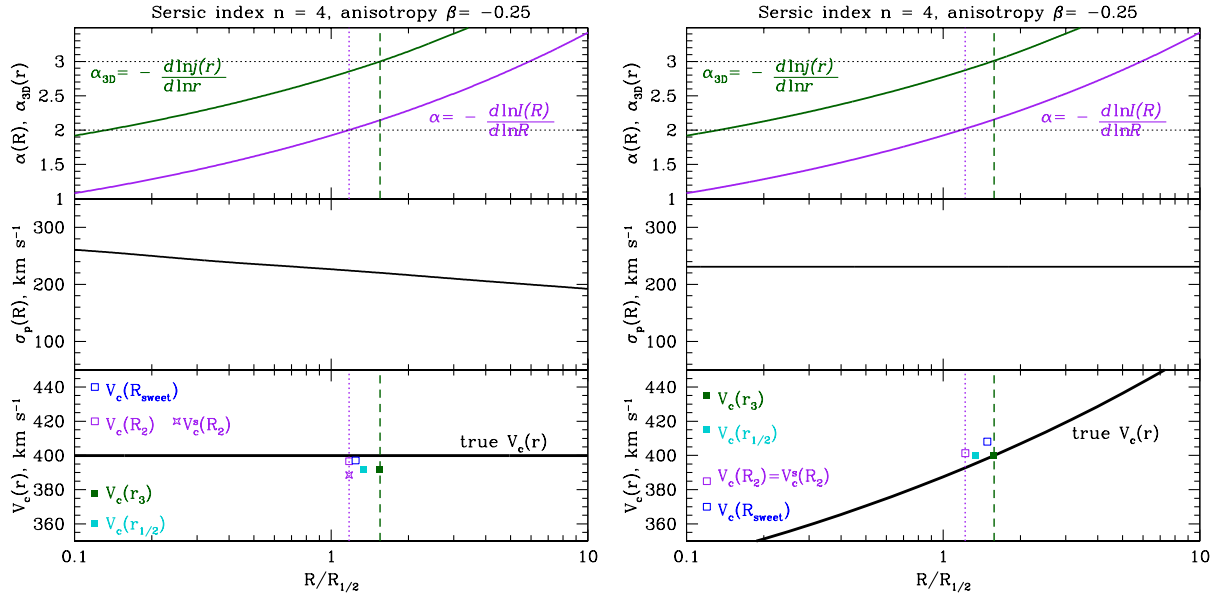


Figure 4.2: Circular speed estimates for ‘ideal’ model galaxy with surface brightness described by Sérsic profile (Sérsic index $n = 4$), constant anisotropy $\beta = -0.25$, flat $V_c(r)$ (left side) or flat $\sigma_p(R)$ (right side). The upper panels show the log-slopes of the 3D stellar density α_{3D} (in dark green) and of the surface brightness α (in purple), the projected velocity dispersion is plotted in the middle panels, and the true circular speed profile as well as simple V_c -estimates are shown in the low panels. The symbols in the low panels are the same as in Figure 4.1.

(rising, roughly flat and decreasing V_c). r_s varies from 0 to 90 half-light radius, r_c changes from 0 to 12 half-light radius.

The luminosity-weighted average of the projected velocity dispersion profile is calculated as $\langle \sigma_p^2 \rangle = \frac{\int I(R) R \sigma_p^2(R) dR}{\int I(R) R dR}$ over $[0.1R_{1/2}; 10R_{1/2}]$. Figure 4.1 illustrates all steps of the analysis and shows typical profiles considered for analytical models.

Performance in an ideal case.

First we apply the simple estimators to the ideal ‘model’ galaxy, which meets all the assumptions used to derive the formulae: dynamical equilibrium, spherical symmetry, no streaming motions, constant anisotropy, flat $V_c(r)$ for Churazov et al. formula and constant $\sigma_p(R)$ for Wolf et al. estimator. Figure 4.2 demonstrates the typical profiles for the ‘ideal’ galaxy and derived estimates. If the circular speed is assumed to be flat, then the derived projected velocity dispersion should monotonically decrease with radius. For the flat velocity dispersion profile and constant anisotropy it is possible to infer the circular speed from a deprojection of $\sigma_p(R)$ and $I(R)$ and solving the Jeans equation (Mamon and Boué 2010). As expected both estimators work well when applied to ‘ideal’ galaxies which meet

all the assumptions. For the flat $V_c(r)$ and decreasing $\sigma_p(R)$ Wolf et al formula slightly underestimates the true circular speed with typical deviation of $\approx -3\%$, for constant $\sigma_p(R)$ and growing $V_c(r)$ Churazov et al. approach tends to overestimate the true V_c by $\approx -3\%$.

Grid of analytical models.

We explore ~ 30000 analytical models, described by the Sérsic law with Sérsic index $2 < n < 20$, mildly increasing with radius anisotropy profile and circular speed characteristic for (i) dark-matter dominated dwarf spheroidal galaxies (growing V_c) and (ii) massive elliptical galaxies (roughly flat and decreasing with radius V_c). However, we do not aim to explore the whole parameter space, the idea is to understand how sensitive the estimators are to the assumption of a flat $V_c(r)$ or $\sigma_p(R)$ and to the mildly varying anisotropy. The resulting histograms for the local estimator (upper row) and the global estimator (lower row) are shown in Figure 4.3. The RMS-scatter for the global estimator is almost twice larger than for the local one, indicating that the latter is less sensitive to the assumption of a constant circular velocity, than the Wolf et al. estimator to the assumption of a flat velocity dispersion.

As the Churazov et al. derivation assumes the isothermal gravitational potential (i.e. flat $V_c(r)$) it would be interesting to test how accuracy of the estimator depends on the slope of the circular speed profile. Indeed, there is a clear correlation between the deviation Δ of the estimated circular speed from the true one and the logarithmic slope of the true $V_c(r)$ at R_{sweet} : $\Delta \approx k \times \left(-\frac{d \ln V_c^2}{d \ln r} \right)$ (Figure 4.4, the black histogram shows the average deviation).

The details of the mean correlation between Δ and $-\frac{d \ln V_c^2}{d \ln r}$ depends on the sampling of the parameter space. However the main trend for the local estimator seems to be rather universal. For growing/decreasing V_c near R_{sweet} (which is close to R_2) the method tends to overestimate/underestimate the true value by a factor of $\approx 1 + 0.1 \left(-\frac{d \ln V_c^2}{d \ln r} \right)$ (order of magnitude estimate). For flat V_c near R_{sweet} the local estimator is largely unbiased when averaged over the parameter space covered by our grid of analytic models. When deviations are plotted against the logarithmic slope of the projected velocity dispersion $\gamma = -\frac{d \ln \sigma_p^2}{d \ln R}$ at R_{sweet} , a similar pattern is observed. If σ_p grows with radius in the vicinity of R_{sweet} , then the local V_c -estimate overestimates the true circular speed. For flat or moderately falling observed velocity dispersion profiles Churazov et al. method seems to recover almost unbiased V_c -estimate.

The global estimator demonstrates more complex dependence on the slope of the circular speed radial profile, giving a noticeable negative bias for a flat circular speed (for the flat $V_c(r)$ the observed velocity dispersion might vary significantly with radius). As expected, Wolf et al. formula works best for roughly flat line-of-sight velocity dispersion profiles. The global V_c -estimate appears to be significantly overestimated relative to the true one for σ_p rapidly increasing with radius ($\gamma \lesssim 0.3$). Large negative deviations are

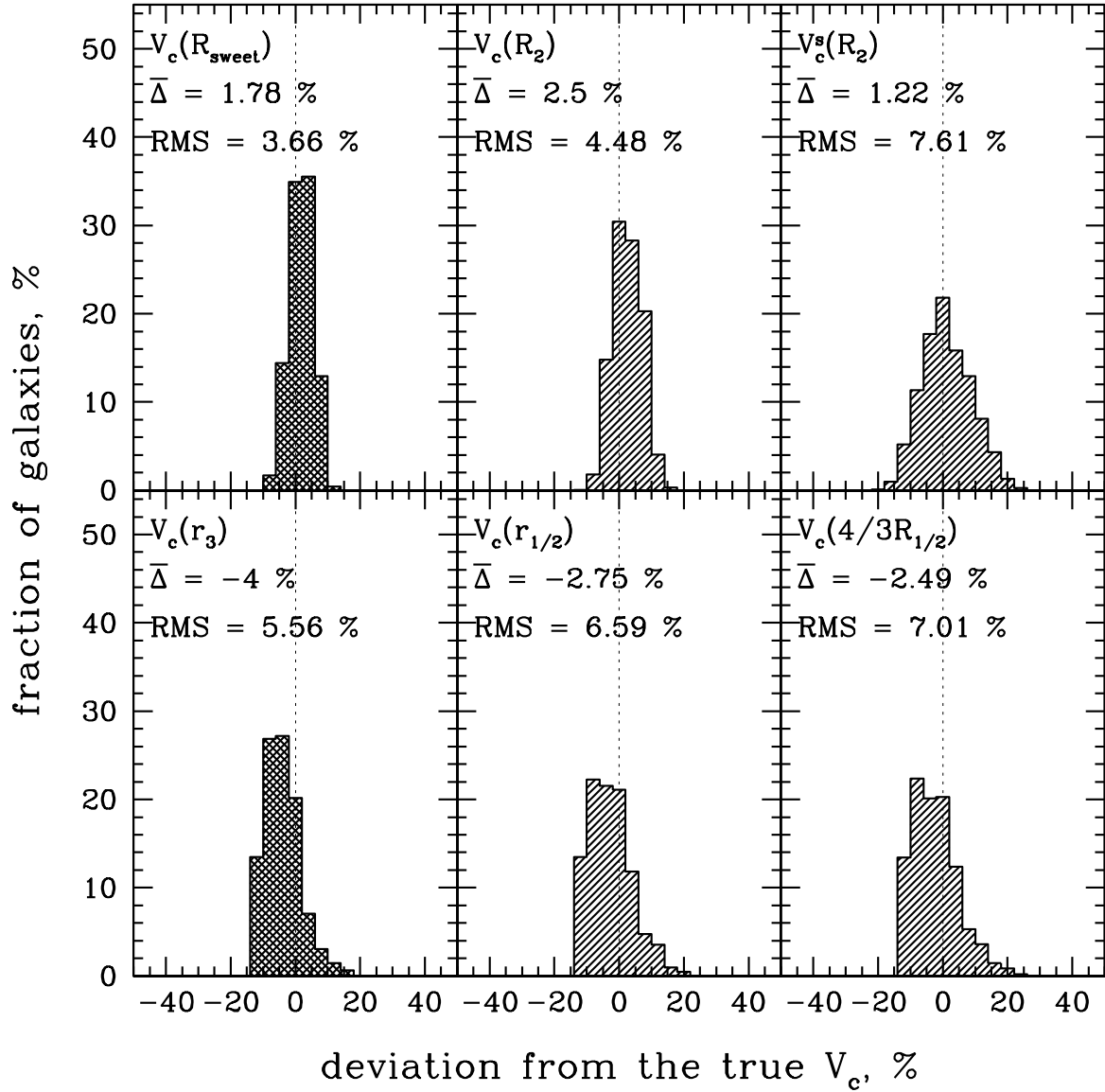


Figure 4.3: The histograms of deviations of simple V_c -estimates from the true value for the local (upper row) and the global estimators (lower row) for model spherical galaxies, described by Sérsic surface brightness profile, mildly growing anisotropy, and circular speed profile that is similar in shape to the observed circular velocity curves. Deviations are calculated as $\Delta = \frac{V_c - V_c^{true}}{V_c^{true}}$, where estimated V_c and true V_c^{true} are taken at the same characteristic radius.

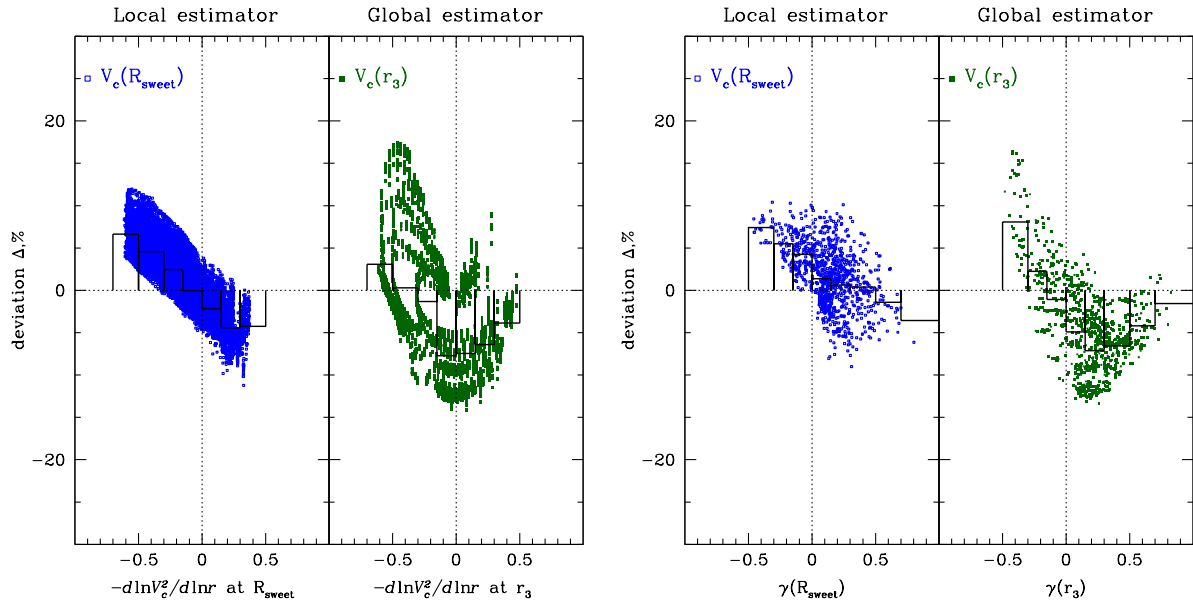


Figure 4.4: Dependence of the error in the V_c estimation on properties of the true $V_c(r)$ and observed $\sigma_p(R)$ profiles. Left: Deviation Δ of the estimated circular speed from the true one as a function of a log-slope of the true circular speed $-\frac{d \ln V_c^2}{d \ln r}$ taken at a characteristic radius (R_{sweet} for the local estimator and r_3 for the global one). The histogram shows the average deviation in a chosen bin of logarithmic slopes. Right: Deviation as a function of the log-slope of the projected velocity dispersion $\gamma = -\frac{d \ln \sigma_p^2}{d \ln R}$ at a characteristic radius. Only 1000 randomly chosen realizations are shown for clarity.

present for models with $\sigma_p(R)$ showing a bump, i.e. when $\gamma(R)$ changes a sign.

Figure 4.4 indicates that the local estimator should be applied with cautious to systems with increasing velocity dispersion profiles and/or to systems that are described by growing circular speed profiles in the vicinity of R_2 . As the Wolf et al. estimator relies on global properties of the galaxies, it works well if the velocity dispersion does not change significantly with radius over the whole extent of the system. Roughly speaking, Wolf et al. formula is appropriate for dwarf spheroidal galaxies (see Kowalczyk et al. 2013 who have tested the global estimator on a sample of simulated dSph) and for a subset of elliptical galaxies with approximately flat velocity dispersion profile, while Churazov et al. estimator works for elliptical galaxies in general.

It should be also noted that for large Sérsic indices ($n > 8 - 10$), typical for massive ellipticals sitting at the centers of groups or clusters, log-slope of the surface brightness α is close to 2 over a wide range of radii, and in this radial range the true circular speed is well described by the isotropic one V_c^{iso} (eq. 4.6).

4.3.2 Tests on simulated galaxies.

From spherical models we now turn to a sample of ‘zoom-in’ cosmological simulations of individual galaxies (Oser et al. 2010), which span a wide range in mass, $7 \times 10^{11} M_\odot h^{-1} < M_{vir} < 2.7 \times 10^{13} M_\odot h^{-1}$, $h = 0.72$, where M_{vir} is the present day virial halo mass. Those massive simulated galaxies have properties very similar to observed nearby early-type galaxies as found by ATLAS^{3d} project (Naab et al. 2013).

Churazov et al. estimator has been tested in Lyskova et al. (2012) and we follow the same analysis procedure. Briefly, we first exclude satellites from the galaxy image and calculate the radial profiles $I(R)$, $\sigma_p(R)$ and the true circular speed $V_c^{true}(r) = \sqrt{GM(< r)/r}$ in a set of logarithmic concentric annuli/shells around the halo center. We define R_{sweet} as a radius where $(V_c^{iso} - \bar{V})^2 + (V_c^{rad} - \bar{V})^2 + (V_c^{circ} - \bar{V})^2$, where $\bar{V} = (V_c^{iso} + V_c^{rad} + V_c^{circ})/3$, is minimal. At R_{sweet} we take V_c^{iso} as an estimate of the circular speed and calculate a deviation from the true value at this radius $\Delta = (V_c^{iso} - V_c^{true}) / V_c^{true}$. We consider three V_c -estimates: (i) $V_c(R_{sweet}) = V_c^{iso}(R_{sweet})$ defined from eq. (4.6), (ii) $V_c(R_2) = V_c^{iso}(R_2)$ defined from eq. (4.6) and (iii) $V_c^s(R_2) = V_c^{iso,s.}(R_2)$ defined from eq. (4.8).

We apply the estimators to a subsample of massive ($\sigma_p(R_{1/2}) > 150 \text{ km s}^{-1}$) simulated galaxies and exclude merging and oblate galaxies seen along the rotation axis.

Figure 4.5 shows the fraction of galaxies versus the deviation $\Delta = (V_c - V_c^{true}) / V_c^{true}$ for Churazov et al. V_c -estimator. Left and rights panels of Figure 4.5, demonstrating the performance of local estimates $V_c(R_{sweet})$ and $V_c^s(R_2)$, has been already presented in Lyskova et al. (2012) (Figure 8). Note, that $V_c(R_{sweet})$ and $V_c(R_2)$ estimates show very similar results: the average over the sample deviation is close to zero and RMS-scatter $\approx 5 - 6\%$. So the radius R_2 , which is uniquely determined from the slope of the surface brightness profile, can be used instead of R_{sweet} , which depends also on the log-slope of the projected velocity dispersion profile $-\frac{d \ln \sigma_p^2}{d \ln R}$ and the second derivative $\frac{d^2 \ln[I(R)\sigma_p^2]}{d(\ln R)^2}$.

To test robustness of Wolf et al. estimator on the sample of simulated galaxies we

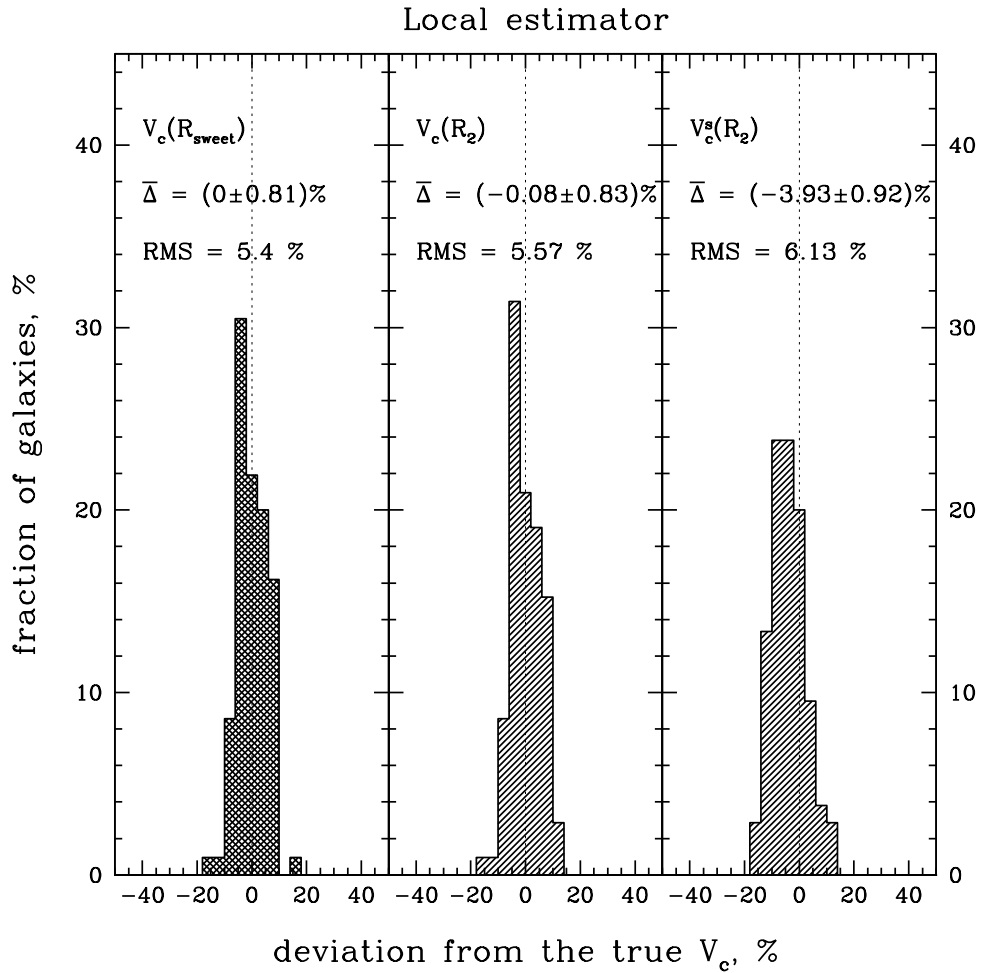


Figure 4.5: The histograms of deviations for the local V_c -estimator from the true circular speed for simulated galaxies. $V_c(R_{\text{sweet}})$ and $V_c(R_2)$ are calculated from equations (4.6) at R_{sweet} (radius where $V_c^{\text{iso}} \approx V_c^{\text{circ}} \approx V_c^{\text{rad}}$) and R_2 (where $I \propto R^{-2}$) correspondingly. $V_c^s(R_2)$ comes from equations (4.8).

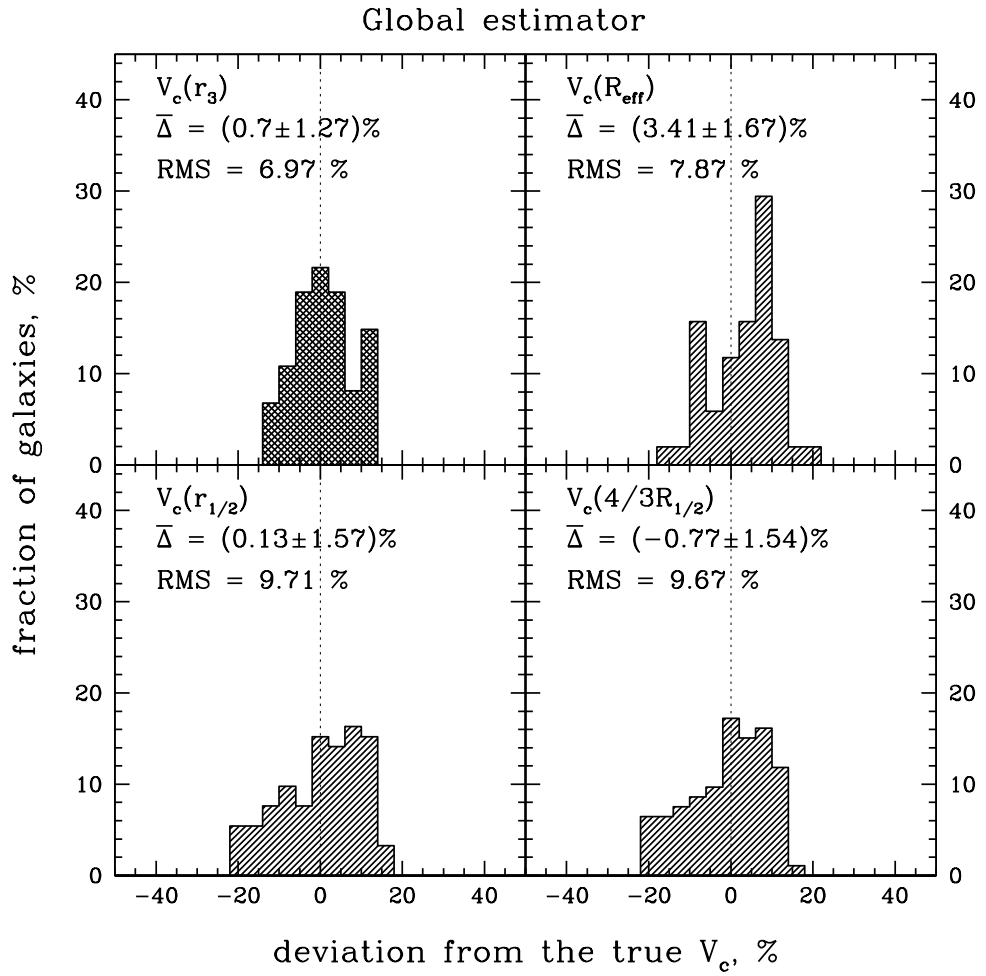


Figure 4.6: The histograms of the deviations for global V_c -estimator from the true circular speed for simulated galaxies. Deviations are calculated at the following characteristic radii: (i) r_3 (left upper panel), where $j(R) \propto r^{-3}$, (ii) $4/3$ ‘observational’ effective radius resulting from the Sérsic fit to the surface brightness over $[3r_{\text{soft}}; 0.1R_{\text{vir}}]$ (right upper panel), (iii) 3D half-light radius $r_{1/2}$ (left lower panel) and (iv) $4/3$ projected half-light radius $R_{1/2}$ (right lower panel).

need to compute (i) luminosity-weighted projected velocity dispersion $\langle \sigma_p^2 \rangle$ over some radial range $[R_{min}; R_{max}]$, (ii) characteristic radii r_3 , $r_{1/2}$ and $4/3R_{1/2}$ where anisotropy is expected to play minor role in circular speed determination. r_3 is calculated as a radius where 3D stellar density declines as r^{-3} , the 3D half-light radius $r_{1/2}$ and projected half-light radius $R_{1/2}$ are computed as a radius of the sphere/circle which contains half of the 3D/projected stellar mass respectively. Since in real observations information on total light is not available, we also determine an ‘observational’ effective radius R_{eff} coming from the Sérsic fit $I(R) \propto \exp(-b_n(R/R_{eff})^{1/n})$ to the observed surface brightness over a radial range $[R'_{min}; R'_{max}]$. We choose $R_{min} = R'_{min} = 3r_{soft}$, where $r_{soft} \approx 400 \text{ pc} h^{-1}$ is a softening length used in simulations and $3r_{soft}$ is the maximum radius where profiles could be affected by the softening. $R_{max} = R'_{max} = 0.1R_{vir}$, where R_{vir} is a halo virial radius ($\equiv R_{200}$, the radius where the spherical overdensity drops below 200 times the critical density of the Universe).

Figure 4.6 shows the performance of Wolf et al. estimator at different radii: (i) r_3 (left upper panel), where $\alpha_{3D} = -\frac{d \ln j(r)}{d \ln r} = 3$, (ii) $4/3 \times$ projected effective radius defined from the Sérsic fit (right upper panel), (iii) 3D half-light radius $r_{1/2}$ (left lower panel) and (iv) $4/3 \times$ 2D half-light radius $R_{1/2}$ (right lower panel). While the global estimates $V_c(r_3)$ and $V_c(r_{1/2})$ are almost unbiased (when averaged over the sample of simulated galaxies), the average deviation of the global $V_c(4/3R_{eff})$ is $\approx 3 - 4\%$. RMS-scatter for all cases is equal to $\approx 7 - 10\%$, i.e. slightly larger than for Churazov et al. estimator. As mentioned above, observed profiles at $R < R_{min} = 3r_{soft}$ could be affected by the softening, and for the analysis of the Wolf et al. estimator we consider only those simulated galaxies for which the characteristic radius is larger than $2R_{min} = 6r_{soft}$. This selection criteria effectively keeps only the most massive galaxies in the sample with roughly isothermal gravitational potential (see Section 3.2 in Lyskova et al. 2012). For those galaxies the virial theorem states that V_c at any radius is well approximated by $3\langle \sigma_p^2 \rangle$ and the exact value of the characteristic radius is not important.

If we vary R_{max} and R'_{max} in reasonable limits, the values of R_{eff} and $\langle \sigma_p^2 \rangle$ for individual galaxies do change, but not dramatically, and the average deviation Δ remains practically the same ($\overline{\Delta} \lesssim 3 - 5\%$) with RMS-scatter $\simeq 8 - 10\%$.

Tests on model spherical galaxies (section 4.3.1) show that the deviation Δ correlates with the logarithmic slope of the true circular speed. For the sample of simulated galaxies we also observe similar trend (Figure 4.7), but not as strong as for model spherical galaxies. The Wolf et al. estimator (at r_3) also shows some correlation with the log-slope of V_c^{true} . No clear correlation between simple estimates and the logarithmic slope of the projected velocity dispersion is found.

Trends with the virial mass.

In Figure 4.8 we show the deviation of simple estimates from the true circular speed as a function of virial halo mass M_{vir} . Dots represent the deviations for individual galaxies and lines are the least-square linear fits of $\Delta[\%] = a \cdot \lg\left(\frac{M_{vir}}{10^{10} M_\odot h^{-1}}\right) + b$. Note, that for

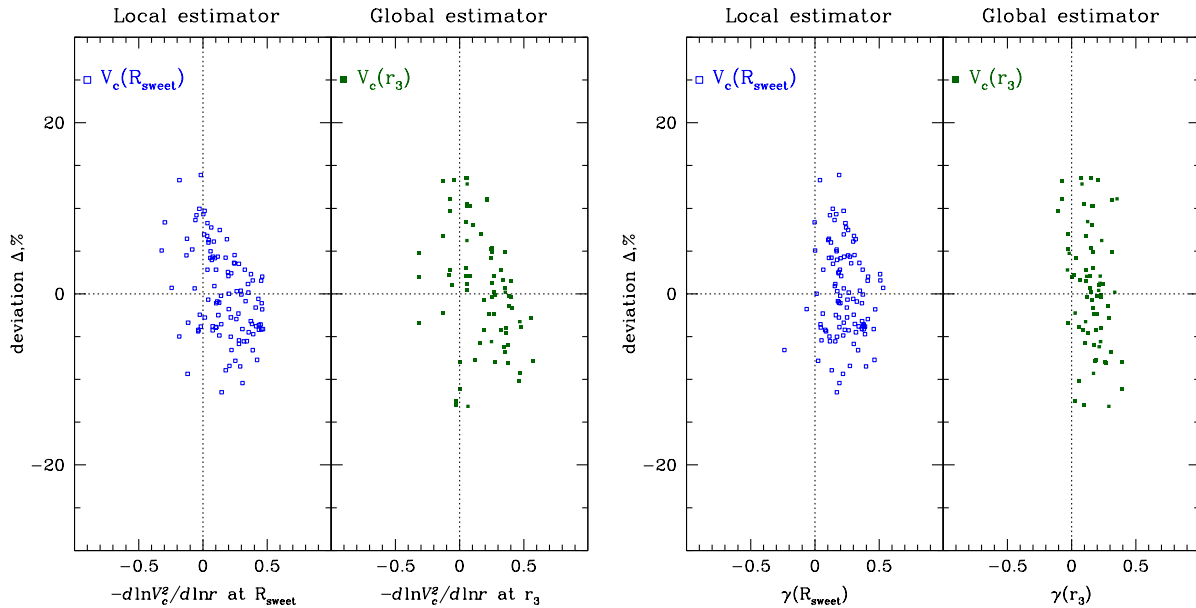


Figure 4.7: Observed correlations for simulated galaxies. Left: Deviation of the estimated circular speed for simulated galaxies from the true one as a function of a log-slope of the true circular speed $-\frac{d \ln V_c^2}{d \ln r}$. Right: Deviation of the estimated circular speed for simulated galaxies from the true one as a function of a log-slope of the projected velocity dispersion profile $\gamma = -\frac{d \ln \sigma_p^2}{d \ln R}$.

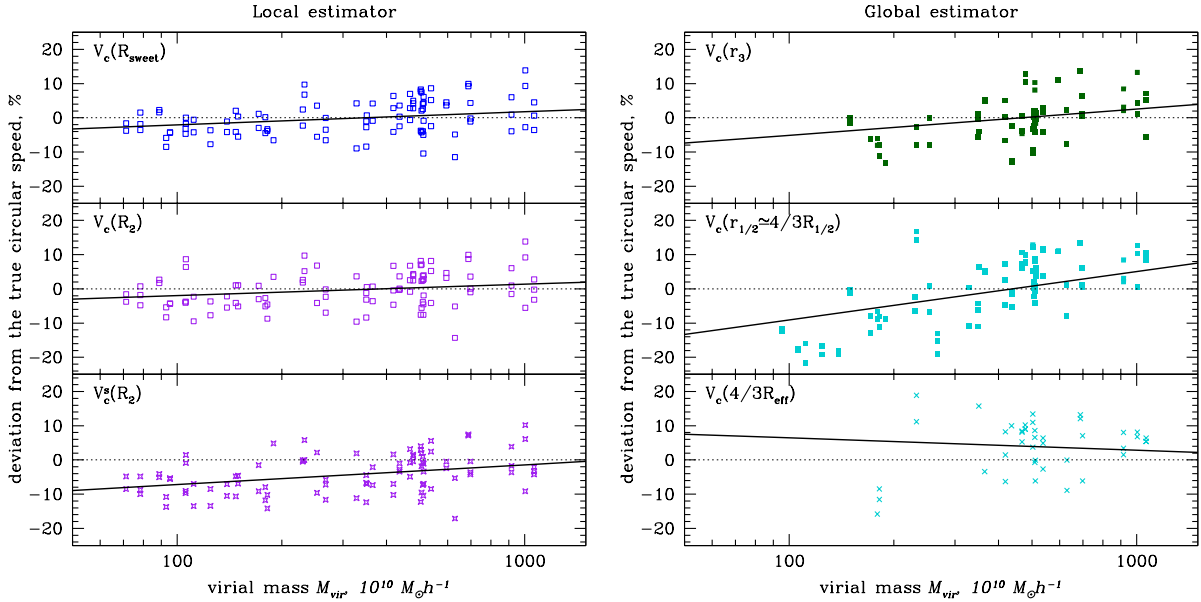


Figure 4.8: Deviation of the estimated circular speed from the true one as a function of the virial halo mass (extracted from simulations). The local formula (left side) recovers the true circular speed for a wide range of the virial masses almost equally well. The global approach works better for the most massive galaxies in the sample ($M_{vir} \gtrsim 3 \cdot 10^{12} M_\odot h^{-1}$), than for the less massive galaxies. One can notice that the global estimator at different characteristic radii probes the different range of virial masses. When using the global estimator at $R_{char} = \{r_3, r_{1/2}, 4/3R_{\text{eff}}\}$ we retain in the sample only the galaxies which have $R_{char} > 2R_{min} = 6r_{soft}$. As a result 3 panels for $R_{char} = \{r_3, r_{1/2}, 4/3R_{\text{eff}}\}$ probe different subsamples on the low mass end. In addition, the characteristic radii r_3 and $r_{1/2}$, which are expected to be close to each other for commonly used analytic stellar light distributions (e.g., for Sérsic models) for simulated galaxies sometimes differ by a factor $\sim 2 - 3$.

Table 4.2: Sample of real elliptical galaxies analyzed using the Schwarzschild modeling (7 Coma galaxies from Thomas et al 2007 and M87 (NGC4486) from Murphy et al. 2011). The effective radii for the Coma galaxies are taken from Thomas et al. 2007 and the effective radius of M87 comes from Kormendy et al. 2009

name	other common names	R_{eff} , arcsec
NGC 4957	GMP 0144	18.4
NGC 4952	GMP 0282	14.1
NGC 4908	GMP 2417	7.1
NGC 4869	GMP 3510	7.6
IC 3947	GMP 3958	3.3
NGC 4827	GMP 5279	13.6
NGC 4807	GMP 5975	6.7
NGC 4486	M87	194.41

the local $V_c(R_2)$, $V_c(R_{\text{sweet}})$ and global $V_c(r_3)$ trends with the virial mass are quite weak. The Wolf et al. formula has been applied only to simulated galaxies with the characteristic radius $R_{\text{char}} \geq 2R_{\min} = 6r_{\text{soft}}$, so the probed range of masses is different for different characteristic radii.

4.4 Comparison of simple mass estimators with a state-of-the-art analysis.

It is interesting to test simple mass estimators on real elliptical galaxies, which have already been studied in detail using the state-of-the-art dynamical modeling. A number of such modelled galaxies is constantly increasing, but the extent of kinematic data for majority of them is limited to $\approx R_{\text{eff}}$ only. For successful mass determination with simple estimators it is desirable to have spatially resolved kinematics at least out to $\approx 1.2 - 1.5R_{\text{eff}}$. As a target sample we use early-type galaxies from the Coma cluster, modelled using the Schwarzschild orbit superposition method by Thomas et al. (2007), and the giant elliptical galaxy M87 from the Virgo cluster modelled by Murphy et al. (2011). For our purposes we choose only those galaxies from the Thomas et al. sample where kinematic measurements are available out to $\gtrsim 1.5R_{\text{eff}}$ and $\sigma_p(R_{\text{eff}}) > V_{\text{rot}}(R_{\text{eff}})$, where σ_p and V_{rot} are the projected velocity dispersion and rotation velocity measured along the major axis.

Galaxies of our target sample (7 Coma galaxies + M87) are listed in Table 4.2. We use the surface brightness and a root-mean-square velocity ($V_{\text{rms}}(R)' = \sqrt{\sigma_p^2(R) + V_{\text{rot}}^2(R)}$) to recover the circular speed of the galaxy via equations (4.6) and (4.11). Figure 4.9 provides an example of the data we use to compare simple V_c -estimators with the results of the Schwarzschild modeling. The logarithmic slope of the surface brightness profile $\left(\alpha = -\frac{d \ln I(R)}{d \ln R}\right)$ is shown in the panel A, the radius R_2 where $\alpha = 2$ is marked as a

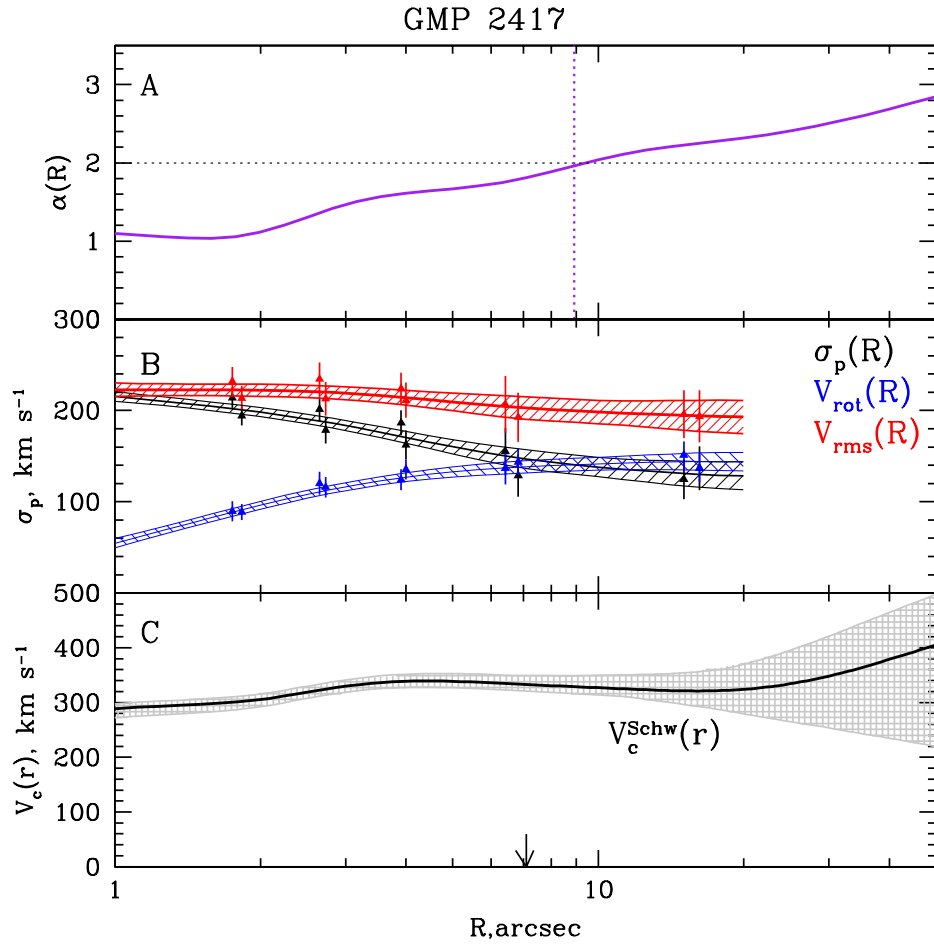


Figure 4.9: Panel A: the log-slope of the surface brightness, radius R_2 where $\alpha = 2$ is marked with the purple dotted line. Panel B: the velocity dispersion and rotational velocity measurements along the major axis of the galaxy. Panel C: the circular speed curve (in black) with errorbars (gray-shaded area) derived from the Schwarzschild modeling. The effective radius is marked as an arrow.

purple dashed line. Panel B presents the major axis rotational velocity V_{rot} (blue triangles) and projected velocity dispersion σ_p (black triangles) measurements with errorbars (Σ_{rot} and Σ_σ correspondingly). The rms-velocity with observational errors $\Sigma_{rms}^2 = \Sigma_{rot}^2 + \Sigma_\sigma^2$ is shown as red triangles. The interpolated curves (the interpolation procedure is described in Churazov et al. 2010) for kinematic data are shown as solid lines. Shaded regions shows the measurement uncertainties. The best-fitting circular speed $V_c^{Schw}(r)$ (black solid line) coming from the Schwarzschild orbit-superposition technique with 1σ -uncertainties (grey shaded area) is depicted in Panel C. An arrow marks the effective radius.

For each galaxy we compare simple circular speed estimators with the best-fit circular velocity. The luminosity-weighted velocity dispersion $\langle \sigma_p \rangle$ (which is needed for the Wolf et al. estimator) is averaged over the radial range where the observational data are available. As some galaxies show a moderate rotation, we test also the slightly modified version of the Wolf et al. formula where $\langle \sigma_p \rangle$ is substituted by the average luminosity-weighted rms-velocity $\langle V_{rms} \rangle$.

The results are presented in Figure 4.10. Panel A shows the rms-velocity and rotation velocity measured along the major axis of the galaxy. Panel B shows the circular speed V_c^{Schw} from the dynamical modeling (black curve) with uncertainties (grey shaded region); plotted in blue is the isotropic circular speed calculated from eq. (4.6) where $\sigma_p(R)$ is replaced with $V_{rms}(R)$, blue shaded region reflects the uncertainties associated with V_{rms} -measurements. Simple V_c -estimates are shown as squares of different color: the blue open square corresponds to the local V_c -estimate at R_{sweet} , the purple open square - at R_2 , global estimates (calculated as $\langle \sigma_p^2 \rangle$ and $\langle V_{rms}^2 \rangle$) at $4/3R_{eff}$ are shown as the brown and orange filled squares. The effective radius R_{eff} is shown with an arrow, and the radius R_2 - as a purple dashed line. As the ‘true’ (coming from the Schwarzschild modeling) circular speed and observed line-of-sight velocity dispersion (or rms-velocity) profiles are close to being flat, both Churazov et al and Wolf et al. estimators are expected to recover the circular speed reasonably well. Note that galaxies in the chosen subsample do not match perfectly all the requirement for using the simple mass estimators. Namely, most of them are flattened and some are mildly rotating. Nevertheless, we see that simple V_c -estimates agree well with V_c^{Schw} , especially for slowly rotating galaxies (GMP 0144, GMP 3510, GMP 5279), where simple estimates (local V_c -estimates at R_{sweet} and R_2) almost coincides with the $V_c^{Schw}(r)$ value. Table 4.3 provides the summary on the comparison of simple V_c -estimates with the circular velocity from the Schwarzschild modeling. Used forms of the estimators are listed in the Column (1), the mean deviation $\bar{\Delta}$ from the V_c^{Schw} - in the Column (2). RMS-scatter around $\bar{\Delta}$ (in Column (3)) is calculated as $\sqrt{\frac{\sum_{i=1}^N (\Delta_i - \bar{\Delta})^2}{N - 1}}$. Column (4) shows an uncertainty Σ_{obs} associated with measurement errors. For each galaxy Σ_{obs} is calculated as $\sqrt{1 + \alpha + \gamma \Sigma_{rms}}$ (eq. (4.6)). The column (5) lists the average errors on the best-fit circular speed from the Schwarzschild analysis taken at the corresponding characteristic radius.

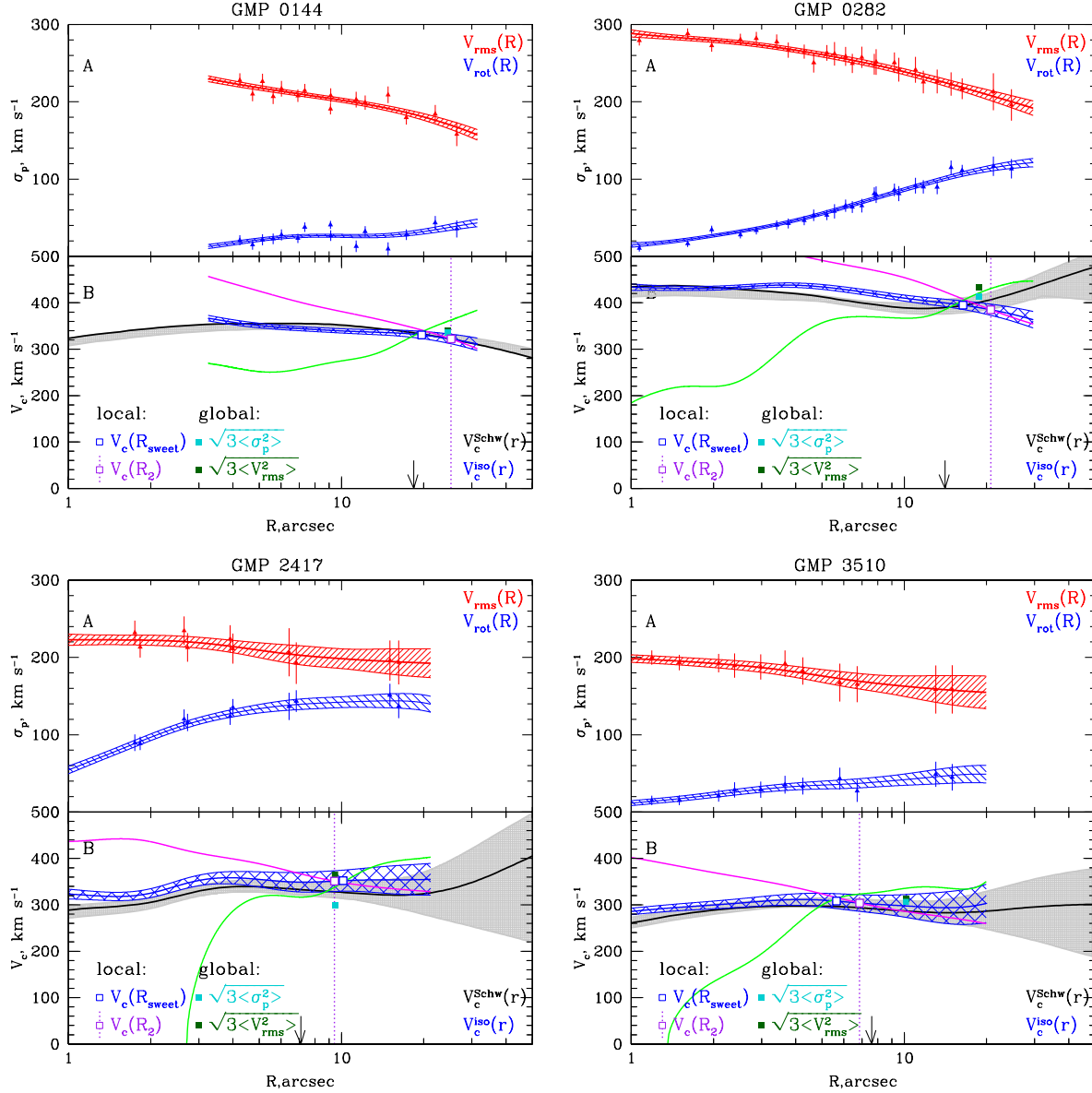


Figure 4.10: Comparison of simple V_c -estimates with the circular speed (V_c^{Schw}) coming from the dynamical modeling. Panel A shows data on the rms-velocity ($V_{rms} = \sqrt{\sigma_p^2 + V_{rot}^2}$) profile and rotation velocity V_{rot} measured along a major axis as well as interpolated curves used to calculate the logarithmic derivatives. Panel B presents the circular speed resulting from the Schwarzschild modeling (black thick curve) with error bars (grey shaded region), the isotropic circular speed V_c^{iso} (in blue) calculated via eq. 4.6 with ‘observational’ error bars Σ_{obs} determined from the measurement uncertainties on V_{rms} . The circular speed profiles for pure circular and pure radial orbits are shown as magenta and green curves correspondingly. The arrow shows and the dotted purple line show the effective radius R_{eff} and R_2 respectively.

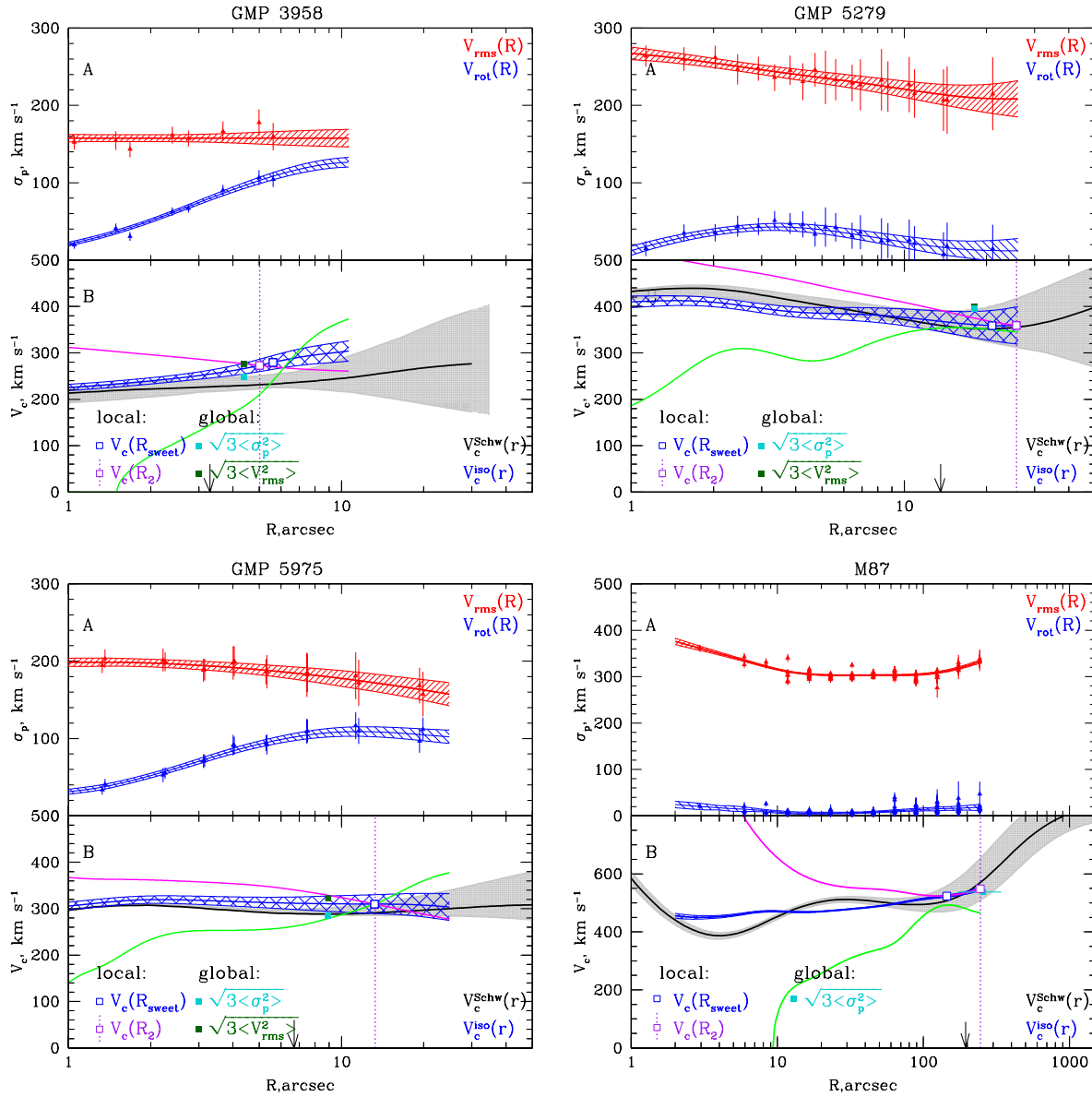


Figure 4.10: (continue)

Table 4.3: Simple V_c -estimates and V_c from dynamical modeling. The columns are: (1) - the simple V_c -estimator; (2) - averaged over the sample of 8 galaxies (7 Coma galaxies + M87) deviation of the estimated V_c from V_c^{Schw} resulting from dynamical modeling; (3) - RMS-scatter around the average deviation; (4) - average observational error at the characteristic radius normalised to V_c^{Schw} ; (5) - average error on dynamically derived V_c^{Schw} at the characteristic radius. Since the bias for the local estimators is mostly driven by a single galaxy IC 3947 (the most compact galaxies in the sample), we exclude this galaxy and provide the results of the analysis of the remaining galaxies in the parenthesis.

estimator	$\bar{\Delta} = \left\langle \frac{V_c}{V_c^{Schw}} - 1 \right\rangle, \%$	RMS-scatter, %	$\langle \Sigma_{obs} \rangle / V_c^{Schw}, \%$	$\langle \Sigma_{Schw} \rangle / V_c^{Schw}, \%$
(1)	(2)	(3)	(4)	(5)
$\bar{V}_c(R_{sweet})$	5.3 (3.2)	6.6 (3.1)	$\pm 5.8 (\pm 5.7)$	$+8.1/-4.8$ ($+8.0/-4.9$)
$\bar{V}_c(R_2)$	3.3 (1.2)	7.5 (4.9)	$\pm 6.2 (\pm 6.3)$	$+9.6/-6.4$ ($+9.7/-6.7$)
$\sqrt{3 \langle \sigma_p^2 \rangle}$ at $4/3R_{eff}$	2.0 (1.1)	7.4 (7.6)	$\pm 5.7 (\pm 5.8)$	$+8.4/-5.4$ ($+8.4/-5.6$)
$\sqrt{3 \langle V_{rms}^2 \rangle}$ at $4/3R_{eff}$	8.9 (7.3)	7.8 (6.9)	$\pm 5.7 (\pm 5.8)$	$+8.4/-5.4$ ($+8.4/-5.6$)

Table 4.4: Summary table. The columns are: (1) - the simple V_c -estimator; (2) and (3) - the average deviation $\bar{\Delta}$, % and RMS-scatter for the sample of simulated galaxies; (4) and (5) - the average deviation $\bar{\Delta}$, % and RMS-scatter for the sample of real elliptical galaxies.

estimator	simulated galaxies		real galaxies	
	$\bar{\Delta}$, %	RMS-scatter, %	$\bar{\Delta}$, %	RMS-scatter, %
(1)	(2)	(3)	(4)	(5)
$V_c(R_{\text{sweet}})$	0.0 ± 0.8	5.4	5.3	6.6
$V_c(R_2)$	-0.7 ± 0.9	5.9	3.3	7.5
$V_c(r_3)$	0.9 ± 1.2	7.1		
$V_c(r_{1/2})$	0.1 ± 1.6	9.7		
$V_c(4/3R_{\text{eff}})$	3.4 ± 1.7	7.9	2.0	7.4

4.5 Mass proxy.

Our tests on simulated and real elliptical galaxies suggest, that simple estimators could be helpful for analyzing large surveys. We also test on simulated galaxies whether the simple circular speed estimates could be used as a proxy for the virial galaxy mass. The simple estimators by definition are closely related to the projected velocity dispersion: the local $V_c(R_2) = \sqrt{1 + \alpha + \gamma} \cdot \sigma_p(R_2) \approx \sqrt{3}\sigma_p(R_2)$ (equation 4.6, $\alpha = 2, \gamma \ll \alpha$) and the global $V_c(r_3) = \sqrt{3 \langle \sigma_p^2 \rangle}$. Let us plot $\sigma_p(R_2)$ and $\langle \sigma_p^2 \rangle$ against the virial halo mass for each individual galaxy to see how well these quantities correlate with each other.

Figure 4.11 shows the virial galaxy mass as a function of the local value of the projected velocity dispersion R_2 (left side) and the luminosity-weighted average velocity dispersion $\sqrt{\langle \sigma_p^2 \rangle}$ (right side). Color squares depict the velocity dispersion and the virial mass for individual simulated galaxies (upper panels) and the straight line is the least-square linear fit to these data points. Deviations from the linear fit are shown on the lower panel.

The virial mass M_{vir} (in $M_\odot h^{-1}$) can be approximated by $M_{vir} \approx 6 \cdot 10^{12} \left(\frac{\sigma_p(R_2)}{200 \text{ km s}^{-1}} \right)^4$

with RMS-scatter $\approx 38\%$ or $M_{vir} \approx 4.5 \cdot 10^{12} \left(\frac{\sqrt{\langle \sigma_p^2 \rangle}}{200 \text{ km s}^{-1}} \right)^5$ with RMS $\approx 37\%$. The

local $\sigma_p(R_2)$ has the same scatter as the luminosity-weighted average line-of-sight velocity dispersion (global estimate). $\langle \sigma_p^2 \rangle$ is expected to serve as a good proxy for the virial halo mass for our sample of simulated galaxies as majority of them have almost isothermal gravitational potential which is well approximated by $\Phi(r) \approx 3 \langle \sigma_p^2 \rangle \ln r + const$ at any radius according to the virial theorem. Curiously, the relation between supermassive black hole mass M_{BH} and host-galaxy bulge velocity dispersion $M_{BH} \propto \sigma^{4.24}$ (Gültekin et al., 2009) has approximately the same scatter ($\approx 31\%$) and the power as $M_{vir} - \sigma_p(R_2)$ and $M_{vir} - \langle \sigma_p^2 \rangle$ relations.

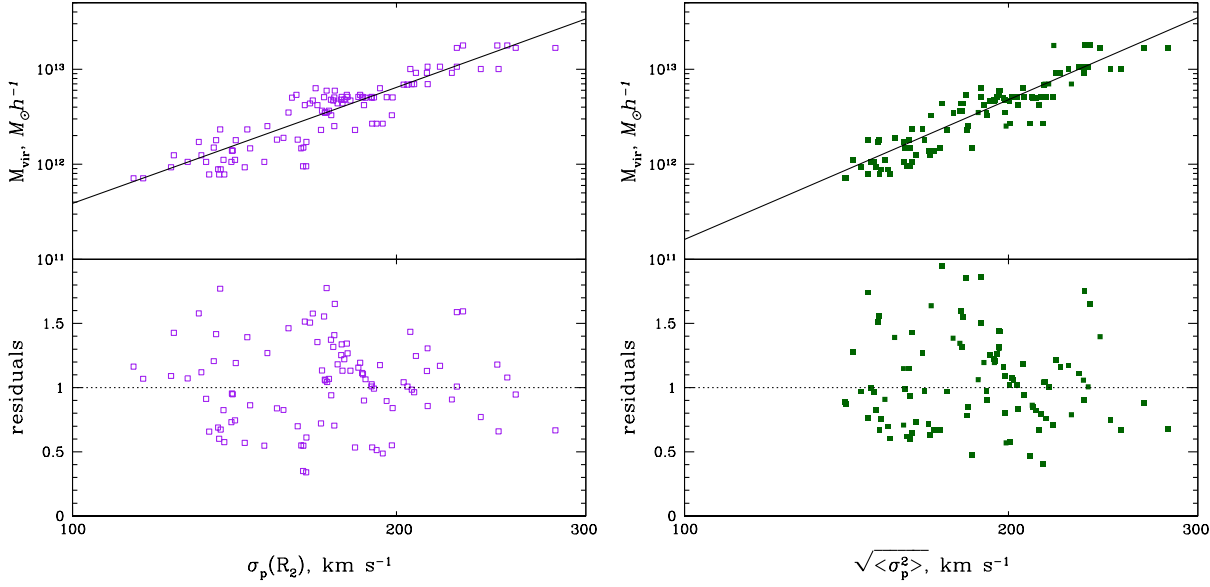


Figure 4.11: The virial mass of simulated galaxies as a function of the projected velocity dispersion at R_2 (left) and the luminosity-weighted average velocity dispersion (right).

We also test whether $\sigma_p(R_{1/2})$ and the luminosity-weighted projected velocity dispersion $\langle \sigma_p^2 \rangle_e$ measured within an aperture of radius $R_{1/2}$ correlate with the virial mass. We find that the rem-scatter for $\sigma_p(R_{1/2})$ is $\approx 60\%$ and for $\langle \sigma_p^2 \rangle_e$ the scatter is $\approx 50\%$, i.e. noticeably larger than for $\sigma_p(R_2)$ and $\langle \sigma_p^2 \rangle$.

4.6 Discussions and Conclusions.

We have compared the performance of two simple and fast methods that allow one to evaluate masses of elliptical galaxies at a special radius where the mass estimate is largely insensitive to the velocity dispersion anisotropy. Such methods could be useful for mass determination of large samples of galaxies with poor/noisy data when detailed investigation is not practical. A reliable mass estimate at a single radius could be also used as an additional constraint for the Schwarzschild dynamical modeling thus reducing the parameter space to be explored by dynamical models.

One approach uses local properties of the galaxy - logarithmic slopes of the surface brightness and velocity dispersion profiles and recovers the mass at a radius where the surface brightness declines as R^{-2} . Another approach uses the total luminosity-weighted velocity dispersion $\langle \sigma_p^2 \rangle$ and evaluates the mass at a radius where 3D stellar density $j(r) \propto r^{-3}$ which is claimed to be related to deprojected and projected half-light radii as $r_3 \approx r_{1/2} \approx R_{1/2}$. We test the accuracy and robustness of these simple mass estimators on analytic models, on a sample of cosmological zoom-simulations of individual elliptical galaxies and on real elliptical galaxies that have already been analyzed by means of a

state-of-the-art Schwarzschild approach.

We have found that

(i) for analytic models both methods recover a circular speed that is in good agreement with the true one. Churazov et al. estimator is found to be less sensitive to the assumptions under which it has been derived than the Wolf et al. one.

(ii) For massive slowly rotating simulated galaxies Churazov et al. formulae recover an (almost) unbiased estimate of the circular speed with RMS-scatter $\approx 5 - 6\%$. Wolf et al. relation also gives an almost unbiased measurement of V_c at the radius where the 3D stellar density declines as r^{-3} with RMS $\approx 7\%$. At the effective radius R_{eff} defined from the Sérsic fit to the surface brightness profile the average circular speed estimate is biased high by 3.4% and RMS-scatter is around 8%. For real elliptical galaxies R_{eff} is subject to additional uncertainty as its determination depends on the radial range used for the analysis and applied methodology.

(iii) For a sample of eight real elliptical galaxies analyzed with the Schwarzschild approach both methods show a remarkable agreement with the best-fit circular speed coming from the dynamical modeling. When averaged over the sample of eight galaxies our simple estimator overestimates the best-fit dynamical circular speed by 5%. This bias is mostly driven by a single galaxy (IC 3947) with the smallest R_{eff} in the sample. When this galaxy is excluded from the sample, the $V_c(R_{\text{sweet}})$ -estimator gives the circular speed estimate overestimated on average by 3.2% relative to the V_c^{Schw} with rms-scatter $\approx 3.1\%$. RMS-scatter between our simple estimates for different galaxies is $\approx 6.6\%$ which is comparable to measurement uncertainties. Wolf et al. estimator for the same sample gives mean deviation $\approx 2\%$ with slightly larger rms-scatter of $\approx 7.4\%$.

Table 4.4 provides the average deviation and the rms-scatter for different simple estimators resulting from the tests on simulated and real elliptical galaxies.

The projected velocity dispersion value at the radius R_2 where the surface brightness declines as R^{-2} seems to be a good proxy for the virial galaxy mass. M_{vir} (in $M_{\odot}h^{-1}$) can be approximated by $M_{\text{vir}} \approx 6 \cdot 10^{12} \left(\frac{\sigma_p(R_2)}{200 \text{ km s}^{-1}} \right)^4$ with RMS-scatter $\approx 40\%$. The scatter is comparable to the scatter observed when $\sqrt{\langle \sigma_p^2 \rangle}$ is used as a proxy for the virial halo mass.

4.7 Acknowledgments

NL is grateful to the International Max Planck Research School on Astrophysics (IMPRS) for financial support and Jeremy Murphy for providing kinematical data on M87.

Bibliography

- 2008, Binney J., Tremaine S., Galactic Dynamics, 2nd edn. (Princeton University Press)
- Breddels M.A., Helmi A., van den Bosch R.C.E., van de Ven G., Battaglia G. 2013, MNRAS, 433, 3173
- Cappellari M., Emsellem E., Krajnović D., McDermid R.M., Scott N., Verdoes K.G.A., Young L.M., Alatalo K., Bacon R., Blitz L., Bois M., Bournaud F., Bureau M., Davies R.L., Davis T.A., de Zeeuw P.T., Duc P.-A., Khochfar S., Kuntschner H., Lablanche P.-Y., Morganti R., Naab T., Oosterloo T., Sarzi M., Serra P., Weijmans A.-M. 2011, MNRAS, 413, 813
- Cappellari M. et al. 2013, MNRAS, 432, 1709 (Paper XV)
- Chen C., Côté P., West A.A., Peng E.W., Ferrarese L. 2010, ApJS, 191, 1
- Churazov E., Tremaine S., Forman W., Gerhard O., Das P., Vikhlinin A., Jones C., Böhringer H., Gebhardt K. 2010, MNRAS, 404, 1165
- Gerhard O.E. 1993, MNRAS, 265, 213
- Gerhard O.E., Binney J. 1996, MNRAS, 279, 993
- Gültekin K., Richstone D.O., Gebhardt K., Lauer T. R., Tremaine S., Aller M. C., Bender R., Dressler A., Faber S. M., Filippenko A.V., Green R., Ho L.C., Kormendy J., Magorrian J., Pinkney J., Siopis C. 2009, ApJ, 698, 198
- Jardel J.R., Gebhardt K. 2012, ApJ, 746, 89
- Jardel J.R., Gebhardt K., Fabricius M.H., Drory N., Williams M.J. ApJ, 763, 91
- Kormendy J., Fisher D. B., Cornell M. E., Bender R. 2009, ApJS, 182, 216
- Kowalczyk K., Lokas E.L., Kazantzidis S., Mayer L. 2013, MNRAS, 431, 2796
- Lyskova N., Churazov E., Zhuravleva I., Naab T., Oser L., Gerhard O., Wu X. 2012, MNRAS 423, 1813

- Lyskova N., Churazov E., Moiseev A., Sil'chenko O., Zhuravleva I. 2013, MNRAS, submitted
- Mamon G.A. and Boué G. 2010, MNRAS, 401, 2433
- Murphy J. D., Gebhardt K., Adams J. J. 2011, ApJ, 729, 129
- Naab T., Oser L., Emsellem E., Cappellari M., Krajnović D., McDermid R.M., Alatalo K., Bayet E., Blitz L., Bois M., Bournaud F., Bureau M., Crocker A., Davies R.L., Davis T.A., de Zeeuw P.T., Duc P.-A., Hirschmann M., Johansson P.H., Khochfar S., Kuntschner H., Morganti R., Oosterloo T., Sarzi M., Scott N., Serra P., van de Ven G., Weijmans A., Young L.M. 2013, MNRAS, accepted
- Oser L., Ostriker J.P., Naab T., Johansson P.H., Burkert A. 2010, ApJ, 725, 2312
- Richstone D. O., Tremaine S. 1984, ApJ 286, 27
- Rybicki G. B. 1987, in de Zeeuw P.T., ed., Proc. IAU Symp. 127, Structure and Dynamics of Elliptical Galaxies. Reidel, Dordrecht, p.397.
- Thomas J., Saglia R. P., Bender R., Thomas D., Gebhardt K., Magorrian J., Corsini E. M., Wegner G. 2005, MNRAS, 360, 1355
- Thomas J., Jesseit R., Naab T., Saglia R.P., Burkert A., Bender R. 2007, MNRAS, 381, 1672
- van den Bosch R. C. E., van de Ven G. 2009, MNRAS, 398, 1117
- Wolf J., Martinez G.D., Bullock J.S., Kaplinghat M., Geha M., Muñoz R.R., Simon J.D., Avedo F.F. 2010, MNRAS, 406, 1220

Chapter 5

Conclusions

The work presented in this thesis aims to investigate and further develop simple mass estimators for early-type galaxies which could be used for the analysis of large optical galaxy surveys. Measuring the mass profile of ellipticals is problematic due to the lack of mass tracers on known orbits. Dynamical orbit superposition modeling is considered to be the state-of-the-art technique for recovering the mass profiles of early-type galaxies and the investigation of their properties. However, this approach requires high quality observational data on the line-of-sight velocity moments and has a high computational cost, therefore, not practical for the mass determination of large samples of galaxies, especially in the case of poor and/or noisy observational data. For such a task it is desirable to have simple and robust methods based on the most basic observables which provides an unbiased mass estimate with a modest scatter.

The most basic optical observables are surface brightness and projected velocity dispersion profiles. Due to the degeneracy between the mass and the anisotropy of stellar orbits, these observables are not sufficient to unambiguously recover the distribution of mass with radius. However, at a special (characteristic) radius and under reasonable assumptions the mass-anisotropy degeneracy can be circumvented without invoking any additional data and detailed modeling. The existence of the characteristic radius where the mass is minimally affected by the unknown anisotropy was emphasized by Richstone and Tremaine (1984). Two approaches which evaluate mass at this special radius and are claimed to be weakly dependent on the anisotropy parameter, have been suggested recently (Churazov et al. 2010 and Wolf et al. 2010). While these approaches do not recover the radial mass distribution, reliable mass estimates at a single radius could nevertheless be useful (i) for cross-calibration of other mass determination methods; (ii) for inferring a non-thermal contribution to the total gas pressure when compared with the X-ray mass estimate at the same radius; (iii) for determining a dark matter fraction when compared with the luminous mass estimate; (iv) for deriving the slope of the mass profile when combined with the mass estimate from strong lensing; (v) and as a virial mass proxy.

The Churazov et al. ('local') technique uses local properties: logarithmic slopes of the surface brightness and velocity dispersion profiles. It estimates the mass at a radius R_2 where the surface brightness declines as R^{-2} (see also Richstone and Tremaine 1984,

Gerhard 1993). The radius R_2 typically lies not far from the half-light radius. In contrast, the Wolf et al. 2010 ('global') method uses the total luminosity-weighted velocity dispersion and evaluates the mass at a deprojected half-light radius, i.e. relies on the global properties of a galaxy.

To test the robustness and accuracy of these methods I applied them to analytical models, to simulated galaxies and to real early-type galaxies that had been already investigated in detail by state-of-the-art dynamical modeling.

I explore ~ 30000 analytical models, described by the Sérsic surface brightness distribution with Sérsic index $2 < n < 20$, anisotropy profile $\beta(r)$ mildly varying with radius and circular speed profiles typical for dwarf spheroidal galaxies and for elliptical galaxies. Both simple estimators are found to recover the circular speed (or mass $M(< r) = V_c^2 r / G$) that is in good agreement with the true circular velocity. The local approach seems to be less sensitive to the assumptions under which it has been derived than the global one. Tests show that the local method tends to overestimate mass of systems with the growing V_c -profile (in the vicinity of R_2) which are typical for dark-matter-dominated dwarf spheroidals. For these systems the global approach gives on average a less biased V_c -estimate. For surface brightness profiles with large Sérsic index ($n > 8 - 10$), typical for massive elliptical galaxies sitting at the centers of groups or clusters, the simple local estimator allows one to recover the circular speed over a wide range of radii where the log-slope of the surface brightness α is close to 2.

To relax the assumption of spherical symmetry, I test the methods on a large sample of cosmological zoom-simulations of individual galaxies which are similar in properties to nearby early-type galaxies. For slowly rotating simulated galaxies both the local and the global formulae recover an (almost) unbiased estimate of the circular speed when averaged over a sample. The local approach is characterized by $\text{RMS} \approx 5 - 6\%$, while the global estimator has $\text{RMS} \approx 7 - 10\%$. Moreover, for real elliptical galaxies the half-light radius is subject to additional uncertainty as its determination depends on the details of the analysis.

Tests on simulated galaxies also suggest that the projected velocity dispersion at the radius R_2 seems to be a good proxy for the virial galaxy mass. M_{vir} (in $M_\odot h^{-1}$) can be approximated by $M_{vir} [M_\odot h^{-1}] \approx 6 \cdot 10^{12} \left(\frac{\sigma_p(R_2)}{200 \text{ km s}^{-1}} \right)^4$ with the RMS-scatter $\approx 40\%$.

The scatter is comparable to the scatter observed when $\sqrt{\langle \sigma_p^2 \rangle}$ is used as a proxy for the virial halo mass.

Then I compare the simple estimators with the circular speed profiles derived from state-of-the-art dynamical modeling on a sample of real early-type galaxies. For this set of galaxies the simple V_c -estimates are in remarkable agreement with the results of the Schwarzschild modeling despite the fact that some of the considered galaxies are flattened and mildly rotating. When averaged over the sample the simple local estimator overestimates the 'Schwarzschild' V_c by $\approx 5\%$ with the RMS-scatter $\approx 6 - 7\%$ between different galaxies. The bias is comparable to observational uncertainties. Moreover, it is mostly driven by a single galaxy which is found to be the most compact one in the sample. When

this galaxy is excluded from the sample, the bias reduces to $\approx 3\%$ and the RMS-scatter to $\approx 3\%$. The global estimator for the same sample gives the mean deviation $\approx 2\%$ with the slightly larger RMS-scatter of $\approx 7 - 8\%$.

Given the encouraging results (a small bias and a modest RMS-scatter) of the tests I apply the local estimator to a sample of X-ray bright elliptical galaxies observed with the 6-m telescope of the Special Astrophysical Observatory of the Russian Academy of Sciences. I compare the simple optical V_c -estimates with X-ray V_c -profiles derived from the X-ray analysis of Chandra data under the assumptions of spherical symmetry and hydrostatic equilibrium of hot gas. The averaged over the sample ratio of the optical V_c -estimate to the X-ray one is equal to ≈ 0.98 with 11% scatter, i.e. there is no evidence for the large non-thermal pressure contribution in the gas at the radius which is not far from the half-light radius. Once the X-ray derived V_c^X is corrected for the non-thermal contribution, the mismatch between the V_c^X and the optical circular speed for isotropic distribution of stellar orbits V_c^{iso} provides a clue to the orbital configuration of the galaxy. E.g., at small radii $V_c^X > V_c^{iso}$ would suggest more circular stellar orbits, while at larger radii this would correspond to more radial orbits. For two galaxies (out of five) in our sample there is a clear indication that at radii larger than the half-light radius stellar orbits become predominantly radial. Finally, the difference between the optical V_c -estimate at the characteristic radius and the stellar contribution to the total gravitating mass allows one to calculate a dark-matter fraction f_{DM} . A typical f_{DM} for our sample of elliptical galaxies is $\approx 50\%$ for Salpeter IMF and $\approx 70\%$ for Kroupa IMF at the radius which is close the half-light radius.

The simple estimators can also handle globular clusters and/or planetary nebulae profiles to recover reliably the mass. Globular clusters and planetary nebulae play a crucial role in investigation of outer regions of elliptical galaxies. The method is not restricted to elliptical galaxies. It can also be applied to galaxy clusters where individual galaxies are user as tracer particles.

Acknowledgements

I would like to thank everyone who has helped me along my academic life during and before my PhD years. Most notably, I would like to acknowledge Rashid Sunyaev that I could be a member of the high energy group at MPA and for his generous support.

I would like to express my gratitude to my PhD supervisor Eugene Churazov for his direct involvement in my growth during my 3.5 years as a graduate student here at MPA.

I thank my collaborators - Ortwin Gerhard, Thorsten Naab and Klaus Dolag - for their suggestions and numerous discussions. It is a real pleasure for me to work with them.

I thank my family for believing in me and taking my dreams seriously.

Attended Conferences, Workshops and Schools

Conference ‘High Energy Astrophysics Today and Tomorrow’ Contributed talk	Moscow, Russia 2013
Conference ‘Physical link between galaxies and their halos’ Poster presentation	Garching, Germany 2013
Conference ‘The mass profile of galaxy clusters from the core to the outskirts: the need for a multi-wavelength approach’ Contributed talk	Madonna di Campiglio, Italy 2013
Conference ‘High Energy Astrophysics Today and Tomorrow’ Contributed talk and poster presentation	Moscow, Russia 2012
Conference ‘X-ray Sky: from Stars and Black Holes to Cosmology’, Contributed talk	Kazan, Russia 2012
XMM-Newton workshop ‘Galaxy clusters as Giant Cosmic Laboratories’ Contributed talk	Madrid, Spain 2012
Conference ‘High Energy Astrophysics Today and Tomorrow’ Poster presentation	Moscow, Russia 2011
Dublin Summer School on High Energy Astrophysics Poster presentation	Dublin, Ireland 2011
ESO workshop ‘Fornax, Virgo, Coma et al. Stellar systems in high density environments’ Poster presentation	Garching, Germany 2011
Conference ‘High Energy Astrophysics Today and Tomorrow’ Poster presentation	Moscow, Russia 2010
The NMDB Training Course ‘Cosmic rays and neutron monitors: A training course in science and applications’	Athens, Greece 2009
The 2009 International undergraduate summer school (IUSS09)	Sheffield, UK 2009

List of publications

Performance of simple mass estimators for elliptical galaxies

N. Lyskova, E. Churazov, S. Tremaine, J. Thomas, T. Naab
in preparation.

Stellar kinematics of X-ray bright massive elliptical galaxies

N. Lyskova, E. Churazov, A. Moiseev, O. Sil'chenko, I. Zhuravleva
2013, MNRAS, submitted

*The mass and angular momentum distribution of simulated massive galaxies
to large radii*

X. Wu, O. Gerhard, T. Naab, L. Oser, I. Martinez-Valpuesta, M. Hilz, E. Churazov,
N. Lyskova
2013, MNRAS, accepted

A simple recipe for estimating masses of elliptical galaxies and clusters of galaxies

N. Lyskova
2013, AN, 334, 360

Testing a simple recipe for estimating galaxy masses from minimal observational data

N. Lyskova, E. Churazov, I. Zhuravleva, T. Naab, L. Oser, O. Gerhard, X. Wu
2012, MNRAS, 423, 1813

*Modeling the images of relativistic jets lensed by galaxies
with different mass surface density distributions*

T. Larchenkova, A. Lutovinov, **N. Lyskova**
2011, Astron. Lett. 37, 4

Observations of lensed relativistic jets as a tool for constraining lens galaxy parameters

T. Larchenkova, **N. Lyskova**, A. Lutovinov
2011, Astron. Lett. 37, 7